Globular cluster systems and their implications of galaxy formation

Cho, Jaeil

Globular Cluster Systems

and

their Implications of Galaxy Formation

by Jaeil Cho

A Thesis submitted to the University of Durham

in accordance with the regulations for

admittance to the Degree of Doctor of Philosophy.

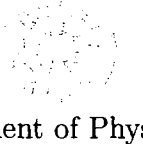

Department of Physics

University of Durham

December 2008

Dedicated to

my parents

and my wife Jiyoung

Globular Cluster Systems
and their Implications on Galaxy Formation

Jaeil Cho
Department of Physics
University of Durham

Abstract

In this thesis the spectroscopic and photometric results of the Galactic and extragalactic globular clusters are presented. And their implications on galaxy formation have been investigated.

Integrated spectroscopy with a high resolution of 24 Galactic globular clusters were obtained using the Isacc Newton Telescope, from which 21 line indices were carefully measured and calibrated. By comparing with recent simple stellar population models (Thomas et al. 2003 and Lee & Worthey 2005), it is confirmed that Galactic globular clusters are old ($\sim$10-12 Gyr). There is a discrepancy between the two models in low metallicity and the line indices measured have a better fit to Lee & Worthey (2005) model. These is a significant effect of blue horizontal branch stars on the Balmer absorption lines in integrated spectra, which could cause globular clusters to be underestimated their age.

Shell in elliptical galaxies are probably signature of recent galaxy merger/interaction. Properties of globular cluster systems (GCSs) in six shell galaxies have been examined and whether this signature can be seen in GCSs have been investigated. The GCSs in shell galaxies are found not to differ noticeably from those in normal elliptical galaxies in the sense that a mean colour get bluer with decreasing host galaxy luminosity and colour peaks of red and blue subpopulations are consistent with previous studies. This result is contradictory to results by Sikkema et al. (2006), who have found possible young globular clusters in the

two galaxies.

Using the Advanced Camera for Survey on the Hubble Space telescope, 10 low density early-type galaxies were observed and properties of their GCSs have been investigated to constrain galaxy formation history depending on environments. By comparing results from the Virgo Cluster Survey as a high-density counterpart, both similarities and differences between the two density groups were found. General behaviour of colour distributions of GCSs found in cluster environment are also seen in those in field galaxies; mean colour gets redder as increasing with galaxy luminosity, less bimodal colour distributions are detected in lower galaxy luminosity, and there is a correlation between red colour peak and host galaxy luminosity. However, mean colours of GCS in low-density appear to be slightly bluer than those in high-density at a given galaxy luminosity, which implies that GCS in field environments is either less metal-rich or younger than those in cluster environments. More diverse shape of colour distributions are found in dense region than in low-density region, which would reflects more complicated galaxy formation history in dense region. In spite of finding environmental this effect on galaxy formation, this effect is so subtle that galaxy (final) mass is still a dominant factor to determine galaxy formation and stellar populations in there.

Acknowledgments

First of all, I would like to thank to my supervisor, Ray Sharples. During the period of Ph. D. student he gave me a precious advice and encouragement. Academically, he taught me almost all areas of Astronomy, observation, data reduction, statistics, theory, and English. Socially, he helped me settle down in England and encourage me to enjoy the life in Durham. I especially thank for his patience. Despite of long delay of completing this thesis, he always gave me another chance and believed me. At the same time I apologize for some troubles I made.

I would also like to thank to staff/postdocs in the Department. John Lucy, Russell Smith, and Naoyuki Tamura gave me an advice on my projects. Thanks to Mark Norris for organizing discussion meeting, sharing some data and helping me English. Thanks to Alan Lotts for sorting out computational problems. Outside Durham, I thank to John Blakeslee, Arunav Kundu, Eric Peng, Sukjin Yoon, and Stephen Zepf for invaluable comments on my research and friendly providing me with their data/models. Also thanks to faculties in Yonsei for a general advice and always warm welcome: Yong-Ik Byun, Suk-Hwan Kim, Yong-Chul Kim, Sukyoung Lee, Young-Wook Lee and Young-Jong Sohn.

I also thank to the Korean Government, the Education Director in Korean Embassy, London and the Higher Education Funding Council for England that support me financially for 3 years.

I specially thank to those in Durham Korean Church for providing Korean food and

social life, even though I do not attend to the service: Jung-Kyu Sun, Han-Sik Kim, Jiho Lee, Ki-Young Park, Young-Jun Yoon and many others.

Finally, I would like to thank to my parents and my sister who always support me and believe in me. Specially thanks to my parents in law for belief and love. I would like to dedicate this thesis to my wife, Jiyoung Nam, who always supports and loves me.

Declaration

The work in this thesis is done by the author under the supervision of Prof. Ray Sharples in the Department of Physics, University of Durham. I confirm that no part of the material offered has previously been submitted by me for a degree in this or in any other University.

Table of Contents

List of Tables

List of Figures

A hypothesis or theory is clear, decisive, and positive, but it is believed by no one but the man who created it. Experimental findings, on the other hand, are messy, inexact things which are believed by everyone except the man who did that work.

Harlow Shapley

Chapter 1

Introduction

A globular cluster (GC) is group of stars which is gravitationally bound with increasing star density toward its center. GCs have little gas/dust, a nearly spherical shape and are generally found orbiting a parent galaxy. Figure 1.1 shows an image of M80, one of the GCs in the Milky Way, which is at a distance of approx 10 kpc from the Sun. Studies of GCs can provide us with great insights into understanding stellar evolution, galaxy formation, and even cosmological parameters such as the age of the Universe. The resolved stars in GCs are useful for testing stellar population theories, since for most GCs these stars appear to form simultaneously with the same chemical abundance. Moreover, GC systems in galaxies can play a key role in understanding the formation of their host galaxy, because they are thought to have formed along with the bulk of stars in galaxies so that they contain a fossil record of galaxy formation. Most GCs in the Milky Way are old (10-12 Gyr) and they are regarded as the oldest stellar structures in the Universe, which provides a lower limit of the age of the Universe (Chaboyer 1995).

GCs are found around parent galaxies with a wide range of galaxy luminosity, from dwarf to giant elliptical galaxies, and in all morphological types; there is even the possibility of the presence of intergalactic globular clusters (Jordán et al., 2003). Studying GC systems in external galaxies has many advantages. The unresolved diffuse stellar light in galaxies

Figure 1.1: Image of M80 globular cluster taken by the Hubble Space Telescope (Ferraro et al. 1999).

can be a mixture of more than one stellar population with various chemical abundances and ages. It is very difficult to derive a unique combination of intrinsic stellar populations from these systems. However, the GCs associated with a parent galaxy can be easily compared with theoretical Simple Stellar Population models which are characterized by a single age and metallicity. The distribution of ages and metallicities for the whole Globular Cluster System (GCS) can then be used to provide constrains on the stellar components of the parent galaxy. In addition, GCSs are spatially more extended than stars in their host galaxies, so the dynamics of GCSs can also constrain dark halo mass host galaxies belong to (e.g. Peebles 1984; Côté et al. 2003)

1.1 Globular Clusters in The Milky Way

1.1.1 Observational history

Abraham Ihle is believed to have discovered the first globular cluster, M22, in 1665; until then globular clusters were indistinguishable from stars. GCs were thought to be one of the many gaseous nebulae in the sky until Messier resolved individual stars in M4 and listed 28 other unresolved GCs in Messier's Catalogue (Messier 1781). Later Herschel resolved stars in 70 GCs including 33 new GCs found by himself; he is also the first person who used the term "*Globular Cluster*" (Herschel 1789).

Intense studies of GCs were undertaken by Shapley in the early 20th century (Shapley 1918a, Shapley 1918b, Shapley 1918c, Shapley & Shapley 1919). His most remarkable discovery began with the construction of the three dimensional spatial distribution of GCs, by deriving distances from the period-absolute magnitude relation for Cepheid variable stars (they were confirmed to be RR Lyrae variables later). This spatial distribution showed that GCs are not symmetrically distributed around the Sun and broke the conventional concept that the Sun is at the center of the Milky Way.

An up to date census of GCs contains 150 GCs in the Milky Way (Harris 1996, current version was revised in 2003), but still new GCs are being discovered in the Galactic disk where strong dust has previously obscured possible GC candidates. For example, large infrared surveys such as the Two Micron All Sky Survey (Skrutskie et al. 1997, 2MASS) and the Spitzer Galactic Legacy Infrared Mid-Plane Survey Extraordinaire(Benjamin et al. 2003, GLIMPSE) have contributes the discovery of several new GCs in the Galactic disk with the advantage of being much less susceptible to extinction by dust at infrared as opposed to optical wavelength (e.g. Hurt et al. 2000; Bica et al. 2003; Borissova et al. 2003; Dutra et al. 2003; Kobulnicky et al. 2005). Harris (2001) estimates that the total number of GCs in the Milky Way is around $N = 160 \pm 10$, by analyzing the number density of GCs vs Galactic latitude.

1.1.2 Colour-Magnitude diagrams of GCs

A colour-magnitude diagram (CMD) is a powerful and one of the most common methods for plotting the photometric data of GCs. Physically colour on the x-axis and magnitude on the y-axis reflects the star's temperature and luminosity respectively. Each location on the CMD is a function of the mass, age, and metallicity of a star. Because all the stars in one GC share the same age and metallicity, points on a CMD indicate different stellar evolution stages depending on the mass of the star. Figure 1.2 shows the CMD of M15 with major evolutionary stages labelled. In brief, at the main sequence stage, stars are burning hydrogen into helium in their core and spend most of their lifetime in this stage. After consumption of most of the hydrogen in the core, stars turn into red giant branch stars with a hydrogen burning shell. Horizontal branch stars have a helium burning core, and then they evolve to asymptotic giant branch star with a helium burning shell (see review by Carney (2001) for more detail).

Using a CMD of a GC, many techniques to derive physical parameters such as age and

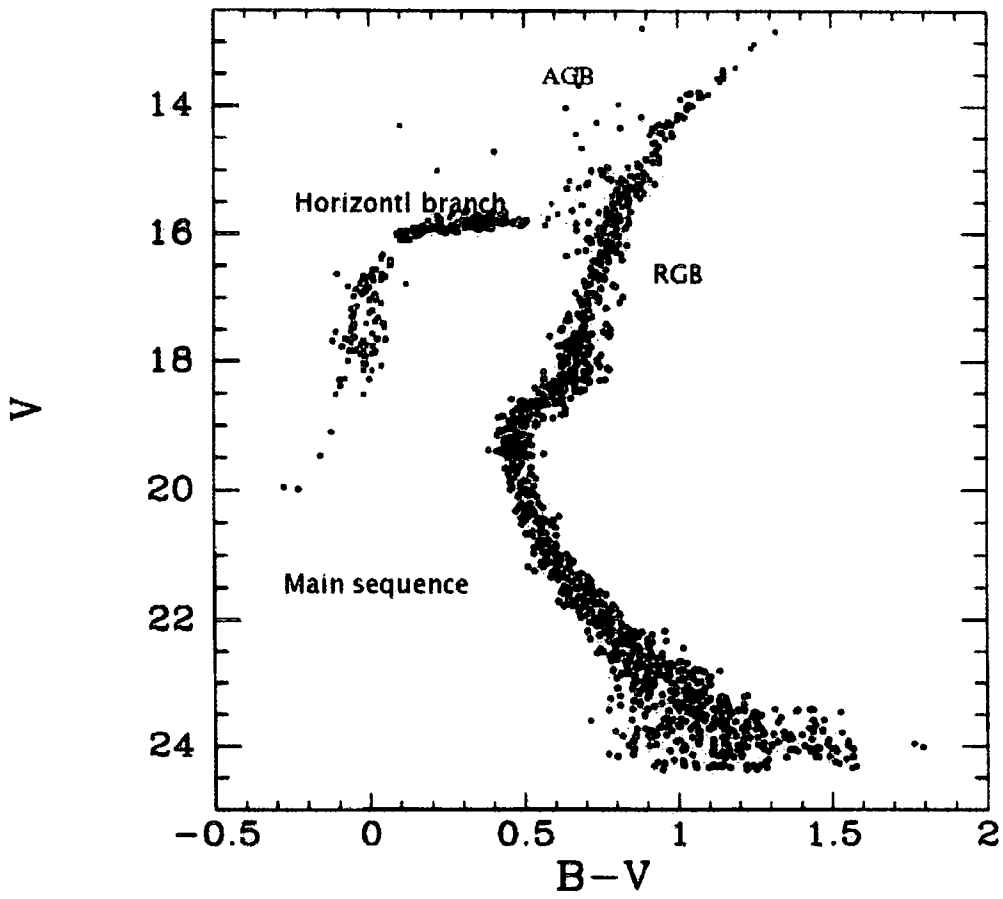

Figure 1.2: Colour-Magnitude diagram of M15 taken from Durrell & Harris (1993). Major evolutionary stages are labelled: main sequence, red giant branch star(RGB), horizontal branch stars, and asymptotic giant branch stars (AGB).

metallicity have been developed. The most widely used method to estimate the age of a GC is to measure the magnitude difference between the main sequence turn-off and the horizontal branch (Iben & Faulkner 1968; Sandage 1982). This method is based on the fact that the luminosity at the main sequence turn-off point is decreasing with increasing age, while that of the horizontal branch remains roughly constant. Another method proposed by Vandenberg et al. (1990) is to measuring the colour difference between the main sequence turn-off and the base of the red giant branch. The colour of the former get much bluer with increasing age so that a smaller colour difference implies an older cluster age. These two methods are still used to day (e.g. Rosenberg et al. (1999); Salaris & Weiss 2002; De Angeli et al. 2005) Finally, direct fitting of theoretical isochrones to observational data on the CMD is also commonly used, from which metallicity also can be derived. The latest example for this method is the survey of GCs using the Advanced Camera for Survey (ACS) on the Hubble Space telescope (HST) (Sarajedini et al. 2007) that is currently obtaining the CMDs of 65 GCs and comparing them with theoretical isochrones from Dotter et al. (2007). Measuring metallicity from photometric data is rather more challenging than from spectroscopic data. One technique is to use the red giant branch, which moves towards redder colours with increasing metallicity (e.g. Ortolani et al. 1990; Saviane et al. 2000).

1.1.3 Galactic globular clusters and formation of the Galactic halo

There are two classic theories for the formation of the Milky Way. In the Eggen et al. (1962) model (ELS model), the Galaxy formed from a monolithic collapse of one protogalactic gas cloud. This model was challenged by Searle & Zinn (1978) (SZ model) who suggested that the Galactic halo must be assembled from many sub fragments since there is no metallicity gradient against the distance from the Galactic center in the halo. Zinn (1993) (see also Lee et al. 1994) divided the Galactic globular clusters into three subgroups based on their metallicity and horizontal branch morphology. In Figure 1.3, metallicity is plotted against distance from

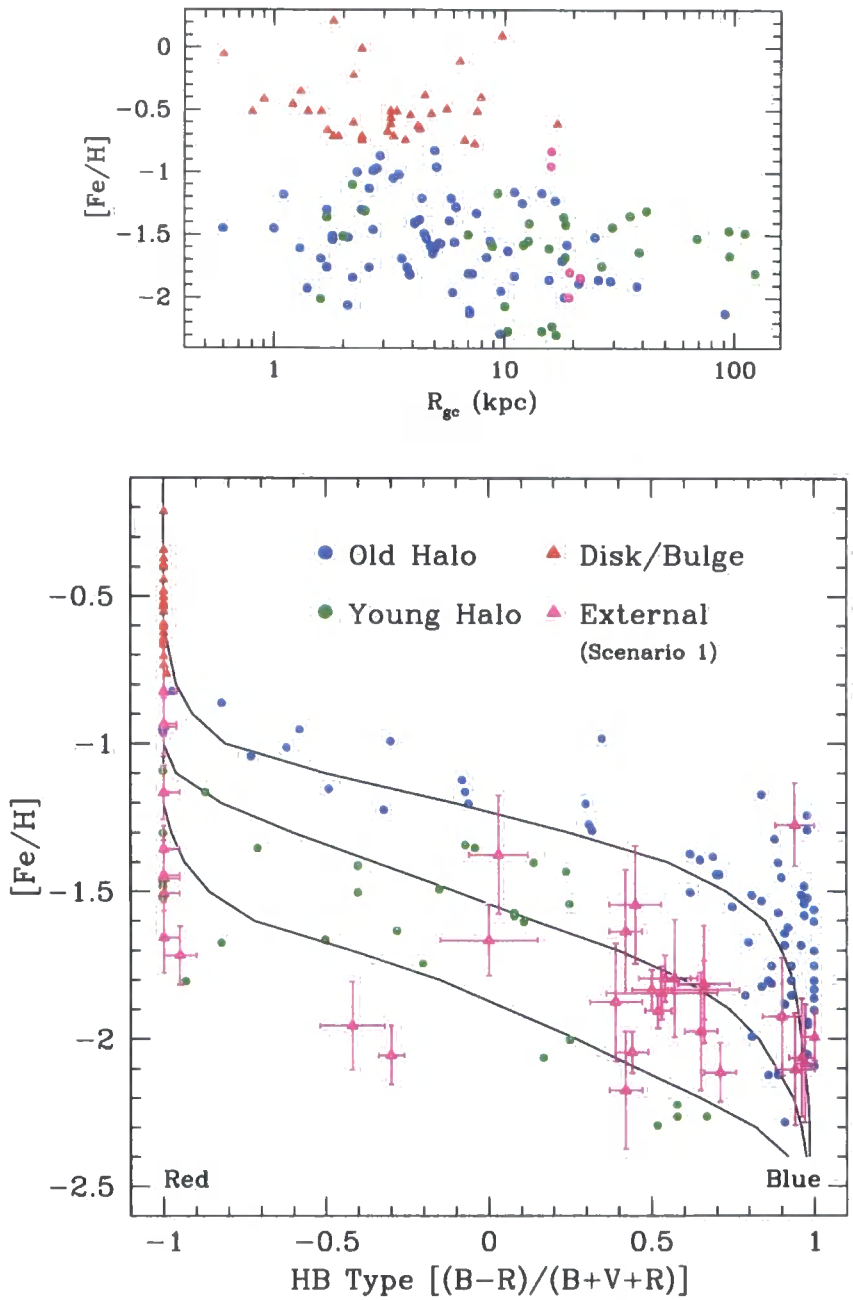

Figure 1.3: Metallicity vs distance to the Galactic center and HB type for globular clusters. These plots are taken from Mackey & Gilmore (2004). The isochrones in the bottom plot originated from Rey et al. (2001). Between each track there is an age gap of 1.1 Gyr with the top track being the oldest. External GCs (pink triangles) belong to the LMC, SMC, Sagittarius, and Fornax dwarf spheroidal galaxies.

the Galactic center and horizontal branch (HB) morphology index (HBR[1]) for the three subsystems. Most metal-rich GCs ([Fe/H]>-0.8) lie within ~8 kpc from the Galactic center and are associated with the Galactic disk/bulge (disk/bulge GCs, *red triangles*). However, metal-poor GCs ([Fe/H]<-0.8) have a large spread in HB morphology. Zinn (1993) found that most metal-poor GCs within 6 kpc have bluer HB morphology than those outside 6 kpc at a given metallicity and a tighter trend on the metallicity-HB type plane. This dispersion of HB type at a given metallicity is the well known *second-parameter effect.* By assuming that the second parameter is age, Zinn (1993) divided the metal-poor GCs into young halo (*green circles*) and old halo (*blue circles*) GCs and argued that while the disk/bulge and old halo GCs from by a dissipate collapse of protogalactic cloud and the young halo GCs would be accreted from dwarf galaxies.

This argument is supported by the fact that some young halo GCs (Arp 2, Ter 8, Ter 7, Pal 12, and NGC4147) are now thought to belong to the Sagittarius dwarf (Da Costa & Armandroff 1995 and Bellazzini et al. 2003), the nearest galaxy with a highly elongated shape due to tidal disruption. Many GCs in dwarf satellites such as the Large Magellanic Cloud (LMC), Small Magellanic Cloud (SMC), and Fornax fall in the area where young halo GCs are found on the metallicity-HB type plane (*pink triangles* in the bottom plot in Figure 1.3). Another signature of accretion is that some massive GCs (ω cen, NGC6715, and M54) show multiple stellar populations so that they may be remnants of stripped cores of dwarfs that have been captured by the Galaxy (Lee et al. 1999; Layden & Sarajedini 2000; Villanova et al. 2007). The general picture of the formation of the Milky Way at present is that the inner halo stars formed by a dissipative collapse resulting in the Galactic disk/bulge, and the outer halo stars were built up by the accretion of nearby dwarf galaxies.

[1]The HBR index is defined as $HBR \equiv (B-R)/(B+V+R)$ by Lee et al. (1994), where B and R are the number of stars bluer and redder than the instability strip respectively, and V is the number of RR Lyrae stars.

As described above, the Milky Way is an excellent example of how globular cluster systems can be exploited to derive galaxy formation history. This principle can be applied to external galaxies as well, which will be introduced in the following section. In fact, these Milky Way formation models give very useful insights to other early-type galaxy formation models.

1.2 Extragalactic Globular Cluster Systems

1.2.1 Globular cluster system of M31

M31 (the Andromeda galaxy) is the nearest spiral galaxy with a similar mass and morphology of the Milky Way, so that its globular cluster system (GCS) is a good comparison with that of the Milky Way. In terms of richness of GCs, M31 possesses almost three times more GCs than the Milky Way and even more unconfirmed GC candidates. For example, the recent catalogue of GCs in M31 by Barmby et al. (2000) lists about 430 GCs and one by Galleti et al. (2004) contains 338 confirmed GCs and 688 candidates. The luminosity function of the GCS in M31 shows a similar Gaussian shape to that of the Milky Way with Gaussian fitting parameters of $M_V = -7.5$ and $\sigma = 1.1$. Its metallicity distribution is also bimodal with similar peak positions (Perrett et al. 2002). Figure 1.4 shows a comparison of the metallicity distribution for the GCSs in M31 and the Milky Way. There is also a slight metallicity gradient against distance from the center of M31. The majority of GCs are old in both systems.

Overall the picture of M31 formation is expected to be similar to the Milky Way with dissipational collapse producing disk/bulge GCs, and halo GCs which have been accreted externally. However, the most distinct feature of the GCS in M31 is the presence of significant number of intermediate age GCs (5-8 Gyr) and even extremely young GCs [2] (<1 Gyr), which

[2]Cohen et al. (2005) argue that such a young GC is actually an asterism, faint star associations with

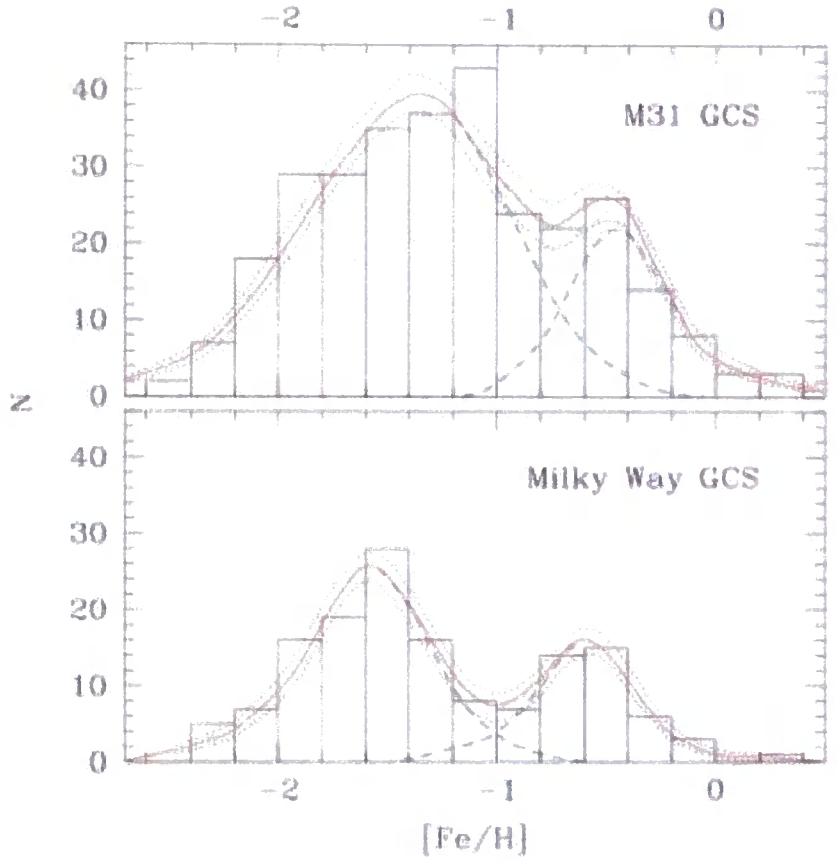

Figure 1.4: Metallicity distributions of GCSs in M31 and the Milky Way. This plot is taken from Perrett et al. (2002). The metallicity peak positions are [Fe/H]≈ -1.4 and [Fe/H]≈ -0.5 for metal-poor and metal-rich populations in M31 respectively. For the Milky Way, the colours are [Fe/H]≈-1.6 and [Fe/H]≈-0.6 for blue and red populations respectively.

are not found in the Milky Way System (e.g. Perrett et al. 2002; Beasley et al. 2004; Burstein et al. 2004; Puzia et al. 2005). This implies that mergers/accretions occurred much more recently than the Milky Way. Direct evidence of accretion of dwarfs in the from of streams and substructures are also found in M31 (e.g. Ibata et al. 2001; Ferguson et al. 2002).

Another distinct feature of M31 GCs found by Burstein et al. (1984) is enhancement in the CN index with respect to the Milky Way GCs. Note that CN is mainly governed by nitrogen abundance, since carbon is rapidly turned into CO molecular. This nitrogen enhancement in M31 GCs is now well-established by many other studies (e.g. Tripicco 1989; Brodie & Huchra 1991; Ponder et al. 1998; Li & Burstein 2003; Beasley et al. 2004). Burstein et al. (1984) also found that the $H\beta$ line in M31 GCs is systematically stronger than in Milky Way GCs at a given Mg_2 line. However, this trend still remains somewhat controversial as the recent study by Beasley et al. (2004) concludes that there is no enhancement in the Balmer lines in M31 GCs compared to the Milky Way GCs in general. The mechanism for the enhancement of nitrogen in M31 GCs is not well understood yet. One possible explanation would be that the difference is primordial and that the protoglobular clouds in M31 were enriched in nitrogen at an early epoch (Brodie & Huchra 1991, Beasley et al. 2004).

1.2.2 Properties of extragalactic globular cluster systems (GCSs)

Beyond the local group, most studies of extragalactic GCSs have been focused on early-type galaxies because observationally they host a large of number of GCs (hundreds), giving a statistical advantage, and they are relatively easy to detect compared to late-type galaxies where strong dust is also present and the galaxy light is severely attenuated. Theoretically the formation of massive elliptical galaxies is also of great interest.

One of the most interesting findings in GCSs in elliptical galaxies is the bimodal distri-

superimposed bright stars, not a globular cluster, although most GCs with an age of ~5 Gyr appear to be genuine.

bution in colour, which was first detected by Zepf & Ashman (1993). Since then, colour bimodality has been found to be common in massive elliptical galaxies (e.g. Ajhar et al. 1994; Zepf et al. 1995; Secker et al. 1995; Geisler et al. 1996). Thanks to the Hubble Space Telescope (HST), several intense studies on GCSs covering a wide range of galaxy luminosity have been conducted (e.g. Gebhardt & Kissler-Patig 1999; Larsen et al. 2001; Kundu & Whitmore 2001a, 2001b). To summarize their common findings, there is generally a colour gradient with distance from the galaxy center, the blue clusters are spatially more extended, and the mean colour of the GCS and colour peak of the red subpopulation are correlated with galaxy luminosity, However, a correlation of the blue peak colour was not confirmed (see discussion in §5.4). The advent of the Advanced Camera for Survey (ACS) on the HST makes it possible to study GCSs with improved accuracy of photometry. For example, Peng et al. (2006a) present 100 colour distributions of GCSs in the Virgo galaxy cluster, confirmed the previous findings and detecting a blue peak trend with luminosity. There are even trimodal colour (metallicity) distribution found in giant elliptical galaxies such as NGC5128 (Woodley et al. 2005 and NGC4365 (Brodie et al. 2005). It is still controversial whether additional subpopulation between normal metal-poor and metal-rich subpopulations are intermediate age or intermediate in metallicity (Brodie et al. 2005 and Beasley et al. 2008).

Globular cluster luminosity functions (GCLFs) are usually well represented by a Gaussian function with peak $M_V \sim -7.4$ and $\sigma \sim 1.4$; this peak position appear to be universal in massive galaxies so that it can also be used as a distance indicator (e.g. Harris 2001; Richtler 2003; Jordán et al. 2007b). Another important aspect of the GCLF is its dynamical evolution. Fall & Zhang (2001) showed that an initial power-law GCLF evolved to a log-normal GCLF as low-mass GCs are evaporated by two-body relaxation so that the turnover magnitude is expected to brighten with time and more so toward the galaxy center. This is supported by theoretical N-body simulations (Baumgardt & Makino 2003) and the observed luminosity function of young GCs (Whitmore & Schweizer 1995). Moreover, Goudfrooij et al. (2004)

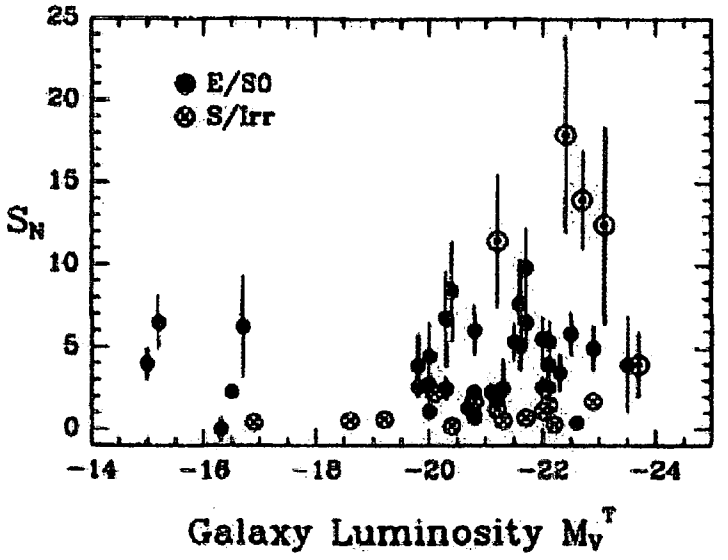

Figure 1.5: Specific frequency vs galaxy luminosity taken from Harris (1991)

found that GCLFs in outer parts of galaxies tend to have a power-law form, whereas the GCLF in the inner parts shows a normal turnover. The LF of inner blue GCs has a brighter turnover magnitude than that of the inner red GCs, which implies that red GC are younger and possibly formed from major mergers.

The richness of GCSs is often expressed by the total number of GCs scaled to the parent galaxy luminosity. Specific frequency introduced by Harris & van den Bergh (1981) is defined as

$$S_N = \frac{N_{GC}}{10^{-0.4(M_V+15)}}$$

, where N_{GC} is a total number of GCs and M_V is the absolute magnitude of the host galaxy. The classic plot of S_N vs galaxy luminosity (Figure 1.5) shows a increase of S_N for luminous galaxies and even towards the faint end. Such a U-shape in specific frequency is not yet well understood. However, the recent study by Peng et al. (2008) revealed a similar trend of specific frequency for galaxies in the Virgo cluster, but is slightly flatter for luminous

galaxies. These authors also found that GCSs with higher S_N in dwarf ellipticals are mainly located toward the central region of the Virgo cluster, which implies that environment plays some role in GC and galaxy formation processes.

1.3 Globular Cluster Systems and Galaxy Formation

As described above, colour bimodality is observed to be quite common in elliptical galaxies. To explain this, Ashman & Zepf (1992) introduced a merger model in which two equal mass gaseous spirals with metal-poor GCs (MPGCs) merge to produce metal-rich GCs (MRGCs) from the enriched gas. This model is supported by the presence of young GCs in present day merging/interacting galaxies like the Antennae Galaxy (Whitmore & Schweizer 1995) and NGC3921 (Schweizer et al. 2004). Alternatively, an *in situ* model proposed by Forbes et al. (1997) suggests that when giant molecular clouds collapse dissipationally, MPGCs are formed first. This is then somehow suddenly truncated at high redshift, after which the MRGCs form along with the bulk of the field stars. In the accretion model (Côté et al. 1998), MRGCs are formed by dissipational collapse and then MPGCs from nearby dwarfs are accreted.

There is also a new approach to explain the colour bimodality via a non-linear colour-metallicity relation (Yoon et al. 2006). Even a single peak of metallcity distribution can be projected to a bimodal colour distribution by this relation which may be the result of horizontal branch stars. We test and discuss this hypothesis further in §3.4.2. Simulations by Cantiello & Blakeslee (2007) have also produced similar results.

1.4 Structure of this Thesis

This thesis presents a new body of ground-based spectroscopy and Hubble Space Telescope photometry, with which to address some of the outstanding questions in the link between

globular clusters and galaxy formation.

- In Chapter 2, high S/N integrated spectroscopy of 24 Galactic globular clusters are presented. Line indices are measured and compared with two recent simple stellar population models to investigate the effect of horizontal branch stars on line indices.

- In Chapter 3, globular clusters in six shell elliptical galaxies are detected and their properties are presented. We investigate any signature of recent star formation in their globular cluster systems.

- In Chapter 4, properties of the globular clusters systems in 10 low luminosity early-type galaxies in low density environments are presented. By comparing with the Virgo Cluster Survey, we investigate environmental effects on galaxy formation.

- In Chapter 5, Further analysis is conducted for important issues in the previous Chapters. Results and their scientific implications are discussed.

Chapter 2

High Resolution Spectroscopy of Galactic Globular Clusters

2.1 Observations

Spectroscopic observations of 24 Galactic globular clusters (GGCs) were conducted with the 2.5m Isaac Newton Telescope in La Palma, Spain from 4-7th July, 2000. Our sample of GGCs span a wide range of metallicity,$-2.28 < [Fe/H] < -0.04$, with a mean metallicity of $[Fe/H] = -1.27$. It also includes clusters with various horizontal branch morphologies. The basic properties of these GGCs are listed in Table 2.1. The instrumentation used was the Intermediate Dispersion Spectrograph (IDS) with the 235 camera, the EEV10 CCD detector, the R900V grating, and a long-slit with width of 1.5″, which provides a spatial resolution of 0.4 ″/pix, a wavelength range of 4000-5400Å, and a spectral resolution of FWHM$\sim$2.0Å. The slit was drifted $\pm 1 r_c$ from the cluster center, where r_c is the cluster core radius, during the exposure time of 900 seconds. This technique avoids the possibility that a bright foreground star or one of the individual bright stars in a cluster accidently dominates the whole integrated spectrum. In order to estimate the systematic uncertainties in line

indices, and to check for foreground star contamination, we repeated each exposure with the slit in an orthogonal direction.

For bright (large) globular clusters, separate sky exposures $\sim 20'$ away from the center of the cluster were obtained for background subtraction. The observation date, the number of exposures in each direction, and the number of sky exposures are listed in Table 2.2. Figure 2.1 demonstrates the scan coverage for each GGC on Digitalized Sky Survey images. A total of 47 Lick standard stars were also observed for an accurate calibration to the Lick system (Burstein et al., 1984). A spectrophotometric standard star was observed each night for flux calibration. The exposure times for the standards vary from 4 seconds to 10 seconds depending on their brightness. Between each repositioning of the telescope, an arc frame was taken using a CuAr/CuHe lamp for wavelength calibration. Each exposure produced a raw image with 500 pixels along the spatial axis $\times$ 4200 pixels along the dispersion axis. The gain of the CCD was $1.17e^{-}/ADU$, and the readout noise $4.2e^{-}/pix$.

2.2 Data Reduction

2.2.1 Basic data reduction

The raw images were reduced using the standard IRAF package. The basic CCD reduction was performed by following the procedure in *A User's guide to CCD Reductions with IRAF* (Massey, 1997). The *IRAF/ccdred* package was first used to trim an overscan region and to subtract a bias frame. A flat-field frame and a twilight sky frame for each night were constructed by averaging several separate frames. Then, using the *twodspec.longslit* package, a normalized and smoothed flat-field and twilight sky flat were made along the dispersion and the spatial axes respectively. By multiplying the previous two products, the 'ideal' flat was produced, which was used for flat fielding of all of the science data as well as the calibration data.

Table 2.1: Properties of the Galactic Globular Clusters (GCSs)

NGC name	other	b	$R_{gc}[kpc]$	[Fe/H]	HBR
		(1)	(2)	(3)	(4)
NGC5904	M5	46.80	6.2	-1.27	0.31
NGC6093	M80	19.46	3.8	-1.75	0.93
NGC6171	M107	23.01	3.3	-1.04	-0.73
NGC6205	M13	40.91	8.7	-1.54	0.97
NGC6218	M12	26.31	4.5	-1.48	0.97
NGC6229		40.31	29.7	-1.43	0.24
NGC6304		5.38	2.2	-0.59	-1.00
NGC6341	M92	34.86	9.6	-2.28	0.91
NGC6342		9.73	1.7	-0.65	-1.00
NGC6356		10.22	7.6	-0.50	-1.00
NGC6517		6.76	4.3	-1.37	...
NGC6528		-4.17	0.6	-0.04	-1.00
NGC6626	M28	-5.58	2.7	-1.45	0.90
NGC6638		-7.15	2.3	-0.99	-0.30
NGC6717		-10.90	2.4	-1.29	0.98
NGC6760		-3.92	4.8	-0.52	-1.00
NGC6779	M56	8.34	9.7	-1.94	0.98
NGC6838	M71	-4.56	6.7	-0.73	-1.00
NGC6864	M75	-25.75	14.6	-1.16	-0.07
NGC6934		-18.89	12.8	-1.54	0.25
NGC6981	M72	-32.68	12.9	-1.40	0.14
NGC7006		-19.41	38.8	-1.63	-0.28
NGC7078	M15	-27.31	10.4	-2.26	0.67
NGC7089	M2	-35.78	10.4	-1.62	0.96

Col. (1): Galactic latitude; col. (2): Distance from Galactic center; col. (3): Metallicity; col. (4): Horizontal branch morphology. The HBR index is defined as $HBR \equiv (B-R)/(B+V+R)$ by Lee et al. (1994), where B and R are the number of stars bluer and redder than the instability strip respectively, and V is the number of RR Lyrae stars. All the data are from Harris (1996).

Table 2.2: Observation Log

Night	Object name	S-N	W-E	Sky
4 Jul 2000	NGC5904(M5)	2	2	2
	NGC6171(M107)	2	2	
	NGC6229	2	2	
	NGC6838(M71)	2	2	4
	NGC7089(M2)	2	2	
5 Jul 2000	NGC6205(M13)	2	2	1
	NGC6528	2	2	
	NGC6341 (M92)	2	2	
	NGC6934	2	2	
	NGC7006	2	2	
	NGC7078(M15)	2	2	
6 Jul 2000	NGC6517	2	2	
	NGC6356	2	2	
	NGC6638	2	2	
	NGC6717	2	2	
	NGC6864(M75)	2	2	
	NGC6981(M72)	2	2	
7 Jul 2000	NGC6093(M80)	2	1	
	NGC6304	2	2	
	NGC6218(M12)	2	2	
	NGC6342	0	3	
	NGC6626 (M28)	0	2	
	NGC6779(M56)	2	2	
	NGC6760	2	0	

The number of exposures obtained for each GGC are listed. S-N indicates a South to North direction of scan and W-E for West to East. Separate sky exposures were taken for three bright extended globular clusters to obtain a better sky subtraction. In other cases, sky spectra were taken from the ends of the long slit.

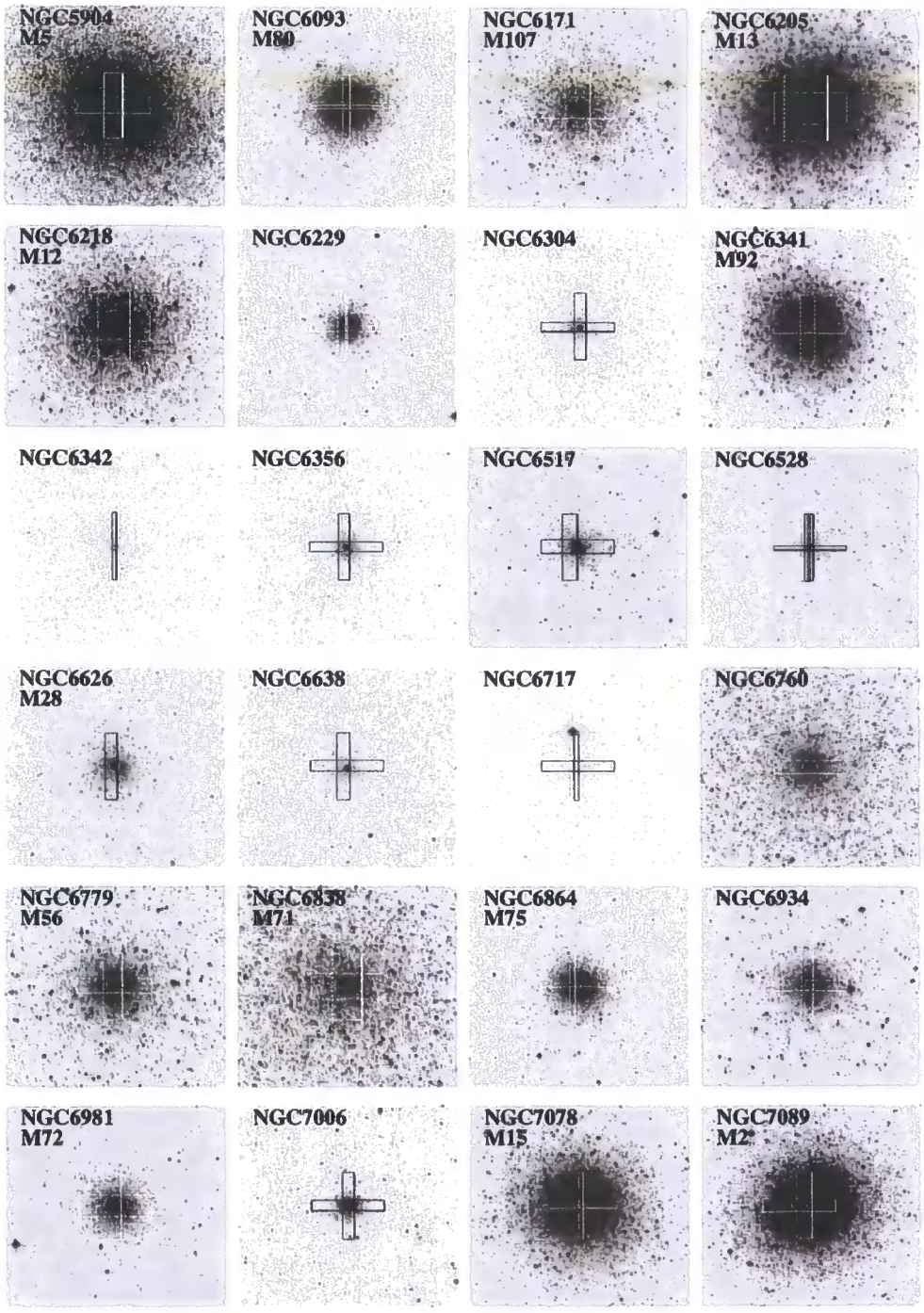

Figure 2.1: Digitalized Sky Survey images of the GGCs observed showing the slit coverage. The circle in the center of each globular cluster represents the core radius. In each rectangle, the long dimension is the slit size, and the short dimension is the drift coverage, which was determined so as to cover a core radius from the center. The slit position and covering area are drawn based on the telescope positions in image headers from our observations and have some pointing uncertainties.

There are several ways to remove cosmic rays in spectroscopic data. *LA-cosmic*, developed by van Dokkum (2001), is a software package that removes cosmic rays with a Laplacian edge-detection technique. Another way is to use the *APALL* routine in the IRAF package, which rejects any highly deviated values while optimally extracting a spectrum. Both methods were tested, and it was concluded that *APALL* alone can remove most of the cosmic rays successfully without needing an additional procedure.

After the basic CCD reduction, spectra were extracted and calibrated following the procedures in *A User's Guide to Reducing Slit Spectra with IRAF* (Massey, Valdes, & Barnes, 1992). The *APALL* routine was used to extract a spectrum from the two dimensional long-slit spectroscopic images. Extracting aperture radii were defined from $0.5r_c$ to $10r_c$ with steps of $1r_c$ from the cluster centers. Sky background regions for the GGCs that do not have separate sky exposures were defined on both sides, well away from the central light profile, avoiding any bright field stars. If one side of the outskirts of a GGC is heavily contaminated by field stars, only the other side is chosen for estimating the sky background. Figure 2.2 shows the flux summed along the dispersion direction, visualizing the spectrum extraction regions of the GGCs and the sky background areas. For those that have separate sky exposures, extraction regions were defined to cover almost the whole area in the spatial axis avoiding any bright stars. Once these extraction windows for the GGCs and sky backgrounds are defined, the *APALL* routine automatically finds a center for the GGCs in the spatial axis, and traces it along the dispersion axis with a 10 pixels step size. It then sums the spectra within the extraction windows previous defined, and subtracts the sky spectrum. During this process cosmic rays are rejected by 3σ clipping. For those that have independent sky exposures (see Table 2.2), sky backgrounds were subtracted manually. Most of the results in this work presented later are derived from spectra with an aperture size of $1r_c$. For the calibration standard stars, a fixed aperture radius was set at 5 pixels with a background region between 10 and 20 pixels on both sides of the object.

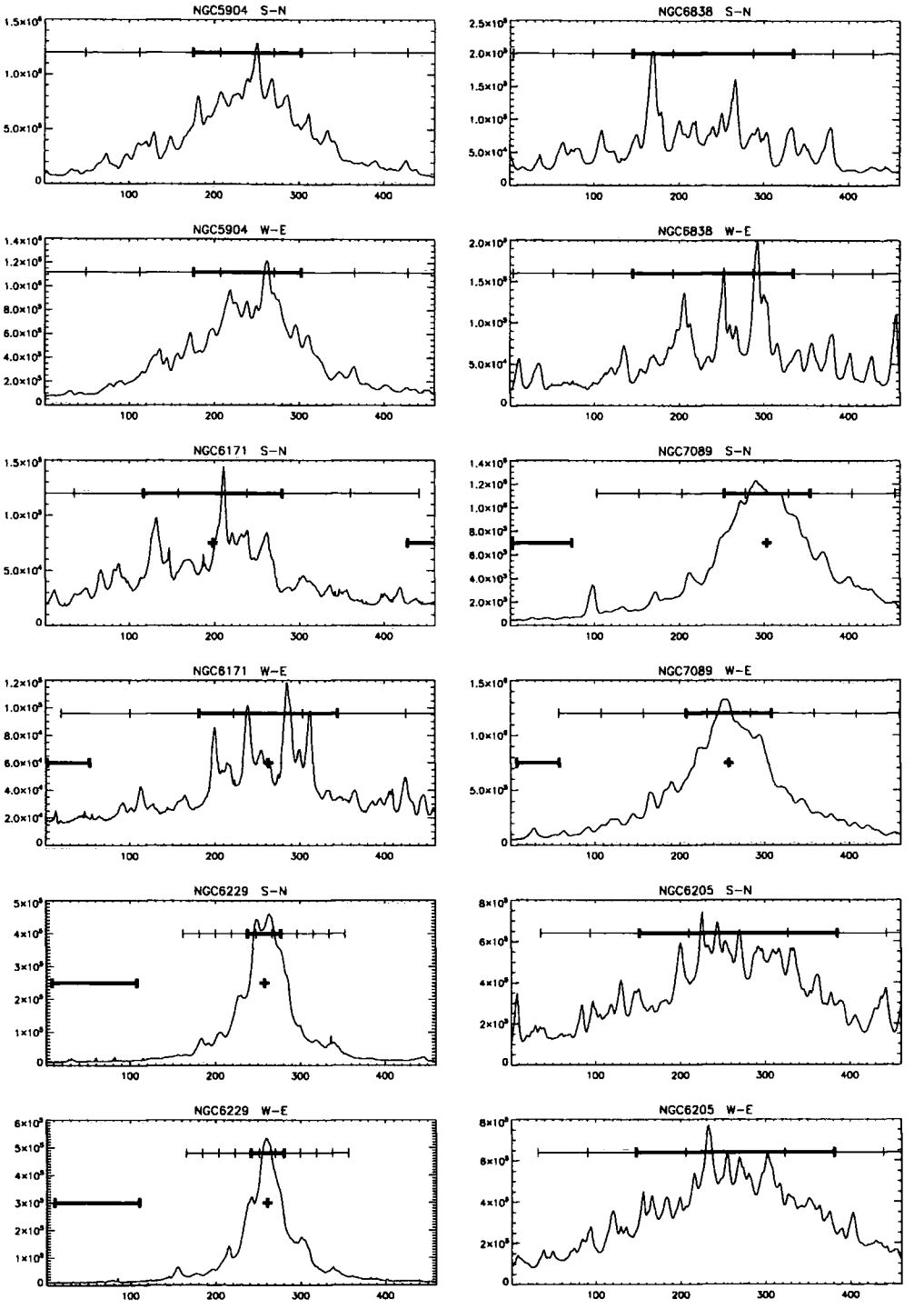

Figure 2.2: Light profiles of the 24 GGCs observed. The profiles were obtained by summing flux along the dispersion axis. In each panel, upper bars indicate various extraction windows with the thick upper bar equal to the size of the core radius. Lower thick bars represent extraction windows of the background sky chosen well away from the globular cluster light.

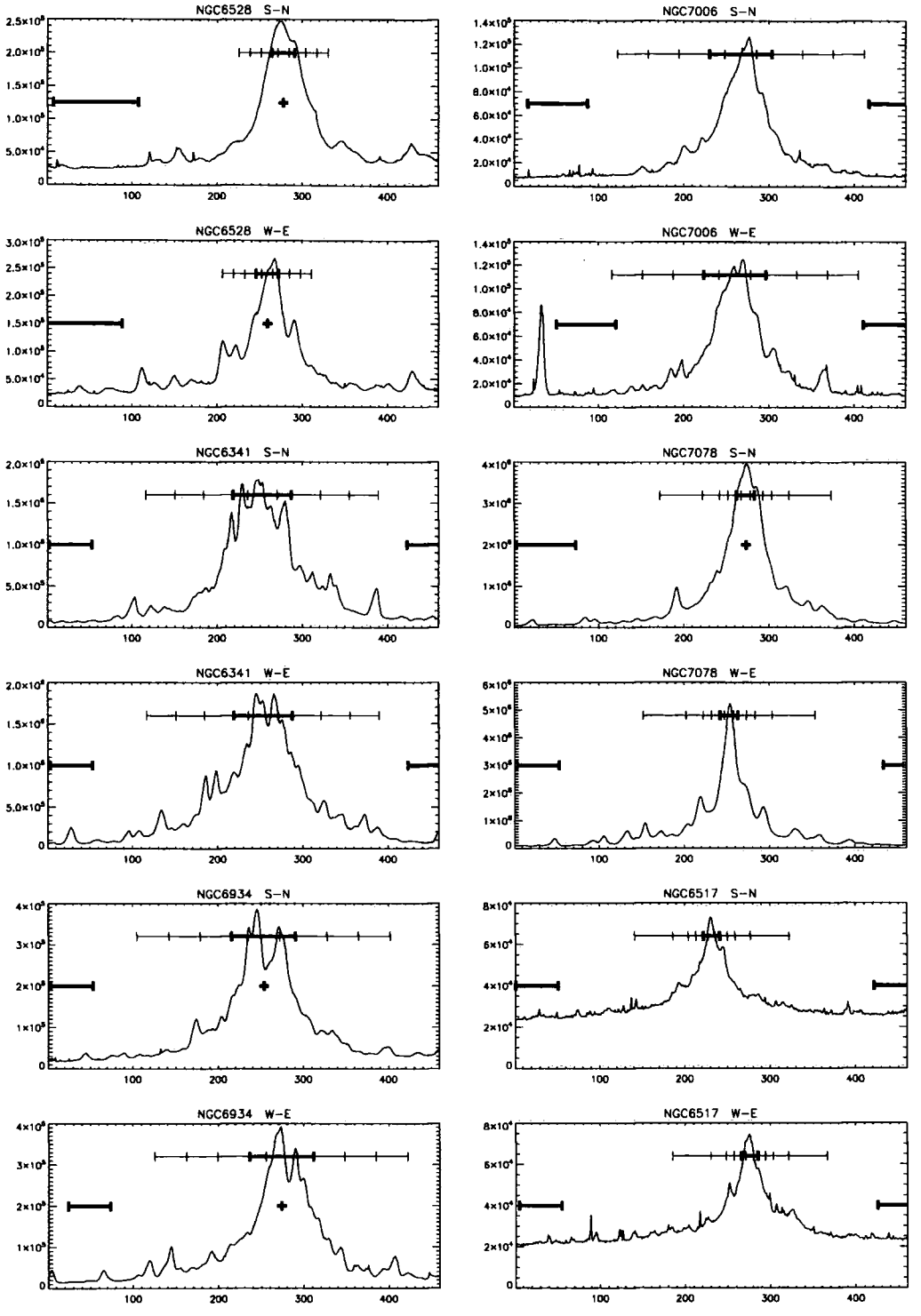

Figure 2.2: Continued.

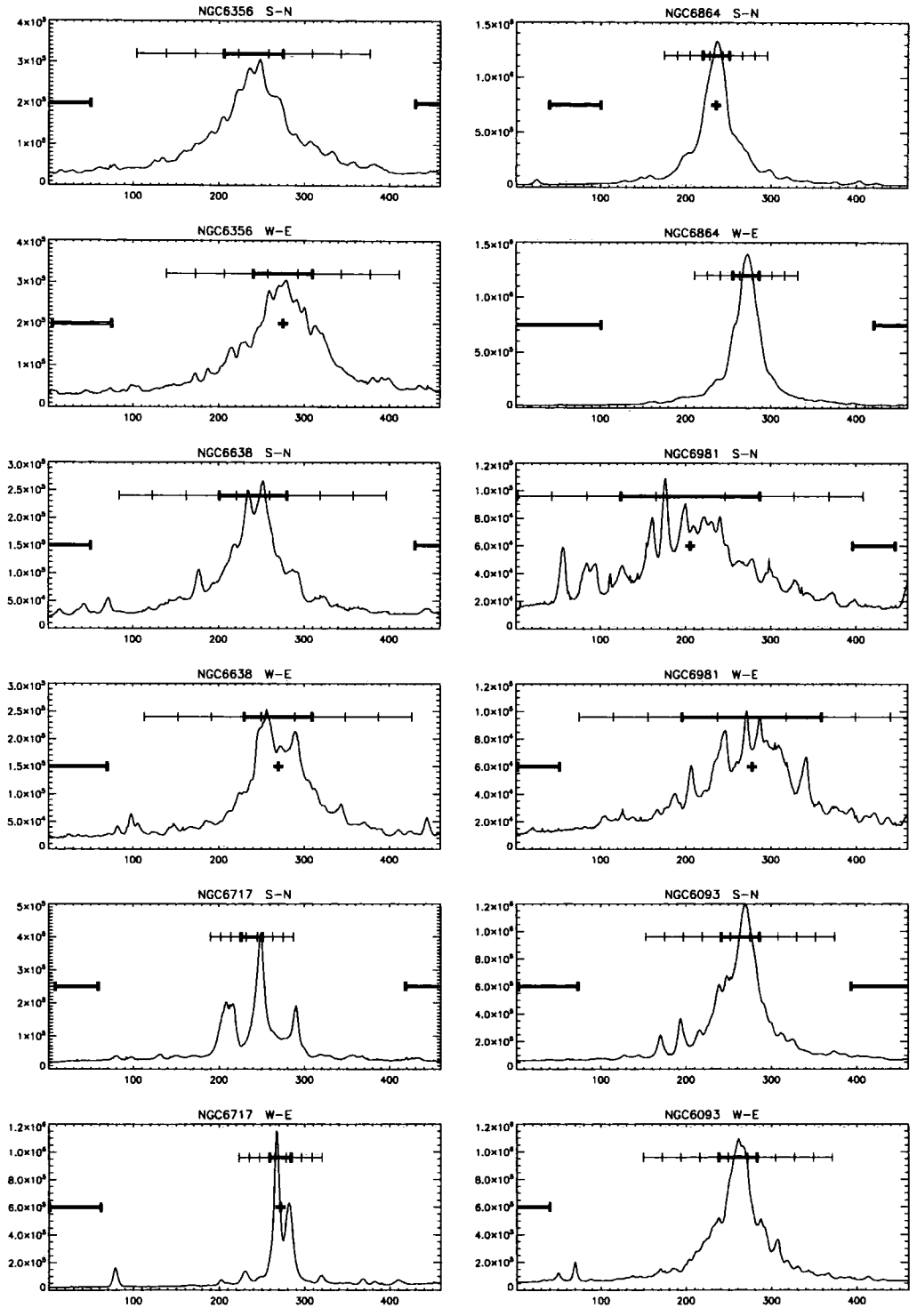

Figure 2.2: Continued.

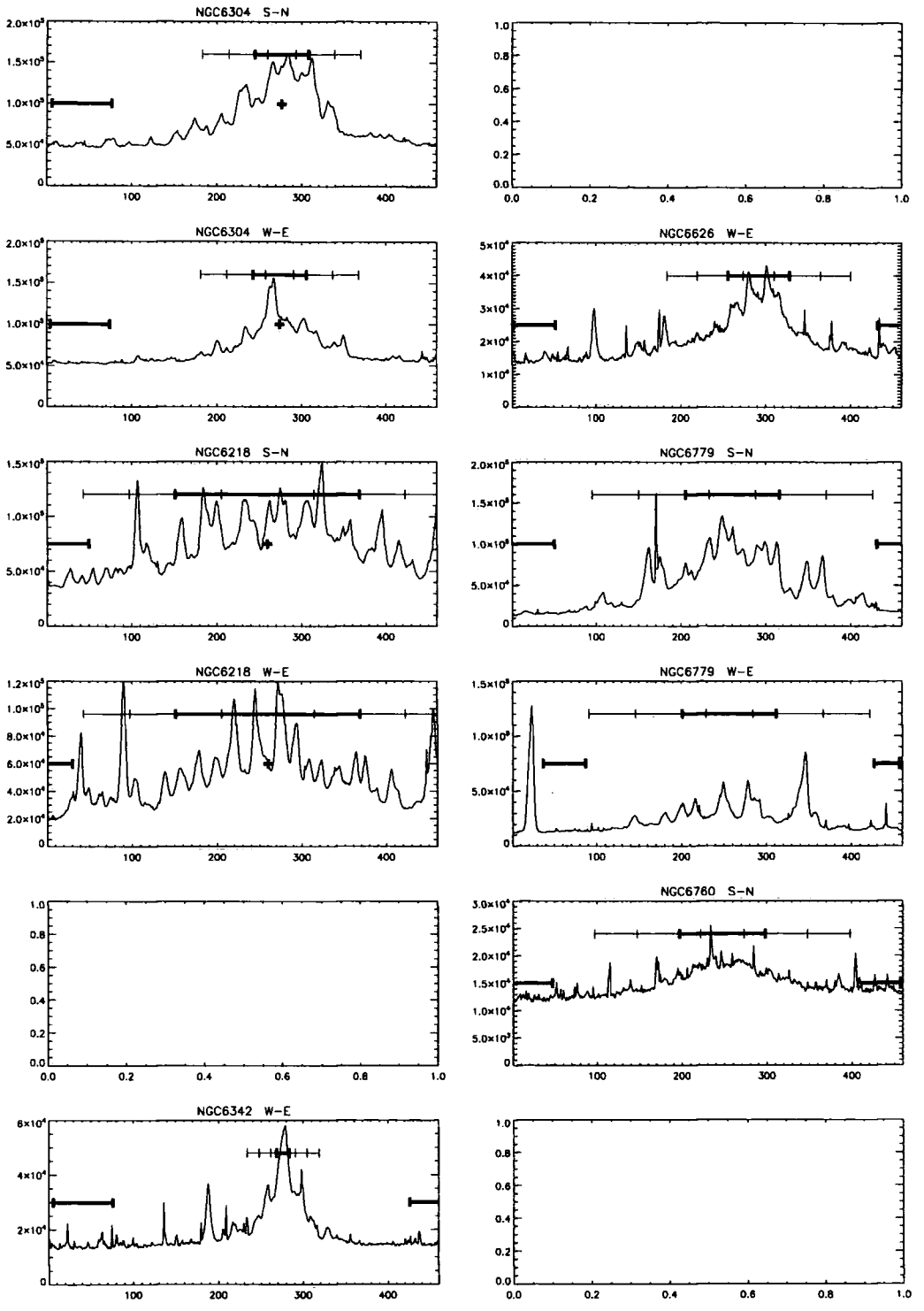

Figure 2.2: Continued.

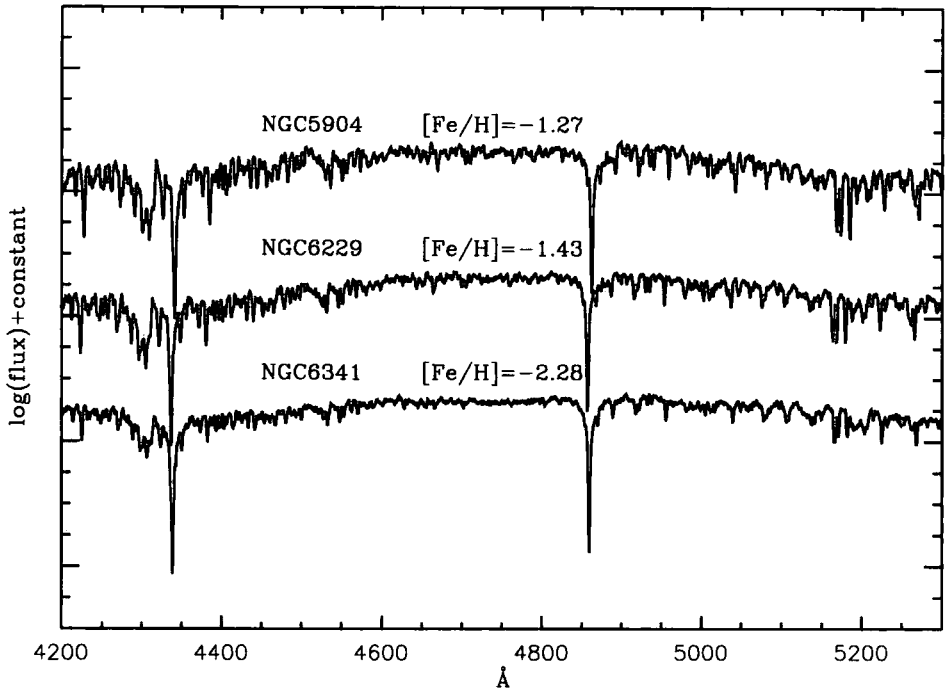

Figure 2.3: Example integrated spectra. Flux and wavelength calibrated spectra are shown for three globular cluster with different metallicities. It is clearly seen that the strength of the Mg line feature near 5150$\AA$ is diminishing with decreasing metallicity.

Using CuAr lines in the arc frames for each target, the science and calibration data were calibrated with an $RMS \sim 0.2\AA$ precision. Finally, the spectrophotometric standard stars Feige110, BD+26-2642,BD+33-2642, and BD+26-2606 (Oke 1990; Massey et al. 1988) were used for flux calibration. Final calibrated spectra have a wavelength range from 4000-5400Å, with an instrumental resolution of FWHM$\sim$ 2.0$\AA$ as measure from the arc frames. Figure 2.3 shows example spectra of three GGCs with various metallicities, showing that metal absorption lines like the Mg line feature around 5150$\AA$ get stronger with increasing metallicity.

To check the self-consistency of our data, and possible contaminations by field stars, we

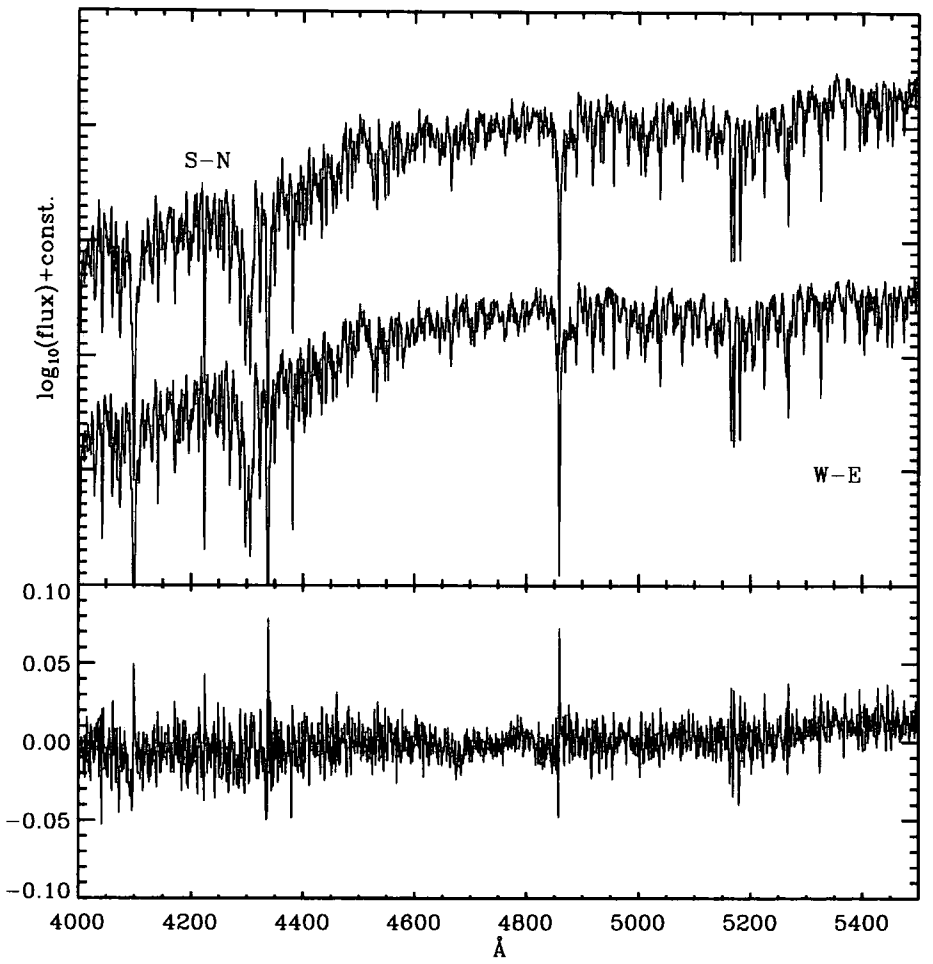

Figure 2.4: Comparison of multiple exposures in NGC6864. The upper panel show spectra of two orthogonal exposures. In the lower panel, the residuals between the two spectra are shown in the unit of dex.

also compared spectra from the two orthogonal slit directions. Figure 2.4 shows spectra of NGC6864 from north-south and west-east directions and their difference. In principle, despite the different drifting directions, the two spectra should be nearly identical because both the drift coverage and the extraction windows are $\pm 1 r_c$ from the center of the cluster, so that the two spectra cover essentially the same region of the cluster (which is the overlapping area defined by the two orthogonal exposures as shown in Figure 2.1). As can be seen in the lower panel of Figure 2.4, the two spectra do show a good agreement with differences less than a few percent. This small residual is probably caused by the different coverage of the sky background extraction regions.

2.2.2 Measurement of radial velocity

Radial velocities of the GGCs were calculated using the *FXCOR* task in IRAF, which computes the Fourier cross correlation between template spectra with a known radial velocity and the input spectra. It is important that the template spectra have a similar spectral type as the input spectra, otherwise, there is a higher chance to mismatch features in the template and object spectra. The template spectra include stars with a range of abundances and also several early-type galaxy spectra. This is a reasonable approach because metal-rich GGCs and early-type galaxies have similar stellar composition with old and metal rich stellar populations. The task was run on a spectrum of each sub-exposure of our sample of GGCs. A radial velocity for each sub-exposure is calculated by averaging the radial velocities measured from the various templates excluding templates for which *FXCOR* fails to return an output. The final value, listed in Table 2.3, is a mean of the radial velocities from different sub-exposures, and the uncertainty was taken to be the standard deviation between sub-exposures. For comparison, the radial velocities from Harris (1996) are also listed. Some GCs with a low S/N ratio fail to retrieve a radial velocity with a sensible value. In terms of an uncertainty, the variation from different templates is found to be relatively small, less

Table 2.3: Radial velocity of GGCs

GC	$V_{r,ref}$ [km/s]	$V_{r,thiswork}$ [km/s]
NGC5904	52.6 ± 0.4	89.1 ± 5.8
NGC6171	-33.6 ± 0.3	-35.2 ± 29.3
NGC6229	-154.2 ± 7.6	-133.5 ± 13.5
NGC6838	-22.8 ± 0.2	-26.4 ± 6.1
NGC7089	-5.3 ± 2.0	-11.4 ± 11.0
NGC6205	-245.6 ± 0.3	-218.1 ± 2.5
NGC6528	206.2 ± 1.5	241.7 ± 21.0
NGC6341	-120.3 ± 0.1	...
NGC6934	-411.4 ± 1.6	-413.9 ± 11.1
NGC7006	-384.1 ± 0.4	-387.4 ± 9.4
NGC7078	-107.0 ± 0.2	...
NGC6517	-39.6 ± 8.0	...
NGC6356	27.0 ± 4.3	48.2 ± 38.1
NGC6638	18.1 ± 3.9	55.2 ± 24.0
NGC6717	22.8 ± 3.4	18.9 ± 37.3
NGC6864	-189.3 ± 3.6	-159.9 ± 20.2
NGC6981	-345.1 ± 3.7	-346.5 ± 24.1
NGC6093	8.2 ± 1.5	41.1 ± 5.4
NGC6304	-107.3 ± 3.6	-77.4 ± 6.7
NGC6218	-42.2 ± 0.5	-19.0 ± 11.1
NGC6342	116.2 ± 1.6	156.3 ± 1.5
NGC6626	17.0 ± 1.0	29.1 ± 7.1
NGC6779	-135.7 ± 0.8	...
NGC6760	-27.5 ± 6.3	...

The radial velocities in the first column come from (Harris, 1996), while the measurement from this work is list in the second column. Results with a large uncertainty are omitted.

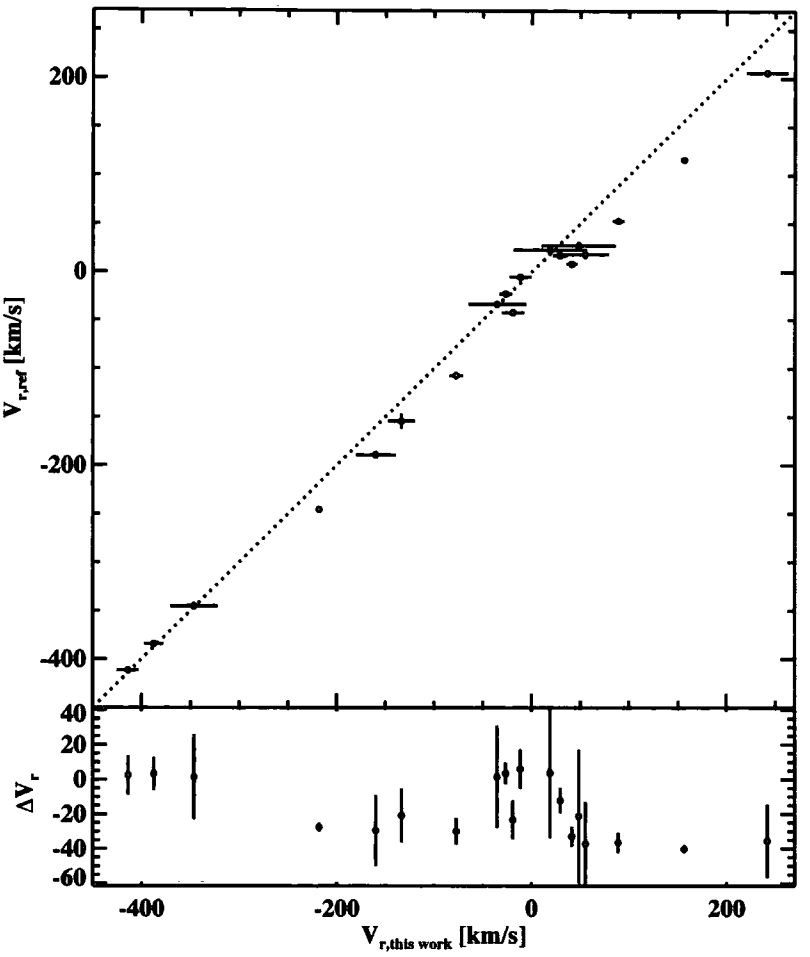

Figure 2.5: Comparison of radial velocities for Galactic globular clusters. In the upper panel our measurements are on the x-axis and the values from Harris (1996) are on the y-axis. The dotted line is the one-to-one relation. The data points are listed in Table 2.3. In the bottom panel differences of the two measurements, $\Delta V_r = V_{r,ref} - V_{r,this\ work}$, are plotted.

than 10km/s, while the one from multiple exposures appear higher up to $\sim$ 30km/s.

2.2.3 Measurement of Lick indices

The most common way to measure an integrated line strength in stellar systems is by defining a passband covering a line feature and measuring flux through that passband relative to an adjacent continuum. The Lick standard system is the most widely used index system. Since Burstein et al. (1984)'s introduction of this system, it has been renewed and upgraded by many authors (Worthey et al. 1994; Worthey & Ottaviani 1997; Trager et al. 1998). The most recent definition of the passbands of the Lick/IDS system is the combination of Trager et al. (1998) and Worthey & Ottaviani (1997), consisting of 25 line indices (Table 2.4). in an optical region of wavelength (4000Å$\lesssim \lambda \lesssim$ 6500Å). Figure 2.6 shows the exact positions of the Lick line index bands and pseudo-continuum passbands superimposed on the spectrum of NGC7089. Fluctuations in this spectrum are not noise but actual features with a high signal to noise.

When measuring the Lick indices, there are several things to be taken into account. A radial velocity is used to correct the spectra to the rest frame. The adopted radial velocities are our measurement for individual exposures, but for the GGCs for which we fail to measure a radial velocity from our spectra, the radial velocities from Harris (1996) were used. Since the Lick/IDS systems has a lower resolution($\sim$10Å) than ours ($\sim$2.0Å), our spectra also have to be degraded. Unlike galaxies, the GGCs have a low velocity dispersion of less than 10km/s (Dubath et al., 1997) so that line broadening by their velocity dispersion is negligible. The actual IDL script used for line index measurement processing was kindly provided by Harald Kuntschner at ESO.

In order to calibrate to the standard Lick/IDS system, the indices of the 47 Lick standard stars were first measured. Because of the limited wavelength of $4000\mathring{A} \lesssim \lambda \lesssim 5400\mathring{A}$ available in our spectra, measurements are restricted to 20 indices, excluding the 5 longest

Table 2.4: Index definition of the Lick/IDS system

Line index	Index band	blue continuum	red continuum	Units
CN_1	4142.125 4177.125	4080.125 4117.625	4244.125 4284.125	mag
CN_2	4142.125 4177.125	4083.875 4096.375	4244.125 4284.125	mag
Ca4227	4222.250 4234.750	4211.000 4219.750	4241.000 4251.000	Å
G4300	4281.375 4316.375	4266.375 4282.625	4318.875 4335.125	Å
Fe4383	4369.125 4420.375	4359.125 4370.375	4442.875 4455.375	Å
Ca4455	4452.125 4474.625	4445.875 4454.625	4477.125 4492.125	Å
Fe4531	4514.250 4559.250	4504.250 4514.250	4560.500 4579.250	Å
Fe4668	4634.000 4720.250	4611.500 4630.250	4742.750 4756.500	Å
$H\beta$	4847.875 4876.625	4827.875 4847.875	4876.625 4891.625	Å
Fe5015	4977.750 5054.000	4946.500 4977.750	5054.000 5065.250	Å
Mg_1	5069.125 5134.125	4895.125 4957.625	5301.125 5366.125	mag
Mg_2	5154.125 5196.625	4895.125 4957.625	5301.125 5366.125	mag
Mg_b	5160.125 5192.625	5142.625 5161.375	5191.375 5206.375	Å
Fe5270	5245.650 5285.650	5233.150 5248.150	5285.650 5318.150	Å
Fe5335	5312.125 5352.125	5304.625 5315.875	5353.375 5363.375	Å
Fe5406	5387.500 5415.000	5376.250 5387.500	5415.000 5425.000	Å
Fe5709	5696.625 5720.375	5672.875 5696.625	5722.875 5736.625	Å
Fe5782	5776.625 5796.625	5765.375 5775.375	5797.875 5811.625	Å
Na_D	5876.875 5909.375	5860.625 5875.625	5922.125 5948.125	Å
TiO_1	5936.625 5994.125	5816.625 5849.125	6038.625 6103.625	mag
TiO_2	6189.625 6272.125	6066.625 6141.625	6372.625 6415.125	mag
$H\delta_A$	4083.500 4122.250	4041.600 4079.750	4128.500 4161.000	Å
$H\gamma_A$	4319.750 4363.500	4283.500 4319.750	4367.250 4419.750	Å
$H\delta_F$	4091.000 4112.250	4057.250 4088.500	4114.750 4137.250	Å
$H\gamma_F$	4331.250 4352.250	4283.500 4319.750	4354.750 4384.750	Å

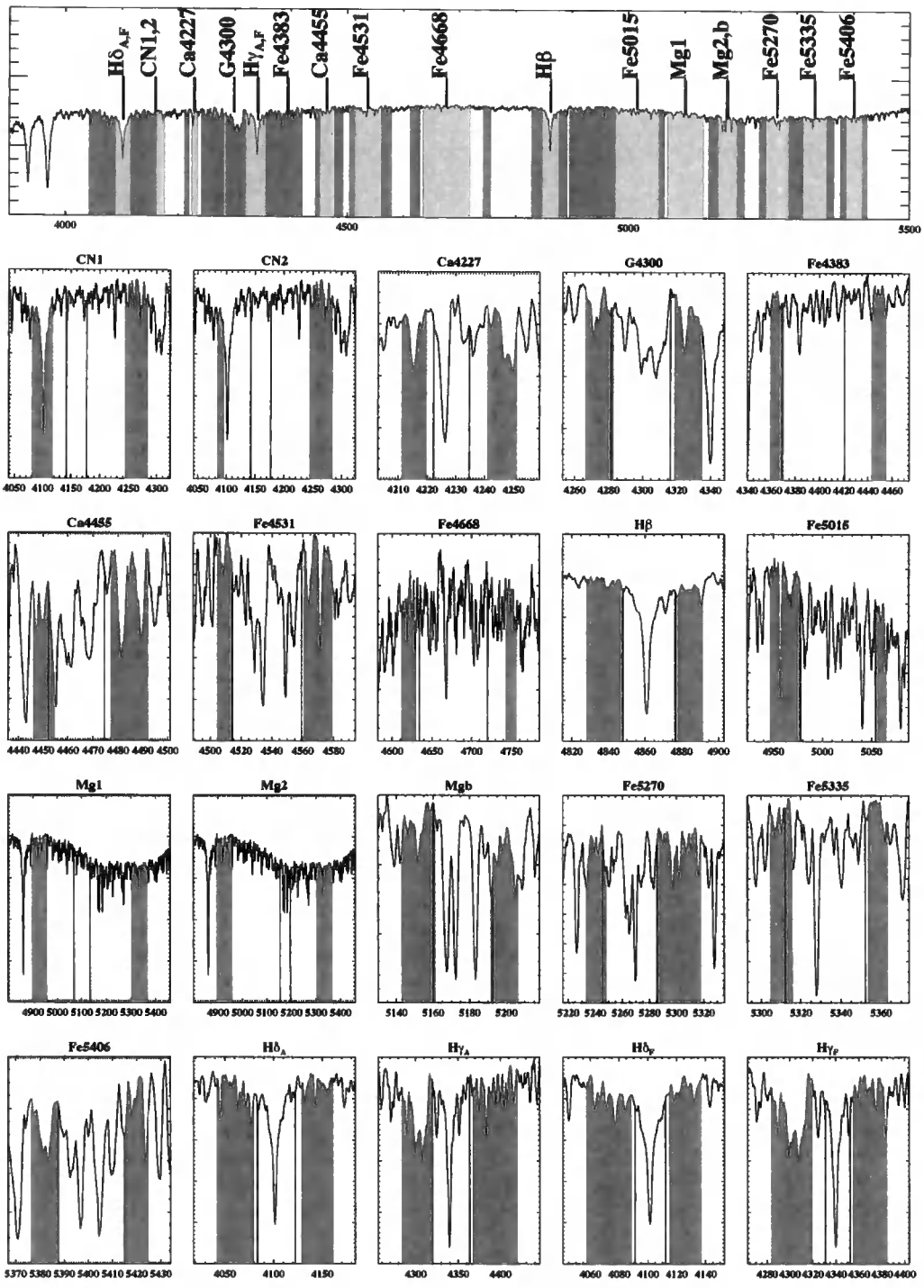

Figure 2.6: Spectrum of NGC7089 with Lick line index passbands superimposed. In the top panel, the position of all line indices are indicated on the spectrum of NGC7089. Dark shaded areas are pseudo-continuum passbands, and light shaded areas line index passbands. The lower 20 panels are a zoom-in of individual line index passbands.

Table 2.5: Offsets for Lick indices of standard stars

Line index	offset	Line index	offset
CN_1	0.0071±0.0004mag	Mg_1	0.0034±0.0001mag
CN_2	0.013±0.001mag	Mg_2	0.0050±0.0002mag
Ca4227	0.00±0.01Å	Mg_b	-0.086±0.008Å
G4300	-0.31±0.01Å	Fe5270	-0.09±0.01Å
Fe4383	0.19±0.02Å	Fe5335	-0.13±0.01Å
Ca4455	0.22±0.01Å	Fe5406	-0.05±0.01Å
Fe4531	0.05±0.01Å	$H\delta_A$	-0.70± 0.01Å
Fe4668	-0.83±0.02Å	$H\gamma_A$	0.01 ± 0.01Å
$H\beta$	-0.14±0.01Å	$H\delta_F$	-0.37 ± 0.01Å
Fe5015	0.34±0.01Å	$H\gamma_F$	0.03 ± 0.01Å

wavelength ones (Fe5709, Fe5782, Na_D, TiO_1, TiO_2). In Figure 2.7, the indices measured for our standard stars by Worthey & Ottaviani (1997) and Worthey et al. (1994) are compared with our results. They generally show a good one-to-one relation. The offsets between our indices and Lick standard measurements were calculated by linear fitting with a unit slope after 2σ clipping. The offsets, $\Delta_{index} = EW_{Lick} - EW_{thiswork}$, are listed in Table 2.5. The line indices of our GGCs were measured independently from the multiple exposures. Our final Lick/IDS calibrated indices were obtained by adding these offset values to the initial measurement of the indices of the GGCs and averaging multiple exposures of the same cluster. Two kinds of uncertainties for the line indices were estimated. Random errors were estimated by Monte-Carlo simulations with a noise map produced by the *IRAF/APALL* task. Systematic errors were estimated by calculating a standard deviation from the different scan directions and multiple exposures.

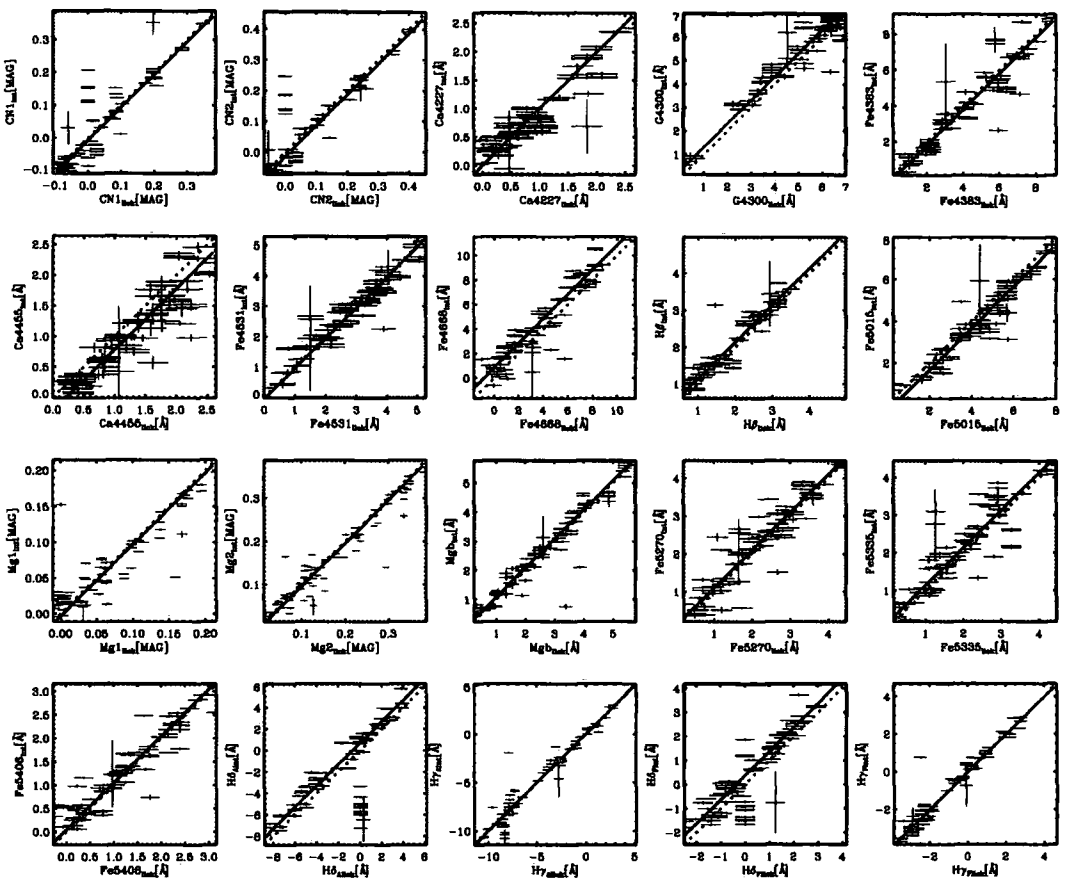

Figure 2.7: Comparison of 20 Lick indices for 47 Lick standard stars. Lick measurements from Worthey & Ottaviani (1997) and Worthey et al. (1994) are on the x-axis, and our measurements are on the y-axis. The dotted line is the one-to-one relation. The solid line is a weighted linear fit with unit slope after 2σ rejection of outliers.

Bright stars can often dominate the integrated light measurements whether they are members of the GC or foreground stars. It is thus important to check if errors caused by stochastic variations of bright stars are significant compared to random errors or the systematic errors measured by multiple exposures and different scan directions. First we search for a GC with a light profile having sharp and well resolved spikes, and a GC with a smooth intensity profile. These correspond to the extreme cases where the integrated light is either dominated by individual bright stars (first case) or by the large numbers of faint stars (second case). A NGC6171 W-E exposure was chosen for the former case, while an NGC7089 W-E exposure was selected for the latter case (see the fourth pair of graphs from the top in the first page of Figure 2.2). Two spectra were then extracted from each side within a core radius from the GC center with the same sky subtraction area and the Lick indices were measured independently. It is found that the errors of the indices of NGC6171 are in general much greater than those of NGC7089. For example, the error of Mgb index of NGC6171 and NGC7089 are 0.23$\AA$ and 0.03$\AA$ respectively. However, the errors introduced by bright stars are comparable to the random errors. In fact the random errors of NGC6171 are greater than those of NGC7089. Therefore, the effects due to variations of bright stars are relatively insignificant in the cases studied.

2.3 Results

2.3.1 Comparison with previous studies

Integrated spectra of GGCs have been carried out by various authors (e.g. Burstein et al. 1984; Covino et al. 1995; Trager et al. 1998; Puzia et al. 2002b, hereafter PSK02; Schiavon et al. 2005, hereafter SRC05). The most recent two studies (PSK02; SRC05) have been compared with our results to check consistency. PSK02 observed 12 GGCs mainly associated with the Galactic bulge using the ESO 1.52m telescope in La Silla, and measured all 25 Lick

line indices. SRC05 obtained integrated spectra of 41 GGCs with the Cerro Tololo Inter-American Observatory (CTIO) Blanco 4m telescope, but released only calibrated spectra with FWHM ~3.1Å. We measured Lick line indices for the SRC05 spectra in the same way as we treated our own spectra. There are 5 common GCs between ours and PSK02, 11 common GCs between ours and SRC05, and 4 common GCs in all the three sources.

In Figure 2.8, our results and the two previous studies are compared, showing a good agreement in general. Index offsets, $\Delta_{ref} = EW_{thiswork} - EW_{ref}$, are computed by weighted linear fitting with unit slope (Table 2.6). The Fe4531 and Fe5015 indices of SRC05 have a large offset from our data. This is probably due to CCD defects or poorly subtracted sky emission lines (see Figure 2 in SRC05) in their work; this problem is also mentioned by Mendel et al. (2007). Figure 2.9 shows spectra of NGC7078 from this work and SRC05 in the region of the Fe4531, Fe5015, and Mgb Lick passbands. It is clear that many data points in the SRC05 spectra are missing. The Mgb feature also demonstrates that our spectra have a higher wavelength resolution than SRC05, showing that some adjacent absorption lines are resolved in our spectra, but not in SRC05. The three datasets have been merged to form a new dataset of Lick line indices for 53 GGCs with a wide range of ages and metallicities using the offsets from Table 2.6 to correct all data to our system. For the common GCs, our results are used in preference to the others. We excluded indices of NGC6760 from our data due to a low signal to noise ratio of its spectrum (see the last panel of Figure 2.2). This combined dataset is used below for further analysis.

2.3.2 Comparison with SSP Models

Since globular star clusters are the best example of stellar systems which contain only one stellar population, they are the ultimate testbed for Simple Stellar Population (SSP) models. In order to investigate the stellar properties of unresolved stellar systems, it is essential to calibrate SSP models to the most recent observational GGC data available. The SSP models

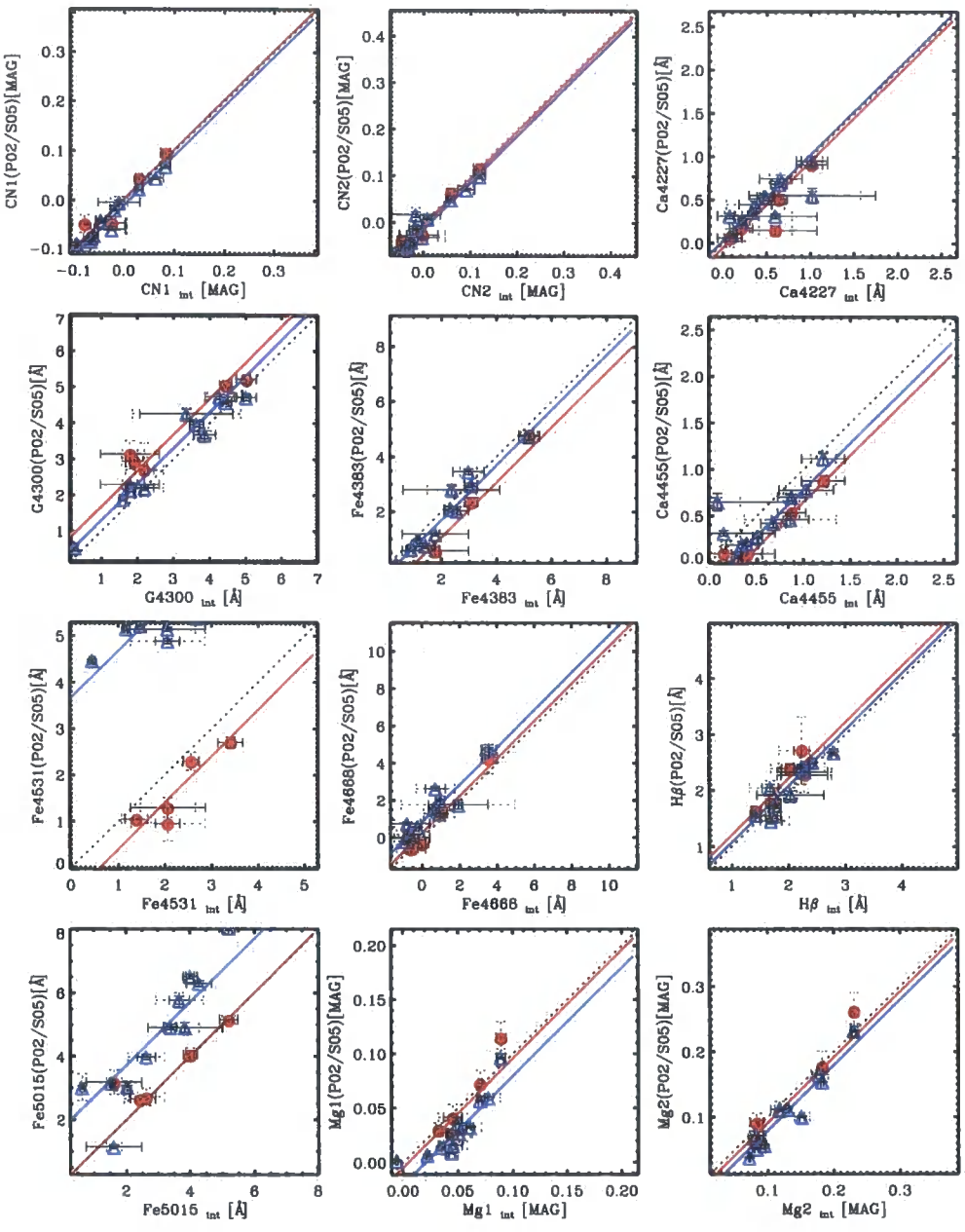

Figure 2.8: Comparison of line index measurements for Galactic globular clusters with measurements from PSK02 (red filled circles) and SRC05 (blue triangles). Dotted lines are the one-to-one relations. Solid lines show the weighted linear fit with unit slope. The solid error bar is the random error, and the dotted error bar represents an additional systematic error estimated from the variations between different scan directions and multiple exposures in our data.

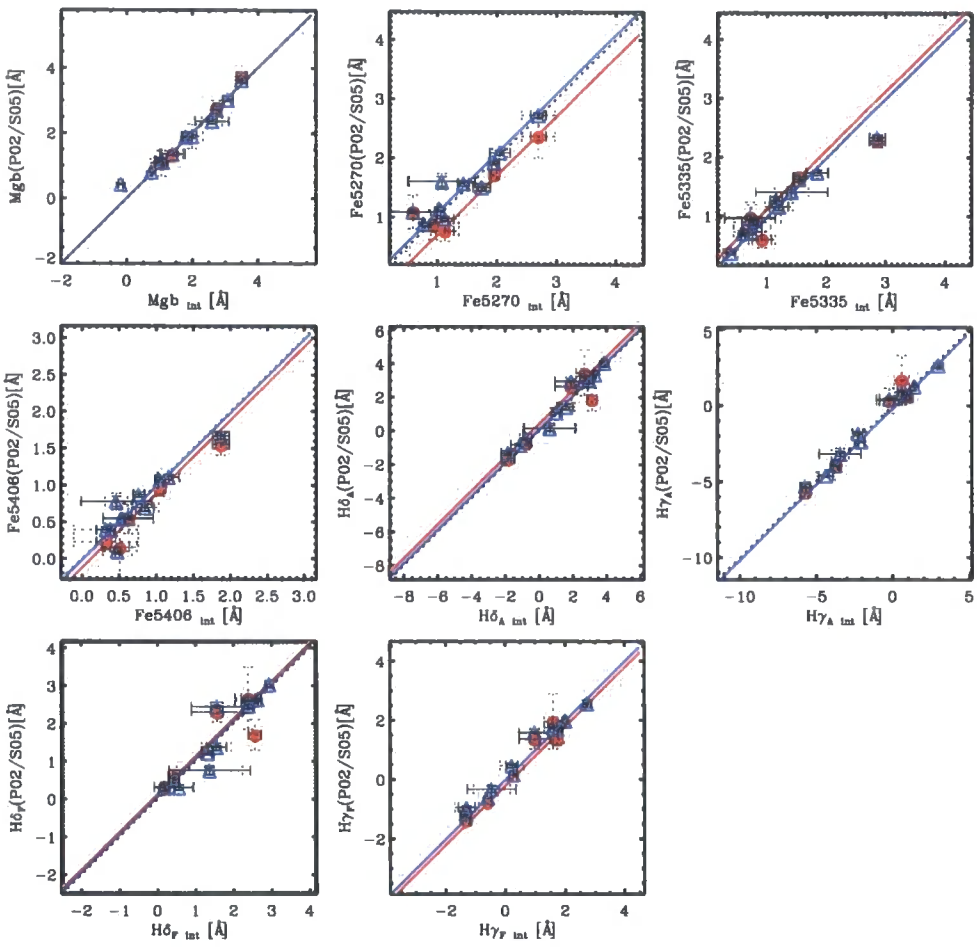

Figure 2.8: continued.

Table 2.6: Offsets of Lick indices for previous studies of GGCs

Line index	Δ_{PSK02}	Δ_{SRC05}
CN_1	-0.0062± 0.0004mag	0.008 ± 0.001mag
CN_2	0.0020± 0.0004mag	0.012 ± 0.001mag
Ca4227	0.04 ± 0.01Å	-0.03 ± 0.01Å
G4300	-0.73 ± 0.01Å	-0.32 ± 0.02Å
Fe4383	0.88 ± 0.02Å	0.29 ± 0.03Å
Ca4455	0.34 ± 0.01Å	0.21 ± 0.01Å
Fe4531	0.57 ± 0.02Å	-3.69 ± 0.02Å
Fe4668	-0.31 ± 0.04Å	-0.87 ± 0.03Å
$H\beta$	-0.23 ± 0.01Å	-0.09 ± 0.01Å
Fe5015	-0.06 ± 0.04Å	-1.72 ± 0.04Å
Mg_1	0.0029 ± 0.0005mag	0.0201 ± 0.0003mag
Mg_2	0.0061 ± 0.0004mag	0.0197 ± 0.0004mag
Mg_b	-0.047 ± 0.019Å	-0.029 ± 0.012Å
Fe5270	0.28 ± 0.02Å	-0.08 ± 0.01Å
Fe5335	-0.13 ± 0.03Å	0.01 ± 0.02Å
Fe5406	0.09 ± 0.02Å	0.01 ± 0.01Å
$H\delta_A$	-0.52 ± 0.01Å	-0.15 ± 0.02Å
$H\gamma_A$	0.17 ± 0.02Å	0.16 ± 0.02Å
$H\delta_F$	-0.17 ± 0.01Å	-0.08 ± 0.01Å
$H\gamma_F$	0.17 ± 0.01Å	0.01 ± 0.01Å

$$\Delta_{PSK02} = EW_{thiswork} - EW_{PSK02},$$

$$\Delta_{SRC05} = EW_{thiswork} - EW_{SRC05}$$

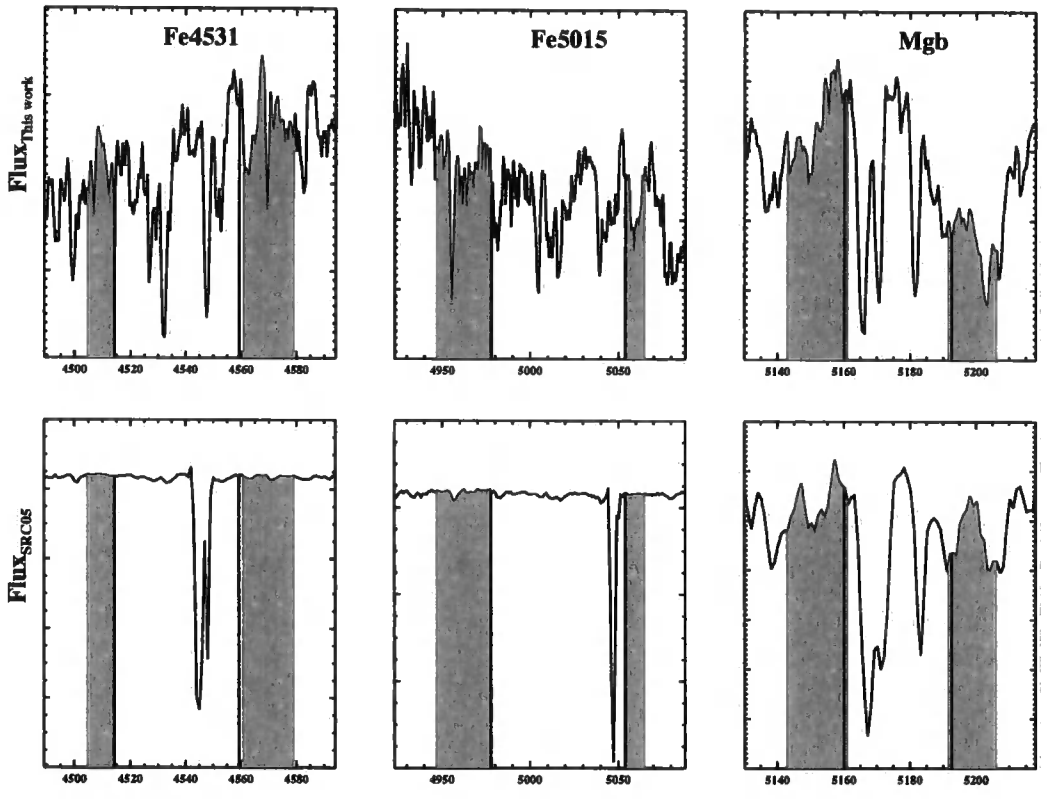

Figure 2.9: NGC7078 spectra within Fe4531, Fe5015, and Mgb Lick passbands. The upper panels are spectra from this work, and the lower panels come from SRC05. The spectra around Fe4531 and Fe5015 from SRC05 are heavily interpolated, and their spectra have a lower spectral resolution than this work.

to be compared with our compiled data set are taken from Thomas et al. (2003, hereafter TMB03) and Lee & Worthey (2005, hearafter LW05). The TMB03 models are based on evolutionary stellar synthesis models from Maraston (1998), and include 21 Lick indices from CN_1 to TiO_2 in the wavelength range $4000\mathring{A} \lesssim \lambda \lesssim 6500\mathring{A}$. These models cover a range of α-element abundances, metallicities and ages: [α/Fe]=0.0, 0.3, 0.5, -2.25$\leq$[Z/H]$\leq$0.67, ages from 1 to 15Gyr. Subsequent work by Thomas et al. (2004, hereafter TMK04) extended this to include the four higher-order Balmer line indices ($H\delta_A$, $H\gamma_A$, $H\delta_F$, $H\gamma_F$). LW05 adopted the Yale isochrones from Kim et al. (2002) coupled with post-red giant branch evolutionary tracks by Yi et al. (1997), and computed all 25 Lick indices including the higher-order Balmer line indices. These models cover a metallicity range of -2.5$\leq$[Fe/H]$\leq$+0.5, an age range from 1 to 12 Gyr, and included α-enhancements of [α/Fe]=0.0, 0.3, and 0.6.

Figure 2.10 shows various line indices plotted against the Mgb line index for our compiled observational data and 12 Gyr old SSP models from TMB03 and LW05. In Figure 2.11, the higher-order Balmer line indices are plotted against [MgFe]'[1]. In general, the two SSP models behave similarly across the range of metallicities without a big offset. At low metallicity, [Fe/H]$\lesssim$-1.5, however, the two models appear to deviate in the Balmer lines vs. Mgb plot. The Balmer line indices increase steeply at lower metallicities in the TMB03's models, while they are flatter below [Fe/H]$\lesssim$-1.5 in LW05. This discrepancy seems to be due to the different way in which the two models treat horizontal branch (HB) stars.

The Balmer absorption lines are strongest in stars with around $T = 10,000K$ (A-type stars). The main stellar components to govern the Balmer line strength are therefore main sequence stars with ages $\sim$1Gyr so that the Balmer lines get weaker as stellar populations get older. Thus, often Balmer lines are regarded as primarily an age indicator of stellar populations. However, main sequence stars are not the only contributor to the Balmer lines. Blue HB stars, which are in a core helium burning stage following red giant branch evolution,

[1] $[MgFe]' \equiv \sqrt{Mgb(0.72 \times Fe5270 + 0.28 \times Fe5335)}$ as defined by TMB03

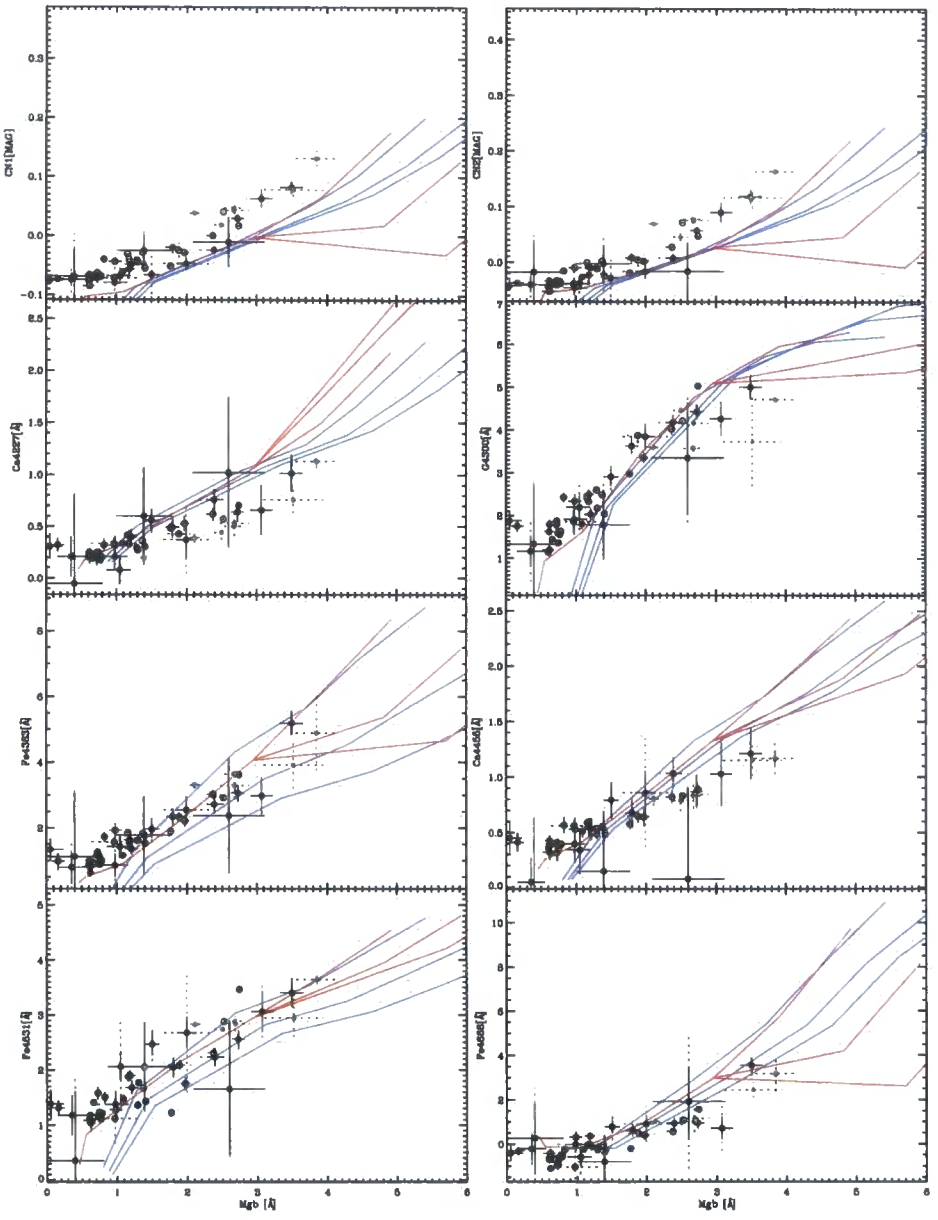

Figure 2.10: Mgb vs various line indices with simple stellar population models superimposed. The solid circles are our GGC sample, the shaded circles are from PSK02, and open circles from SRC05. The solid error bar is the random Poisson error, and the dotted error bar represents an additional systematic error estimated from the variations between different scan directions and exposures. Two different SSP models are overplotted. Blue lines are from TMB03 with a metallicity range 2.25≤[Z/H]≤0.67 and [α/Fe]=0.0, 0.3, 0.5 (lower ordinate values correspond to increasing [α/Fe]). Red lines show models from LW05 with [α/Fe]=0.3 over the metallicity range -2.5≤[Fe/H]≤-1.0, [α/Fe]=0.15 at [Fe/H]=-0.5, and [α/ Fe]=0.0,0.3,0.6 at [Fe/H]=0.0 and 0.5. Both models are for an age of 12 Gyr.

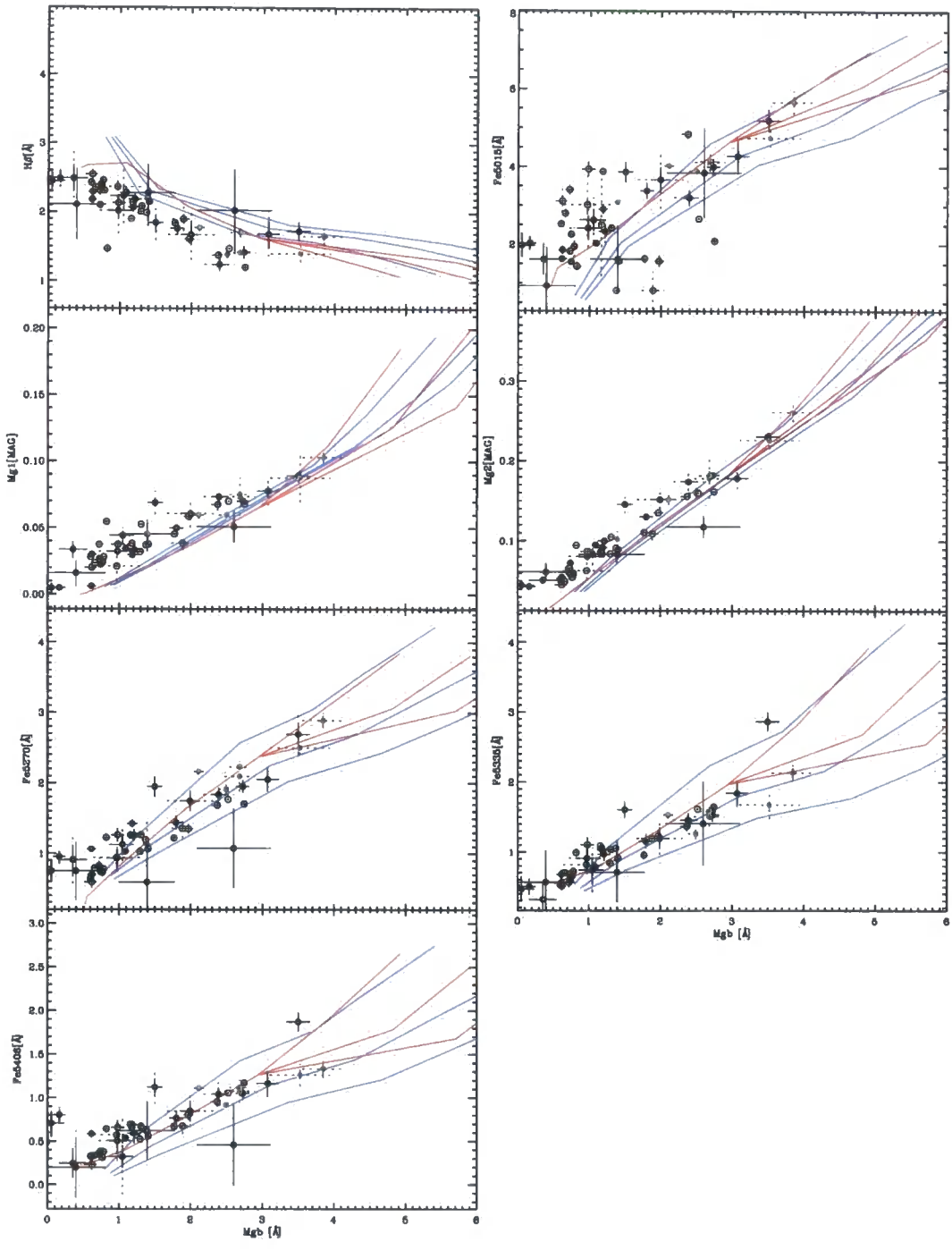

Figure 2.10: Continued

can also contribute strongly to the strength of the Balmer line. Therefore, the number and morphology of HB stars are an important component of stellar synthesis models.

Maraston & Thomas (2000) modified Maraston (1998)'s standard model in order to reproduce the Balmer line strengths in the GGC sample of Burstein et al. (1984), Covino et al. (1995), and Trager et al. (1998) by implementing mass loss at the red giant branch tip. This additional mass-loss makes HB stars appear to be hotter by stripping more mass from the outer shell of HB stars, thus resulting in stronger Hβ lines. This was calibrated using the PSK02 GGC sample by Maraston et al. (2003). On the other hand, LW05 follow the earlier works by Lee at al. (2000, 2002) that adopt a systematic variation of HB morphology with age and metallicity; the older GCs are, the bluer their HB stars are, and the metal poorer GCs are, the bluer their HB stars. Our observational data appear to track closer to LW05's models in the Balmer and Mgb line index spaces, although our Balmer indices are somewhat flatter than LW05's model in the very metal poor region (see top-left panel in the second page of Figure 2.10 and Figure 2.11). Beasley et al. (2005) also found a mismatch between their M31 GC sample and TMB03 models in that the M31 GC Balmer line indices tend to be weaker at low metallicities. Beasley et al. (2005) find a better agreement with TMB03 models without mass-loss on the red giant branch (see Figure 3 in Beasley et al. (2005)). LW05 also claim that their own models agree well with observations of Galactic and M31 GCs without any zero-point shifts.

Some other lines (G4300, Fe4383, Ca4455, and Fe4531) in Figure 2.10 also show some disagreements in the metal poor region between TMB03 and LW05. The different treatments of HB stars can certainly have an effect on other absorption lines. Once again our compiled GGC dataset have a better agreement with LW05 than TMB03 at low metallicity. The Fe5015 vs. Mgb plot in Figure 2.10 shows a large scatter for the SRC05 data (open circles). This seems to be due to the poor quality of data for Fe5015 in SRC05 as mentioned in §2.3.1.

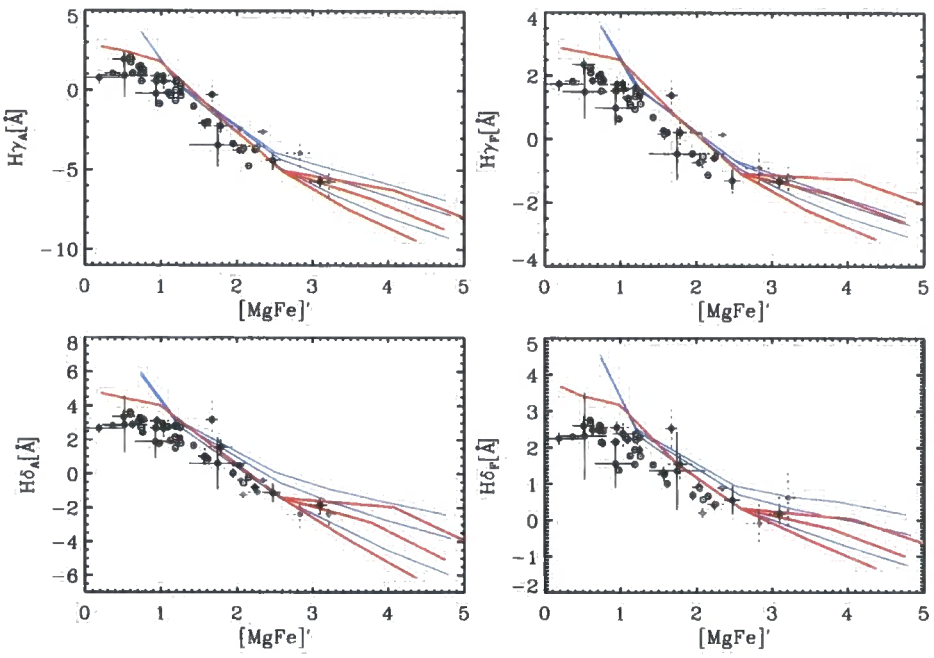

Figure 2.11: Higher order Balmer line indices against [MgFe]′, which is defined as $\sqrt{Mgb(0.72 \times Fe5270 + 0.28 \times Fe5335)}$ by TMB03. All the symbols and lines are the same as in Figure 2.10 except the blue model lines come from TMK04.

2.3.3 Radial gradients of line indices

Radial changes of stellar population within GGCs have been suggested in many previous spectroscopic and photometric studies. An increase in the strength of the Balmer absorption lines toward the centres of M30 and NGC4147 was found by Zinn & West (1984), Hesser & Shawl (1985), and Rose et al. (1987). Colour gradients in which the central regions are bluer than the outer parts of GCs have also been found in many post core collapse clusters like M15, M30, NGC6397, and NGC6752 (e.g. Djorgovski et al. 1991a; Djorgovski et al. 1991b; Cederbloom et al. 1992; Guhathakurta et al. 1998; Howell et al. 2000). Sohn et al. (1996) detect colour gradients even in GCs with King-type surface brightness profile which is rather flatter than the post core collapse morphology in the central part. This colour gradient could be due to the depletion of red giant stars caused by mass segregation (Howell et al., 2000), and/or because the dense environments in the center of GCs can result in stellar encounters and enhancement of stellar binary systems, which produce hot stars such as blue stragglers and blue horizontal branch stars (Djorgovski & Piotto, 1992).

We have investigated whether there is any evidence for radial gradients of the line indices in our sample of GGCs. As stated in §2.2.1, we retrieved spectra within various aperture sizes and measured the Lick line indices of those spectra independently. The final values were calculated by averaging the line indices from multiple exposures. Figure 2.12 shows the metallicity sensitive line index of Mgb, and the age sensitive line index of Hβ plotted against radial distance from the center of each GC. Most GCs in our sample show little evidence of line index gradients in Hβ and Mgb. Even GCs in which colour gradients have been detected previously (e.g. NGC7078, NGC7089, and NGC6934) do not have any strong trend in our results. This is possibly because in order to achieve a sufficient S/N our measurements of line indices enclose light within a circular aperture, not within an annulus, resulting in cumulative measurements. It is difficult therefore to rule out whether or not a weak line index gradient does exist in some of GGCs.

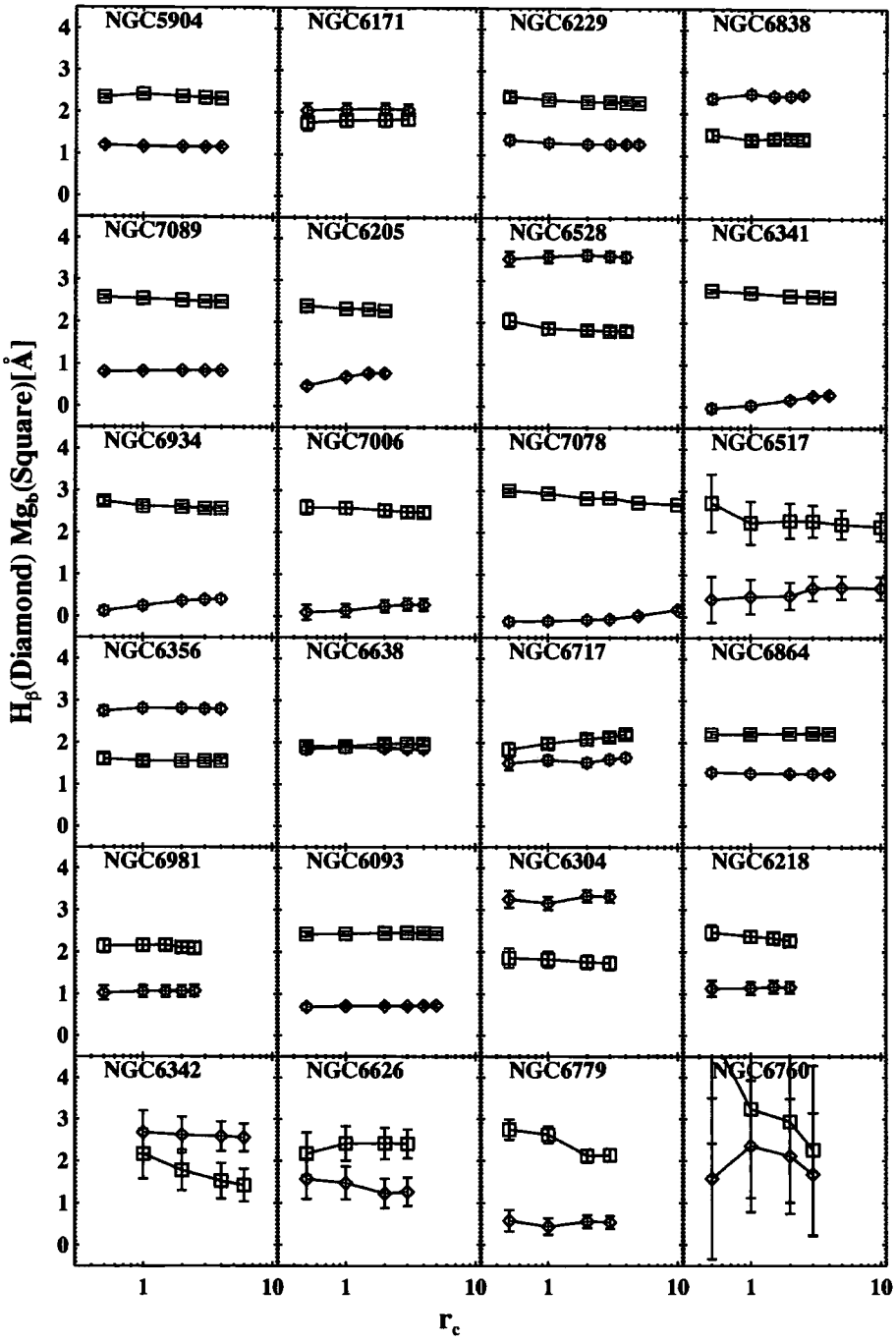

Figure 2.12: Line indices against radial distance our sample GCs. The line indices were measured from spectra that contain GC light within a given radial distance. The diamonds symbols represent an age sensitive line index of Hβ, and the square symbols are a metallicity sensitive index of Mgb. The Y-axis is the unit of core radius.

2.4 Conclusions

- We have obtained integrated spectra of 24 Galactic globular clusters with a high spectral resolution of $FWHM \sim 2\AA$ and a high S/N of ~ 30 using the 2.5m Isaac Newton Telescope in La Palma. Our sample of clusters spans a wide range of metallicity, $-2.28 < [Fe/H] < -0.04$, and horizontal branch morphologies.

- Lick/IDS line indices were measured from these spectra, and a comparison with previous measurements from PSK02 and SRC05 for the common clusters shows good agreement. We construct a homogeneous dataset that contains of 20 Lick line indices for 53 Galactic globular clusters.

- This dataset has been compared with two recent stellar population models from TMK03 and LW05, and it has been found that the LW05 model does a better job of tracing our line indices at low metallicities in the index-index plots than TMK03. The discrepancy of the two models is probably due to their different treatments of horizontal branch stars.

- No strong evidence for line index gradients as a function of the distance from the center of the clusters has been found, even though some clusters in our sample had been previously reported to have radial colour gradients.

Chapter 3

Globular Cluster Systems in Shell Ellipticals

We investigate the properties of the globular cluster systems (GCSs) around six 'shell ellipticals' using archival data from the Advanced Camera for Surveys on HST.[1] The three most luminous galaxies with $M_V < -21.5$ mag show strong evidence of a bimodal colour distribution, whilst the three least luminous galaxies are all consistent with only having a single blue population of clusters. The luminosity functions are well fitted by a Gaussian function in most galaxies, whose turn-over absolute magnitudes appear to be universal. We demonstrate that the ACS data is a considerable improvement on WFPC2 images from HST for identifying populations of globular clusters in nearby elliptical galaxies and discuss the results from this pilot study in the context of current scenarios for the origin of globular cluster sub-populations and shell ellipticals. Finally, we discuss comparison with results from Sikkema et al. (2006) results which use the same ACS dataset, and the application of the

[1]Some/all of the data presented in this paper were obtained from the Multimission Archive at the Space Telescope Science Institute (MAST). STScI is operated by the Association of Universities for Research in Astronomy, Inc., under NASA contract NAS5-26555. Support for MAST for non-HST data is provided by the NASA Office of Space Science via grant NAG5-7584 and by other grants and contracts.

non-linear colour-metallicity relation from Yoon et al. (2006) to our results.

3.1 Background

As a tracer of galaxy formation and evolution, globular clusters(GCs) are widely used for several reasons. Galaxy formation appears to be clearly tied to the formation of GCs. In addition, GCs are composed of millions of stars with the same age and metallicity, which allows us to compare them to simple stellar population models. A number of studies of extragalatic globular clusters have been carried out in the past two decades. One of the most interesting discoveries has been the bimodal colour distribution of extragalatic globular clusters in massive elliptical galaxies. Since Zepf & Ashman (1993) first discovered the bimodal colour distribution in NGC3923, it has been found in many other elliptical galaxies (e.g. Gebhardt & Kissler-Patig 1999; Kundu & Whitmore 2001a; Peng et al. 2006a), and the peak positions of the blue and red subpopulations appear to be universal with V-I $\approx$ 0.95 and V-I $\approx$ 1.18.

The colour of globular clusters is mainly governed by metalicity: the more metal rich a GC, the redder its colour. Another parameter to affect colour is the age of the GC with younger GCs appearing bluer. Therefore, the bimodality implies the presence of two subpopulations differing in metallicity and/or age. As described in §1.3, there are several scenarios that could explain the origin of these subpopulations including the merger of gaseous spiral galaxies, and the metal poor GCs form in the progenitor galaxies (Ashman & Zepf 1992), the *in situ* scenario (Forbes et al. 1997), and the accretion scenario (Côté et al. 1998).

All the above scenarios predict that the blue subpopulation is metal poor and old. However, in the merger scenario the red peak is expected to arise from the metal rich and younger population. In both the *in situ* and accretion models, the red subpopulation is considered metal rich and old. The problem is that although a bimodality is found in many cases, more

complicated colour distributions also exist in giant elliptical galaxies(e.g. a single broad peak or only a blue peak). Unfortunately none of these models succeed in explaining all the properties of extragalatic globular clusters such as colour distribution, specific frequency, radial colour gradient, etc.

Shell features in an elliptical galaxy were first discovered by Malin & Carter (1980). Subsequently, Malin & Carter (1983) cataloged 137 elliptical galaxies possessing shells with a global frequency of ~20%. The shell detecting capability increased with the advent of CCD detectors, finding more than 50% of elliptical galaxies with shells(Seitzer & Schweizer 1992; Forbes & Thomson 1992). There are also several models introduced to account for the origin of shells. N-body simulations successfully reproduced a shell structure by a merger of two unequal mass galaxies (e.g. Quinn 1984; Dupraz & Combes 1986; Hernquist & Quinn 1988, 1989). Alternatively, Thomson & Wright (1990) and Thomson (1991) demonstrate that shells can be produced with weak interactions without merger.

3.2 Observations and Data Reduction

3.2.1 Observation

The Hubble Space Telescope (HST) observations used in this chapter were initially proposed by D. Carter(proposal ID:9399) to study the properties of shells in elliptical galaxies. Their main aim was to investigate the cores of shell galaxies to see if shells exist further in than known previously. Velocity maps from high resolution long-slit and integral-field spectra support this possibility (Balcells & Carter, 1993). With help from the high spatial resolution of the HST, Sikkema et al. (2007) determine the distribution of inner shells, and finally compare with the shell formation model combined ground-based dynamic studies. We used this same observational data to investigate the properties of the GCSs of the shell galaxies. Even though this observation was designed for studying shells themselves, it is deep and

wide enough to detect globular clusters.

The Advanced Camera for Survey (ACS) has three different channels: Wide Field Channel (WFC) for deep, wide field imaging from visible to near-IR, High Resolution Channel (HRC) for high spatial resolution imaging from near-UV to near-IR, and Solar Blind Channel (SBC) for solar blind UV imaging (Pavlovsky et al., 2006). The primary observation was carried out with the WFC along with a parallel observation using the HRC. This parallel observation was automatically set by default. The position of the HRC aperture is controlled by the position and orientation of the WFC so that it is pointing randomly. We did not used the HRC images to find GCs because of the small field of view of $26'' \times 29''$ and since a parallel observation cannot share the same filter set that the primary observation uses. The WFC consists of two 4K×2K CCD chips covering a field of view of $202'' \times 202''$ with a pixel scale of $0.05''/pix$. Figure 3.1 shows the positions and the orientations of the ACS/WFC fields on the Digitalized Sky Survey images demonstrating that the WFC aperture fully covers the sample galaxies.

The filters used are F814W($\approx$ Cousins I) and F606W($\approx$ Johnson V). The typical exposure times are$\sim 900s$ and $\sim 1100s$ in F814W and F606W respectively. The `CR-SPLIT` parameter is set at 2, which divides each exposure into two subexposures without reposition to remove cosmic rays. Dithering was not carried out for these observations, which could have covered the gap between the two chips, and reduced cosmic rays and hot pixels more effectively. In Table 3.1, the basic properties of the sample of six shell elliptical galaxies, and the exposure times are listed.

Table 3.1: Basic Properties of the shell elliptical sample and exposure time

Name	Type	m-M	Ref.	Distance (Mpc)	M_V	M_B	E(B-V)	$logR_e$ (arcsec)	FILTER	Exp Time (s)
(1)	(2)	(3)	(4)	(5)	(6)	(7)	(8)	(9)		
NGC3923	E4	31.80	1	22.91	-22.11	-21.18	0.083	1.78	F814W	978
									F606W	1140
NGC7626	Epec	33.01	2	39.99	-21.93	-20.95	0.072	1.59	F814W	960
									F606W	1140
NGC5982	E3	32.87	2	37.50	-21.70	-20.82	0.018	1.37	F814W	1020
									F606W	1314
NGC2865	E3	32.89	1	37.84	-21.53	-20.71	0.082	1.20	F814W	840
									F606W	1020
NGC1344	E5	31.48	1	19.80	-21.11	-20.24	0.018	1.65	F814W	840
									F606W	1062
NGC474	Sa	32.14	2	26.79	-20.99	-20.17	0.034	1.81	F814W	960
									F606W	1140

Note: Col.(1) Host Galaxy; col.(2) morphological type from NED; col.(3) distance modulus; col.(4) reference for distance modulus: 1.Tonry et al. (2001), 2.Prugniel & Simien (1996); col.(5) distance from col.(3); col.(6) and (7) absolute V and B magnitude using V_T^0 and B_T^0 from NED and col.(3); col.(8) Galactic extinction (Schlegel, Finkbeiner, & Davis, 1998); col.(9) effective radius from NED

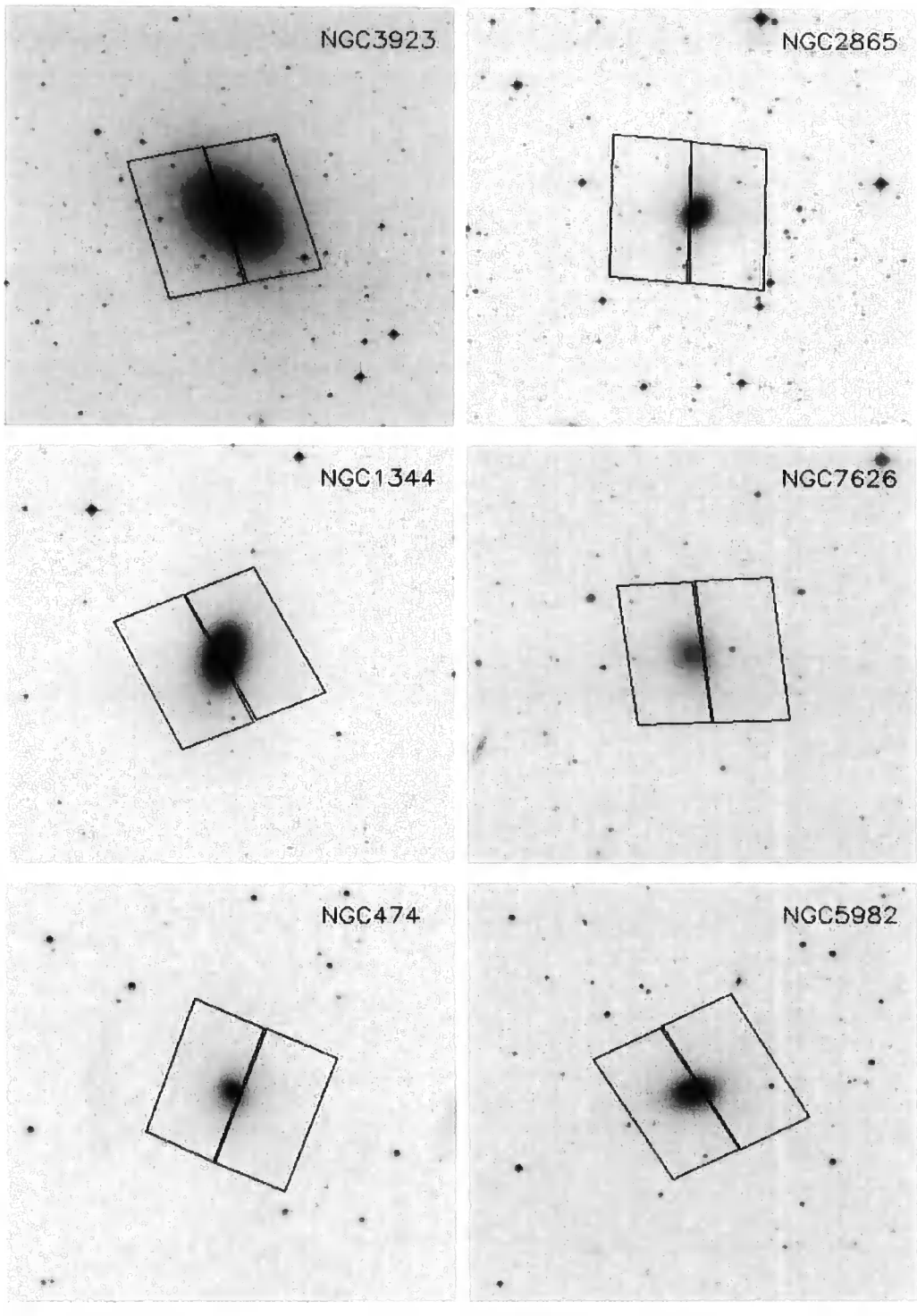

Figure 3.1: The Digitalized Sky Survey images of the shell galaxies overlaid by the ACS/WFC aperture. All the galaxies except NGC3923 are fully covered by ACS/WFC.

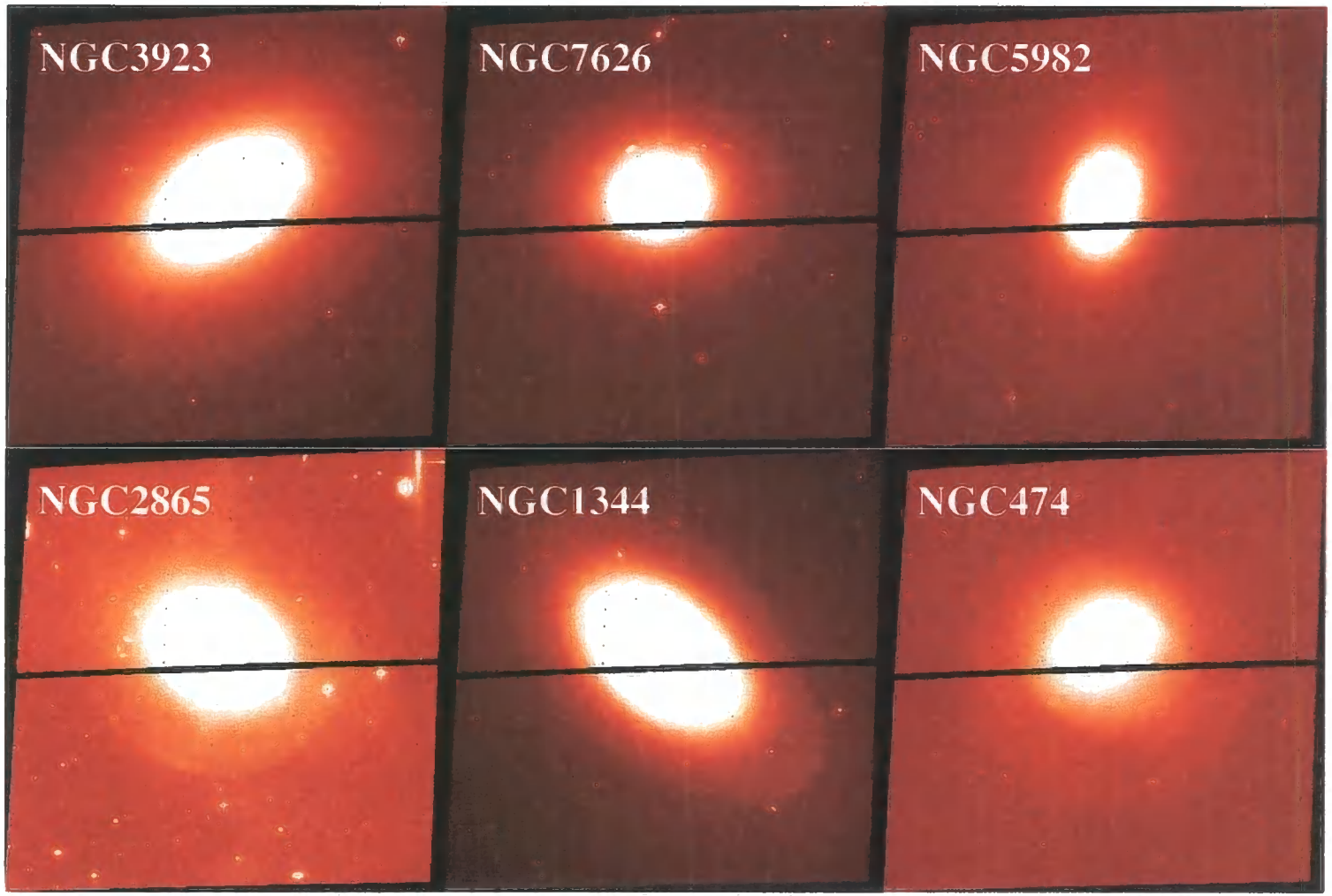

Figure 3.2: The ACS/WFC images of the six shell galaxies with the high spacial resolution in F814W band. Shell features are clearly noticeable in some galaxies. The black bar is the gap between the two WFC CD chips.

3.2.2 Pipeline Processing

For pipeline data processing, we used the standard HST/ACS data pipeline called On The Fly Reprocessing(OTFR). When users request data from the STScI archive, OTFR uses the most up to date reference files such as CCD bias, dark frames, and bad pixel table. The standard pipeline processing contains two separate packages: **CALACS**, and **PyDrizzle**. **CALACS** performs several basic calibrations. First, it subtracts the bias and dark frame from each subexposure image. Then the images divided by `CR-SPLIT` are combined so as to reject cosmic rays. Finally, it is flat fielded to produce a `CRJ` image in the units of electrons. The product from **CALACS** is not suitable for photometry because geometric distortion introduces a variation of pixel area across the field. The reason that the geometric distortion is present on ACS/WPC is because the ACS focal plane is not normal to the optical axis of HST. **PyDrizzle** is the package that corrects this geometric distortion and combines the dithered images. Since our observation does not include dithering, **PyDrizzle** was run just for correcting the distortion, and then creating `DRZ` images in the units of electrons/sec. We therefore retrieved `DRZ` images from HST archive, and used them for detection and photometry of GCs. Figure 3.2 shows the calibrated `DRZ` images of the six shell ellipticals in the F814W band.

3.2.3 Photometry

We used the *SExtractor* (Bertin & Arnouts, 1996) package for detecting GC candidates. *SExtractor* is an object detection and photometry package which works by the sequence of detecting objects above a certain threshold, deblending objects, measuring photometric and morphological parameters, and classifying between point and extended sources using a neural network. The detecting parameters were set to 5 pixels for the minimum area of an image above threshold and a minimum 3 σ detection above the background computed in 32 $\times$ 32 pixel grid. We did not subtract the galaxy light independently since it is hard

to model analytically because of the shells. Once the GC candidates were classified based on *SExtractor* output parameters as described in §3.2.4, their flux was measured using the PHOT routine in the IRAF package with 3 and 10 pixel aperture radii. The background levels were taken to be the median value between 10 and 20 pixels radii. The reason for using the PHOT routine for aperture photometry is because magnitudes produced by *SExtractor* are not suited for photometry that requires a high accuracy.

The half-light radius of a typical GC, taken to be the median value of the half-light radius for the Galactic GCs (Harris, 1996) [2] , is $r_h \approx 5pc$. If this half-light radius is converted to the half-light diameter at the given distance, we find an angular half-light diameter in the range $0.05'' \lesssim 2r_h \lesssim 0.10''$. Considering the FWHM of the ACS/WFC PSF is $\approx 0.1''$, GCs at the distance of our galaxies, $20Mpc \lesssim d \lesssim 40Mpc$, are marginally resolved by HST/ACS. Thus applying the aperture correction derived from a stellar PSF to extended objects like GCs underestimates their total magnitude. In addition, the mean size of GCs shows some scatter between galaxies, since in our sample there is no trend for the median size to be smaller in the more distant galaxies (see Figure 3.14 in §3.3.3).

An aperture correction was therefore determined from the offset between 3 and 10 pixel radius aperture photometry for several bright GCs in each frame. An additional correction from 10 pixel radius aperture to infinite aperture was adopted from the ACS calibration paper by Sirianni et al. (2005). The mean total aperture correction from 3 pixel radius to infinite radius for each galaxy and each filter is listed in Table 3.2; this was applied to all the GC candidates in a given galaxy. The aperture corrections for the stellar PSF in Table 3.2 were calculated from a model PSF produced by the *Tiny Tim* package (Krist & Hook 2004) for each band. Figure 3.3 shows the aperture corrections of the GCs against the host galaxy distances in the two filters. The aperture corrections do not show a strong correlation with the distances. The differences between the aperture correction in the two filters for NGC2865

[2]Available at: http://physun.physics.mcmaster.ca/Globular.html

Table 3.2: Aperture correction magnitudes from 3 pixel radius to infinite aperture and 50% completeness

	Δ F606W	Δ F814W	F606W	F814W
Stellar PSF	0.248	0.292		
NGC3923 GCs	0.321	0.367	25.8	25.8
NGC2865 GCs	0.364	0.453	26.1	26.2
NGC1344 GCs	0.385	0.436	26.1	26.2
NGC7626 GCs	0.338	0.474	26.2	26.3
NGC474 GCs	0.318	0.370	26.1	26.3
NGC5982 GCs	0.294	0.349	26.5	26.3

and NGC7626 are noticeably larger than those for the stellar PSF and other galaxies. We have investigated instrumental effects by checking the HST/ACS observational log files. For NGC7626, the guide star for this observation is much fainter than those for other galaxies; its magnitude is 13.2 mag, whereas a typical magnitude of guide stars for other galaxies is ∼11 mag. Consequently, the root mean squares of the jitter about V2 and V3 axis for NGC7626 are 4.7 mili-arcsec and 6.7 mili-arcsec respectively. Typical root mean squares of the jitter for other galaxies are 2.6 mili-arcsec and 4.0 mili-arcsec about V2 and V3 axis respectively. This could account for the unusual aperture correction behaviour for this galaxy.

For NGC2865, there is no difference compared to other galaxies in terms of a guide star magnitude and jitter. The reason for the large difference in the aperture corrections between the two filters in NGC2865 is therefore still not understood. However, we have verified that our way to treat the aperture corrections effects is sensible even accounting for instrumental effecs. These differences result in the main discrepancy between the conclusion by Sikkema et al. (2006) and ours as discussed in §3.4.1.

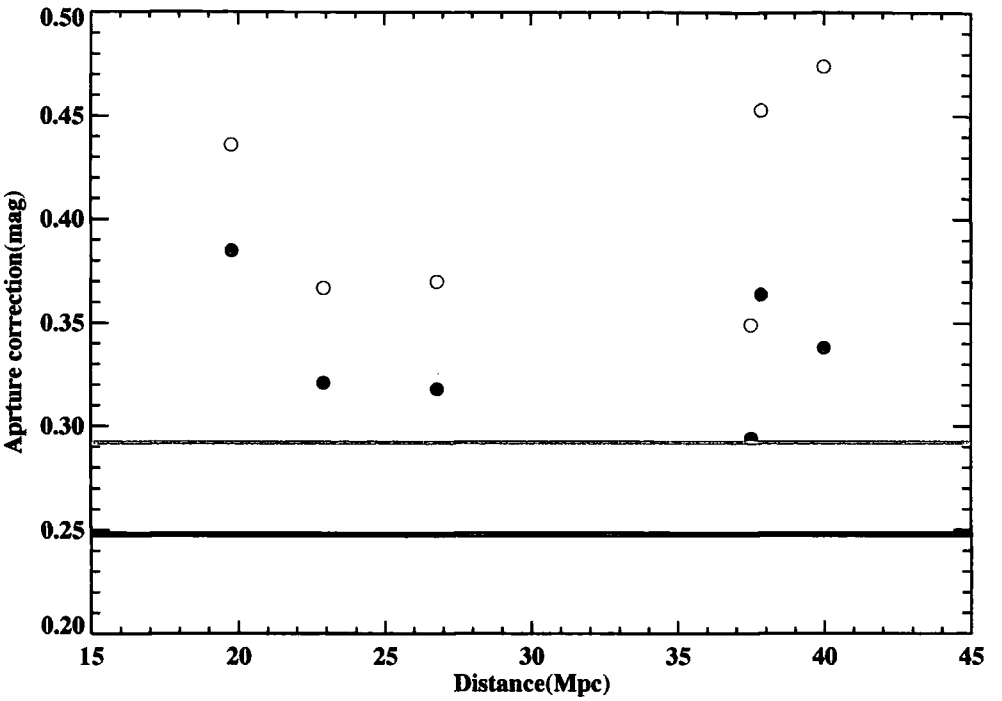

Figure 3.3: Aperture corrections against host galaxy distances. The filled circles represent F606W filter, while the open F814W filter. The thick black and grey lines are the aperture corrections of the stellar PSFs of F606W and F814W, respectively. The difference of aperture correction between the two filters remains stable, whereas the aperture corrections themselves vary between galaxies.

Another photometric correction that should be considered is a photometric loss caused by the Charge Transfer Efficiency(CTE) degradation due to cosmic ray damage, which depends on a function of a CCD position, flux, background, time and aperture size. Since the source and background(host galaxy) flux is high and these observations were carried out at an early epoch, from Aug. 2002 to Jan. 2003, the photometric loss is only a few $0^m.01$ (Riess & Mack, 2004). Even if it is not negligible, it does not affect the colour of the GCs because the CTE does not depend on which filter is used. The completeness tests were determined from Monte-Carlo experiments using artificial GC images added to the reduced frames. Figure 3.4 shows the completeness level along with magnitude in the F606W band, and the 50% completeness limit for each galaxy is listed in Table 3.2. This procedure is discussed in more details in Chapter 4.

For correcting foreground reddening we adopted the extinction map of Schlegel, Finkbeiner, & Davis (1998) and the extinction law of Sirianni et al. (2005): $A_{F606W} = 2.764E(B-V)$ and $A_{F814W} = 1.803E(B-V)$. The internal reddening for the galaxies was ignored, since as can be seen from Figure 3.2, none of the galaxies show evidence of strong dust lanes. Although Sikkema et al. (2007) found some evidence of dust features in the very central regions of the sample galaxies, only a few of the GCs detected are located in that region. The aperture and extinction corrected magnitudes were converted to Johnson-Cousins V and I magnitudes using the equations:

$$V = \begin{cases} F606W + 26.394 + 0.153(V-I) + 0.096(V-I)^2 & ,(V-I) < 0.4, \\ F606W + 26.331 + 0.340(V-I) - 0.038(V-I)^2 & ,(V-I) > 0.4 \end{cases} \tag{3.1}$$

$$I = \begin{cases} F814W + 25.489 + 0.041(V-I) - 0.093(V-I)^2 & ,(V-I) < 0.1, \\ F814W + 25.496 - 0.014(V-I) + 0.015(V-I)^2 & ,(V-I) > 0.1 \end{cases} \tag{3.2}$$

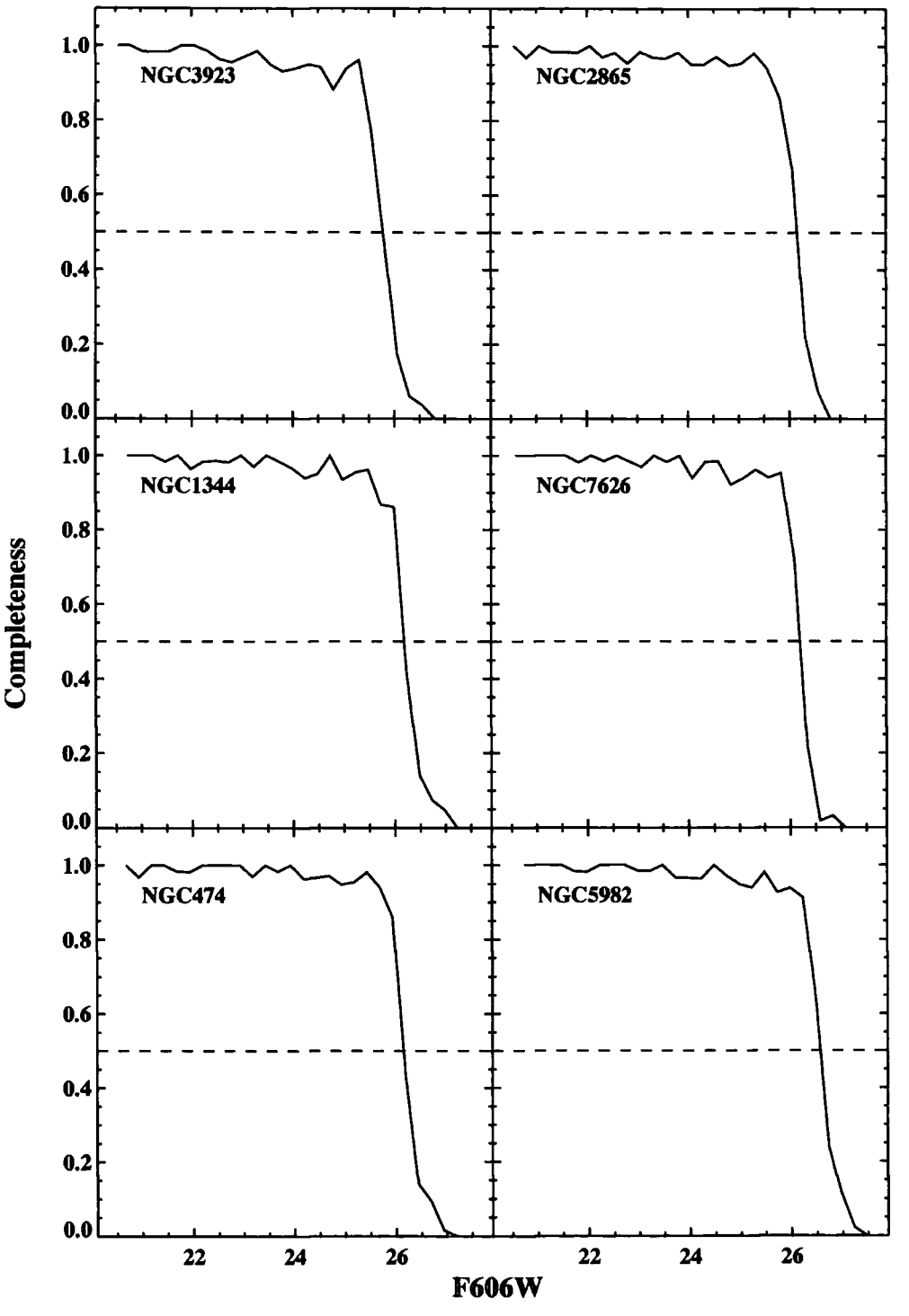

Figure 3.4: Completeness test on the six sample galaxies in F606W band. The dashed lines are guide lines for 50% completeness, which is listed in Table 3.2.

from the transformation table of Sirianni et al. (2005), which allows us to compare our results with previous studies directly. Hereafter, all the magnitudes and colours are presented in the Johnson-Cousins V and I magnitude system.

3.2.4 Classification of globular clusters

GCs were selected based on their morphology, magnitude and colour. The *SExtractor* output parameters of `ELONGATION` and `CLASS_STAR` were used as the main criteria. The `ELONGATION` parameter is defined as A/B, where A and B are the image semi-major and semi-minor axis lengths, respectively. `CLASS_STAR` is a star/galaxy classifier parameter based on the neural network which returns `CLASS_STAR`=1 for point stellar objects, and `CLASS_STAR`=0 for very extended galaxies. Among the detected objects, those with `ELONGATION` less than 2 and `CLASS_STAR` greater than 0.9 were classified as GC candidates. In addition, the GC luminosity function(GCLF) in the Milky Way and M31 is fit by a Gaussian distribution with a turn-over magnitude of $M_{V,TO} = -7.4 \pm 0.2$ and the standard deviation of $\sigma = 1.2 \pm 0.1$ (Beers et al. 1990, Bird & Beers 1993). This distribution appears to be quite universal for elliptical galaxies (e.g. Jordán et al. 2006), therefore objects brighter than $M_{V,TO} - 3\sigma$ were discarded to minimize the contamination by foreground stars. There is also a constraint applied on the colour of the GCs. Based on the redening corrected colours of the Galactic GCs from Harris (1996), we set the allowed colour range to be $0.5 <$ V-I < 1.5. Figure 3.5 shows the colour magnitude diagram of the GCs in the six shell ellipticals, and the magnitude and colour constraints.

3.2.5 Foreground and background contamination

Two main sources of contamination are present in our GCS candidates: foreground stars and background galaxies - particularly those which are dominated by a compact bulge component. We estimated each contamination source statistically. For the former, the luminosity

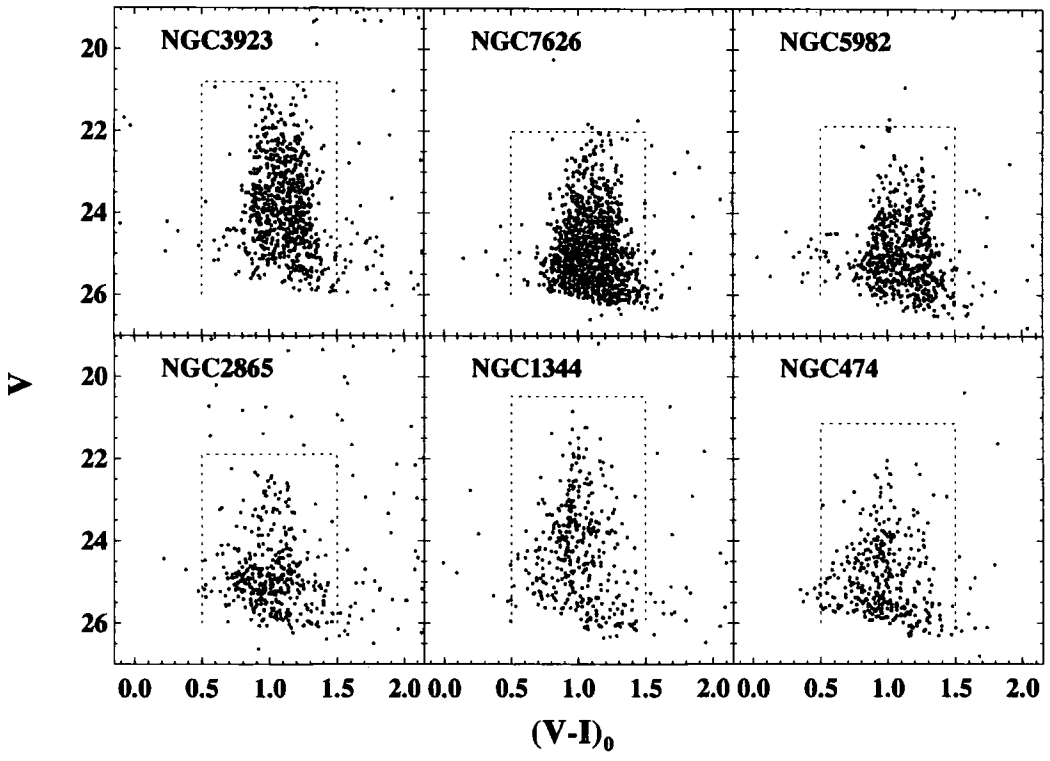

Figure 3.5: The colour magnitude diagram of globular cluster candidates around the six shell ellipticals. The vertical dotted line represents the adopted colour cut, 0.5 < V-I < 1.5. The horizontal line does the magnitude cut, $M_{V,TO} - 3\sigma$, where $M_{V,TO}$ is the absolute V magnitude which corresponds to the peak of the Galactic GC luminosity function.

function and the colour distribution of foreground Galactic stars in the direction of the galaxies were obtained from the model [3] of the Milky Way by Robin et al. (2003). For the latter, the ACS images from the GOODS survey (Giavalisco et al., 2004) were used as representative high latitude blank fields. We ran *SExtractor* on one of the Chandra Deep Field South(CDF-S) sections with the same input parameters as used for detecting GCs. The same classification criteria were then applied to the output. After subtracting the expected number of foreground stars, we obtained the distribution of background galaxies. These two contamination distributions were used to correct the GC luminosity functions and the colour distributions statistically. Note that the total level of contamination is always less than 10% of the number of GC candidates.

3.2.6 Comparison with previous WFPC2 observations

Three of the sample galaxies, NGC7626, NGC5982, and NGC474, have been observed before with HST/WFPC2, and their GCs were analyzed by Kundu & Whitmore (2001a) and Kundu & Whitmore (2001b) (hereafter KW01). Figure 3.6 shows the positions of the GCs from the two different observations. After correcting offsets, which are calculated by the median value of differences in RA and DEC, 135, 83, and 27 common GCs are found within 1″radius in NGC7626, NGC5982, and NGC474 respectively. To test the accuracy of our photometry, we directly compared the magnitude of the commonly detected GCs. Figures 3.7, 3.8, and 3.9 show the comparison of magnitude and colour in NGC474, NGC5982, and NGC7626 respectively. Our measurements of magnitude appear to be systematically 0.2∼0.3mag lower than KW01's measurements in both the filters. This is possibly due to their overestimation of the sky background level. KW01 used the median value between 5 and 7 pixels as a sky background, where a considerable amount of GC light may still exist. Another possibility is due to the smaller aperture correction. KW01 derived an aperture correction from a

[3]Available at: http://bison.obs-besancon.fr/modele/

linear fit to the aperture corrections against distance for a subsample of galaxies with a minimum correction set by the aperture correction of the stellar PSF. However, as can be seen in Figure 3.3, our aperture corrections appear to be independent of distance and even those in the most distant galaxies have greater aperture correction than the stellar PSF. For instance, the most distant galaxy, NGC7626, has the minimum aperture correction (stellar PSF) in KW01, whereas ours is much larger than the PSF value (see Table 3.2). Finally, the extinction map was adopted from different sources for some galaxies. For example, our extinction $A_V = 0.24$ in NGC7626 comes from Schlegel, Finkbeiner, & Davis (1998), whereas KW01 adopted a somewhat obsolete value, $A_V = 0.12$, from Burstein et al. (1984). This non-negligible difference, 0.12mag, seems to contribute to the magnitude offset to some degree.

In addition, there is also discrepancy in colour with a systematic dependence; KW01's blue GCs appear to be bluer, and the red GCs to be redder than ours. This trend cannot be explained by any of the three possibilities above, because these make the colors shifted not tilted. One possible explanation would be because of some uncertainties in the ACS or WFPC2 calibration. However, the colour distributions from both the studies do not show a large deviation as shown in the bottom-right panel of Figure 3.9, although KW01's colours are slightly more spread than ours.

3.3 Data Analysis

3.3.1 Colour distributions

The V-I colour distributions of the globular cluster systems (GCSs) in the six shell galaxies are shown in Figure 3.10 ordered by host galaxy absolute magnitude. We found that colour selection resulted in less blue objects being detected in the faint magnitude bins. In order to avoid any bias by the colour selection, and to minimize the effects of photometric

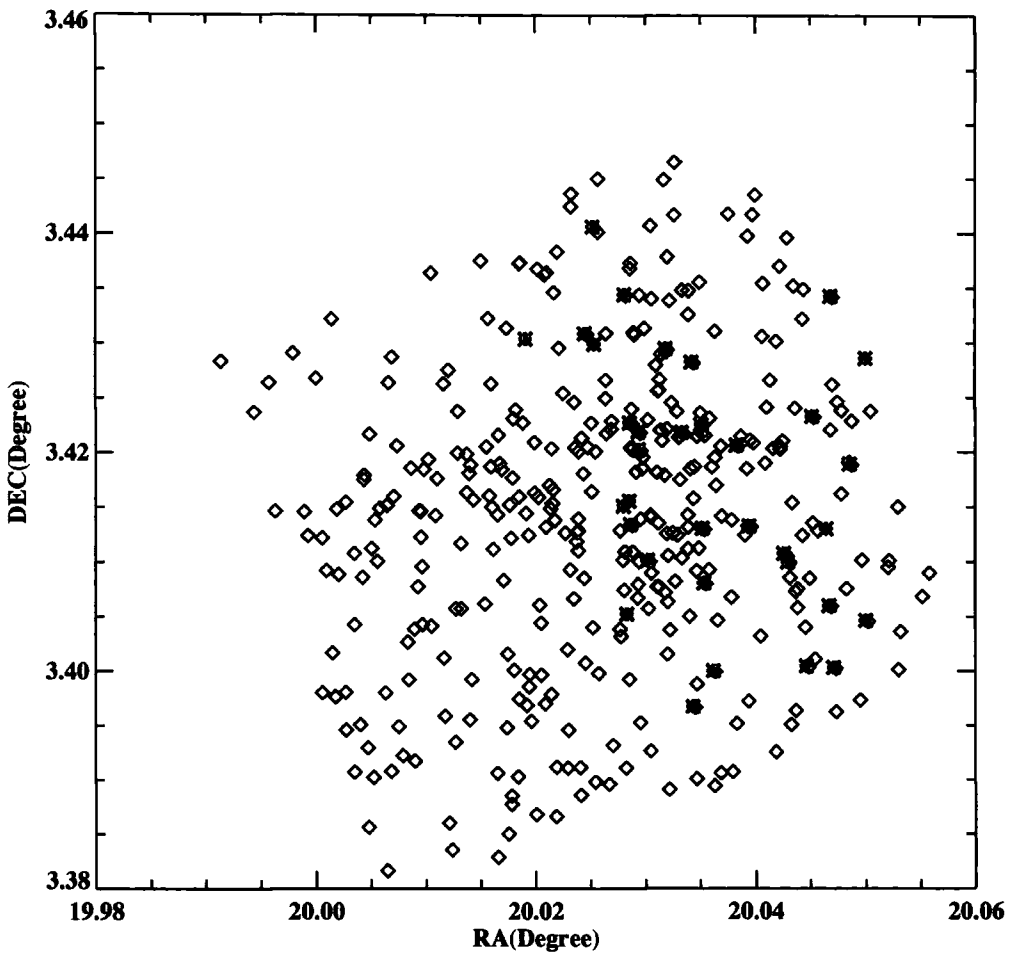

Figure 3.6: Matching the globular clusters of NGC474 with Kundu & Whitmore (2001b). The squares are the GCs detected by this work, while the asterisks by Kundu & Whitmore (2001b). There are 27 GCs matched within 1″radius after correcting slight offsets.

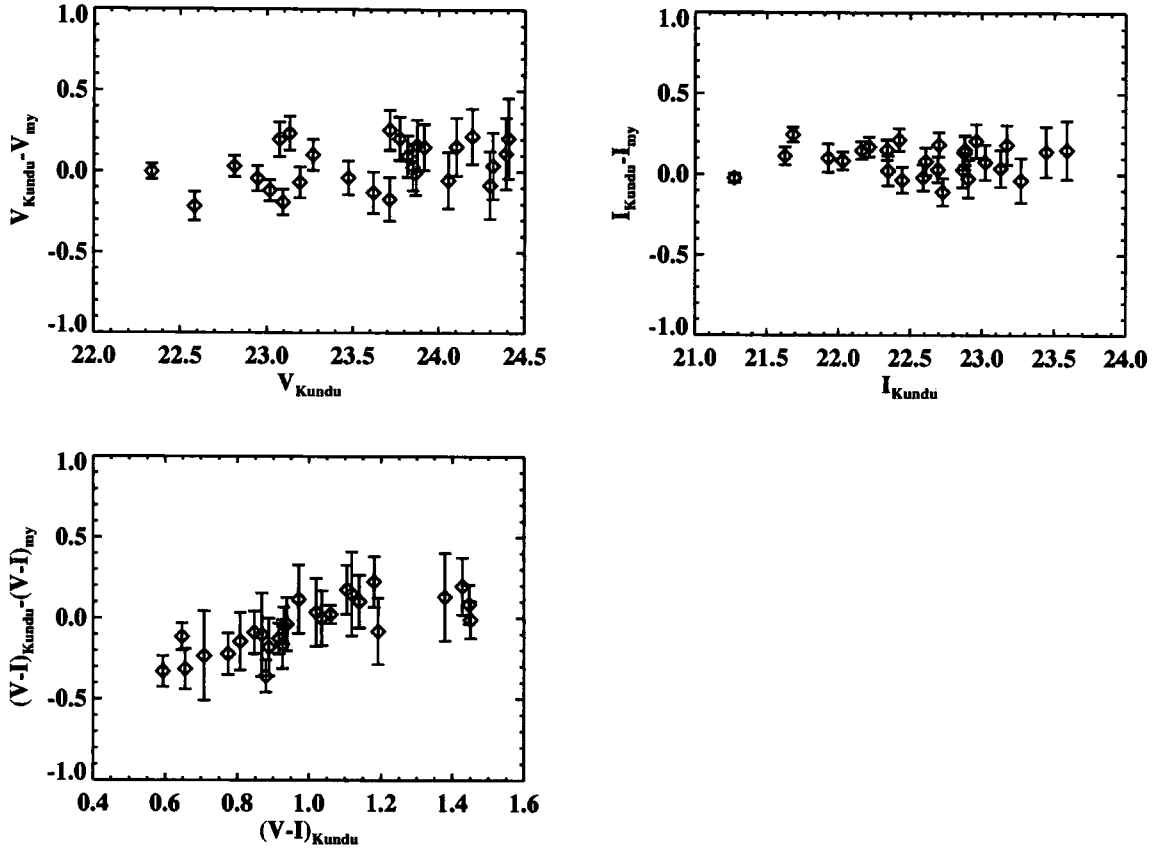

Figure 3.7: Comparison of NGC474 GC photometry with Kundu & Whitmore (2001b).

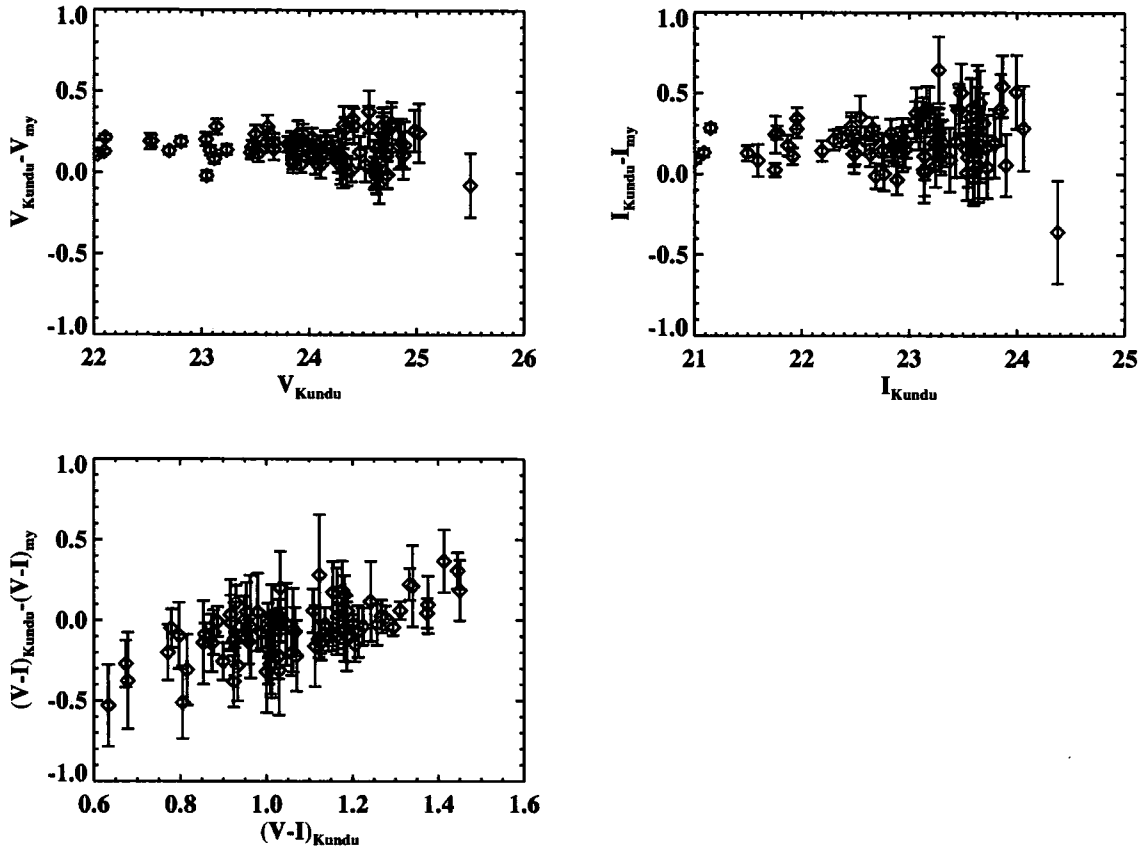

Figure 3.8: Comparison of NGC5982 GC photometry with Kundu & Whitmore (2001a).

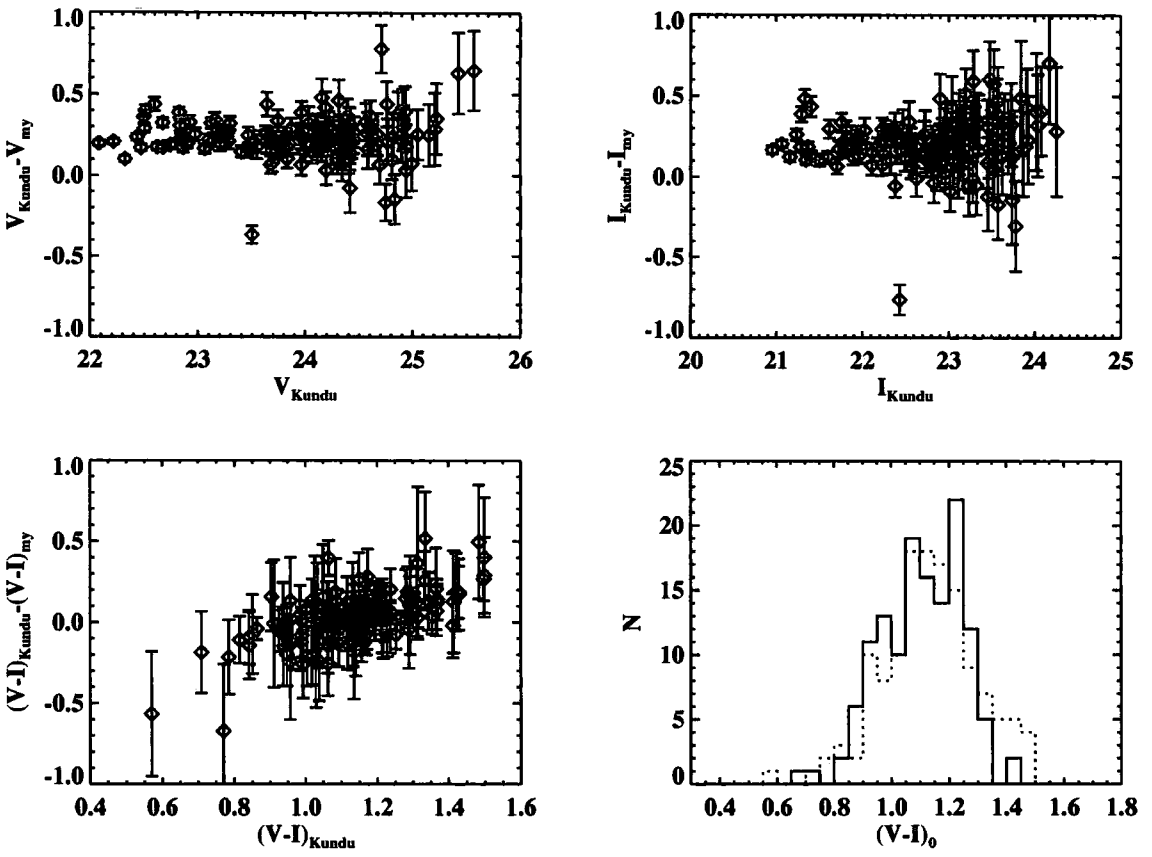

Figure 3.9: Comparison of NGC7626 GC photometry with Kundu & Whitmore (2001a). In bottom-right panel, the colour distributions of the commonly detected GCs are plotted. The solid histogram is from this work, whereas the dotted histogram is from KW01.

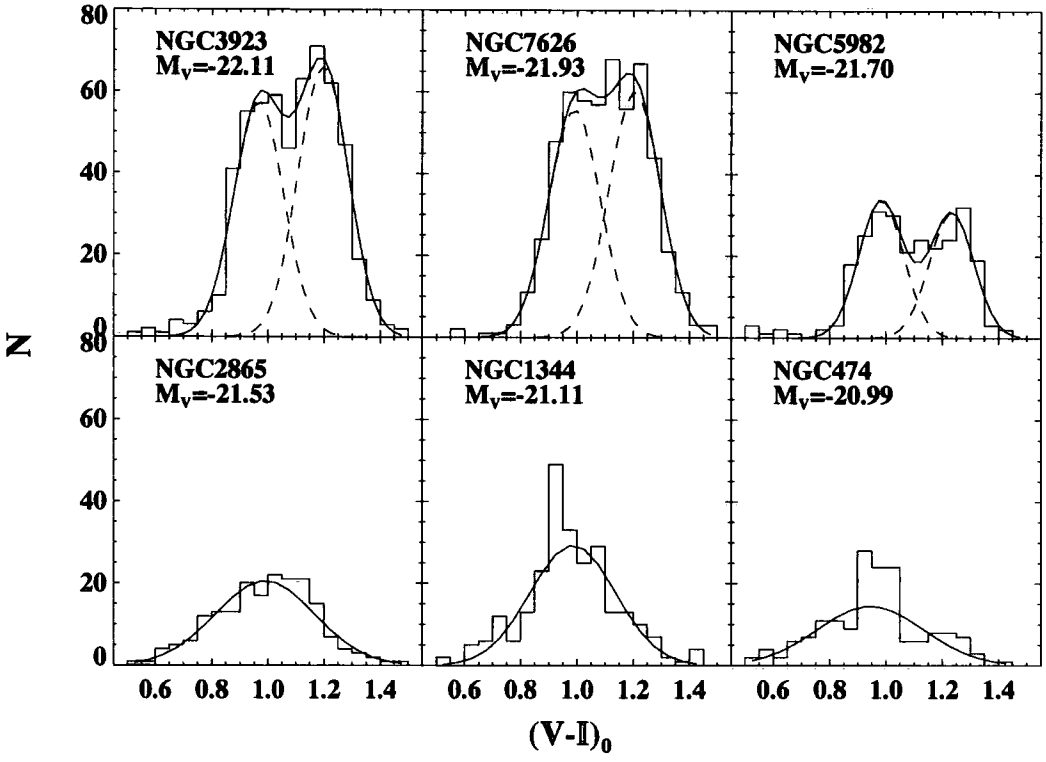

Figure 3.10: The colour distribution. The dashed lines represent Gaussian fits to the subpopulations based on KMM test output. The solid line is the sum of subpopulations in the upper panels, and a single Gaussian function to fit all GC candidates in the lower panels.

errors (Malmquist effect), a faint magnitude limit of $V = 25mag$ was applied to the colour distribution diagrams.

At first glance, it can be seen that the three most luminous galaxies seem to have a bimodal GC colour distribution, while the three least luminous galaxies display a unimodality. We used the KMM test (Ashman, Bird, & Zepf, 1994) to confirm whether the colour distributions have bimodality or unimodality statistically. The KMM test assumes that each subpopulation has a Gaussian distribution with identical width, and the KMM test outputs are summarized in Table 3.3. The KMM test reveals that the three most luminous shell galaxies(NGC3923, NGC7626, and NGC5982) display bimodality with more than 95%

Table 3.3: Properties of Globular cluster systems

	$N_{GC,det}$	Blue Peak	Red Peak	Bimodality	$< (V-I)_0 >$	$< [Fe/H] >$
	(1)	(2)	(3)	(4)	(5)	(6)
NGC3923	662	0.97	1.20	YES	1.08	-0.82
NGC7626	1110	0.99	1.21	YES	1.10	-0.76
NGC5982	595	0.98	1.23	YES	1.09	-0.80
NGC2865	364	0.99		NO	0.99	-1.20
NGC1344	357	0.99		NO	0.98	-1.27
NGC474	339	0.94		NO	0.96	-1.35

Note: Col(1): the number of GC detected, col(2) and (3): blue and red colour peaks produced by KMM test, or the best fitted peak position of a single Gaussian for the galaxies whose GC colour distribution is unimodal, col(4): likelihood of bimodality based on p-value output by KMM test, col(5): mean colour of GC candidates, col(6): mean metallicity of GC candidates.

confidence. On the other hand, in the three least luminous galaxies, the GCS colour distributions are more likely to be a unimodal. For these galaxies we therefore fit a single Gaussian function. It is also noticeable that the single peak in the less luminous galaxies is consistent in colour with the blue peak of the bimodality in the luminous galaxies. This implies that the less luminous galaxies significantly lack a red subpopulation.

A plot of the average colour of the GCS vs. the absolute magnitude of the host galaxy (Figure 3.11.) shows this trend more obviously. The metallicity of GCs is one of the driving parameters of their colour. Assuming an old age, colour can be converted to metallicity,

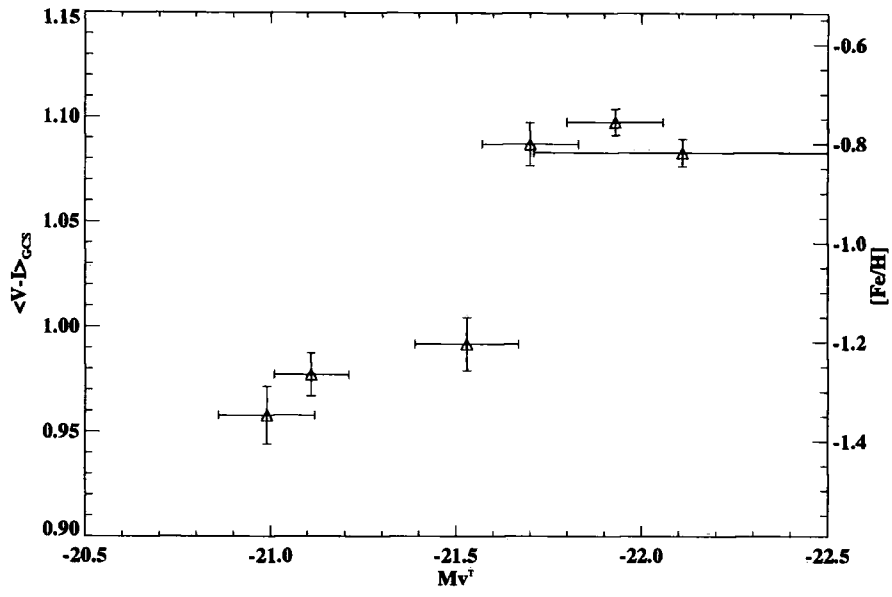

Figure 3.11: Average colour of GCS vs. host galaxy absolute magnitude. The mean colour of GCS is strongly correlated with the host galaxy absolute luminosity: the colour of GCS gets redder (the metallicity of GCS gets richer) increasing with the galaxy mass.

$[Fe/H]$, using the colour-metallicity relation:

$$[Fe/H] = (4.22 \pm 0.39)(V - I)_0 + (-5.39 \pm 0.35),$$

based on the Galactic GCs (Barmby et al., 2000). This metallicity scale is shown in the right axis of the diagram in Figure 3.11.

When comparing our results with previous studies on the same host galaxies, our results turn out to be deeper, and to show some interesting effects . Zepf et al. (1995) detected 145 globular clusters in NGC3923 and derived an average metallicity of $[Fe/H] = -0.56 \pm 0.14$ from their Washington $(C-T_1)_0$ colour. However, we detect more than four times the number GC candidates, and our GCS is more metal poor than theirs (see Table 3.3). More recently, Kundu & Whitmore (2001a) and Kundu & Whitmore (2001b) studied the properties of globular clusters in 28 elliptical and 29 S0 galaxies using archival WFPC2 images. There are

the three common galaxies: NGC7626, NGC5982, and NGC474 with our sample. While they detected 152, 89, and 34 globular cluster candidates in NGC7626, NGC5982, and NGC474 respectively, we find many more GC candidates due to the greater depth of the ACS images (see Table 3.3 and Figure 3.6). Moreover, while these authors found no strong evidence for bimodality in NGC7626 and NGC5982, our data show a clear bimodality. In addition, our peak positions agree well with the peaks from Kundu & Whitmore (2001a) as shown in Figure 3.12(a). Even allowing for the fact that our ACS data have almost double the exposure times in the F814W band, the ACS images show a better performance in detecting GCs than WFPC2. This is probably because the ACS has a slightly wider field of view, a better spatial resolution, and detector sensitivity.

An extensive study on GC colour distributions was carried out by Peng et al. (2006a) as a part of the ACS Virgo Cluster Survey (Côté et al., 2004). Since these authors used F475W($\approx$ SDSS g) and F850LP($\approx$ SDSS z) filters, and there is no reliable colour transformation between V-I and g-z empirically or theoretically, we compare our results with Peng et al. (2006a) in terms of metallicity [Fe/H]. Figure 3.12(b) shows that the peak positions of our samples are consistent with those from Peng et al. (2006a). Even though the source of the colour-metallicity relation we used is different from Peng et al. (2006a), and our colour-metallicity relation is linear while the g-z relation is non-linear, differences are within the calibration uncertainty of both colour-metallicity relations in the metallicity range between $-1.4 \lesssim [Fe/H] \lesssim -0.2$.

3.3.2 Luminosity functions

As mentioned in §3.2.4, the globular cluster luminosity function(GCLF) is well fitted by a Gaussian function, whose peak is known as the turnover luminosity of the GCLF. Our V band GCLF is corrected for foreground and background contamination, and then it is fitted by a Gaussian function down to the 50% completeness limits (Table 3.2). The ACS observations

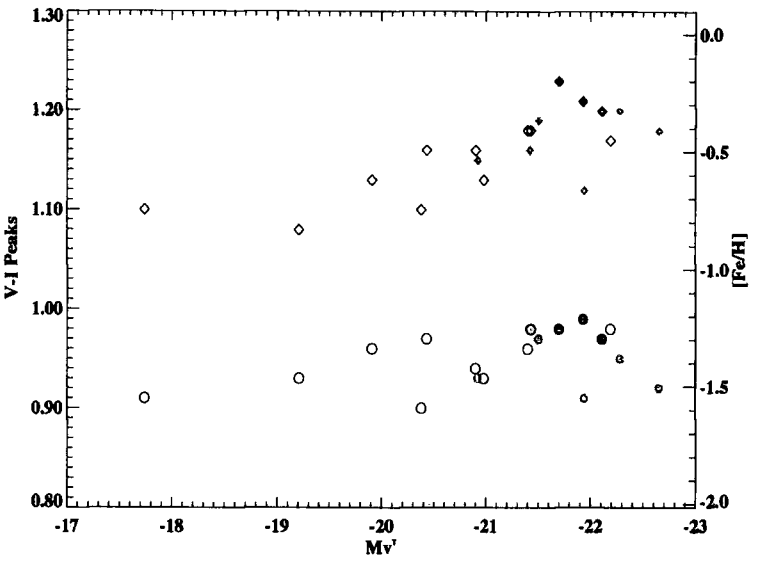

(a)

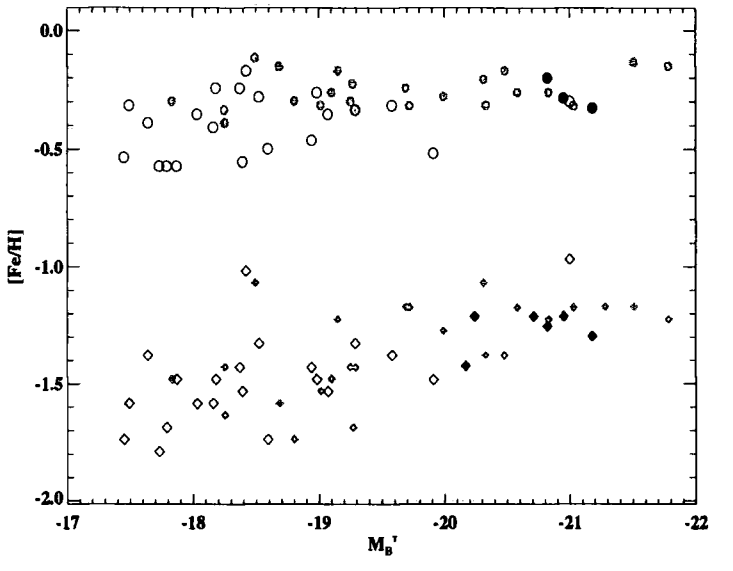

(b)

Figure 3.12: Metal-poor and metal-rich peak position vs. host galaxy luminosity M_B. The circle and diamond symbols represent metal-rich and metal-poor peak respectively. The open symbols are likely bimodal peaks, the shaded symbols are strong bimodal peaks from Kundu & Whitmore (2001a) in (a), and from Peng et al. (2006a) in (b), and the filled ones are our results.

Table 3.4: Fitted parameters of GCLF and turn-over absolute magnitudes

Host Galaxy	m_{TO,m_M}	$m_{V,TO}$	σ_V	$M_{V,TO}$
	(1)	(2)	(3)	(4)
NGC3923	24.40	24.08 ± 0.04	1.18 ± 0.03	-7.7
NGC7626	25.61	25.71 ± 0.09	1.28 ± 0.06	-7.3
NGC5982	25.47	25.34 ± 0.05	0.98 ± 0.04	-7.5
NGC2865	25.49	25.94 ± 0.64	1.39 ± 0.36	-7.0
NGC1344	24.08	24.45 ± 0.07	1.26 ± 0.07	-7.0
NGC474	24.74	26.14 ± 0.32	1.14 ± 0.16	-6.0

Note: Col(1): turnover V magnitude derived from distance modulus and assuming $M_{V,TO}$=-7.4, col(2): turnover V magnitude fitting GCLF, col(3):σ of GCLF, col(4): absolute magnitude in turn-over

are deep enough to detect the turnover magnitude in most galaxies. Figure 3.13 shows the GCLF with fitted Gaussian function for our sample; the fitted Gaussian parameters are listed in Table 3.4. It is found that the turnover magnitudes agree well with the ones expected from the distance modulus assuming a Galactic GCLF except for NGC 474, in which excess of GCs at faint magnitudes causes the disagreement. The standard deviations of the GCLFs are also consistent with a fixed $\sigma = 1.2 \pm 0.1$. Our results support the view that the GCLF parameters are similar across a wide range of morphologies and luminosities so that it can be used as a distance indicator. The average of the absolute turn-over magnitudes of the GCSs in our sample except NGC474 is $< M_{V,TO} >= -7.3$, which is consistent with the turn-over magnitude in the MW and M31(Beers et al. 1990, Bird & Beers 1993).

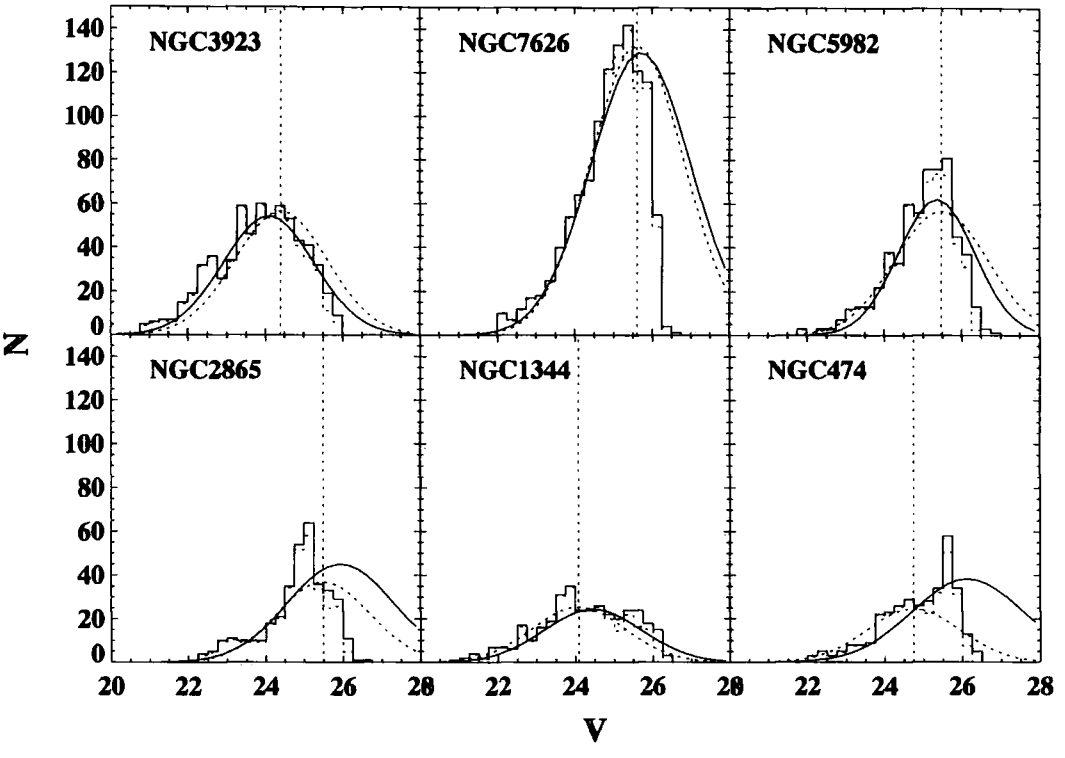

Figure 3.13: Globular cluster luminosity functions: The solid histogram is the observed GCLF, the dashed histogram is a contamination corrected GCLF, the solid line is a fitted Gaussian function, the dashed line is a fitted Gaussian function with a fixed turnover magnitude and standard deviation (see text), and the dashed vertical line is the expected turnover magnitude based on the distance modulus in Table 3.1

3.3.3 The size of globular clusters

We measured the sizes of the GCs using the **ishape** software developed by Larsen (1999). **ishape** fits a King profile(King, 1962) convolved by the ACS PSF function for each band. We choose a concentration parameter of c=30[4] since the average c value of the Galactic GCs is $\log r_t/r_c = 1.5 (r_t/r_c \approx 30)$. The output of **ishape** is expressed as a FWHM[5] in pixels. Only the brighter GC candidates gave consistent results. We take the median value of the size as the best estimator of the size of the whole GC population, because there was no strong correlation found between the GC brightness and size (e.g. Jordán et al. 2005) . We also checked whether or not the median size of the GCs can be used as a distance indicator. As shown in Figure 3.14, there is no trend of median size against distance for our sample. This is not surprising since the plot of the FWHM (Figure 3.14) and the aperture correction (Figure 3.3) against distance resemble each other. The bigger GCs have a more extended light profile so that the GC aperture correction also increases. We generated the King profile with several different core radii to investigate the expected trend, but the median sizes of the GCs in the host galaxies just scatter between 1pc to 3pc. In particular the three most distant galaxies at around 40Mpc have a range of >2 in expected median size.

There are several sources of uncertainty in determining the exact size of GCs. The analytic King profile fitted has two free parameters: concentration parameter and core radius. Since we fixed the concentration parameter, the size returned by **ishape** still has an intrinsic uncertainty. The uncertainties of the ACS PSF and the fitting algorithm could also prevent us from determining the size of the GC accurately. However, as seen in Figure 3.14, there is no systematic difference between the two bands. We conclude instrumental effects are more dominant than distance effects. Fundamentally, in order to use GC sizes as a distance

[4]Concentration parameter defined as $c = r_t/r_c$, where r_t is a tidal radius and r_c is a core radius. Conventionally it is defined as $c = \log r_t/r_c$ by King (1962).

[5]Core radius, half-light radius, and FWHM are used to express the size of a GC. They can be converted to each other for a given analytic profile model.

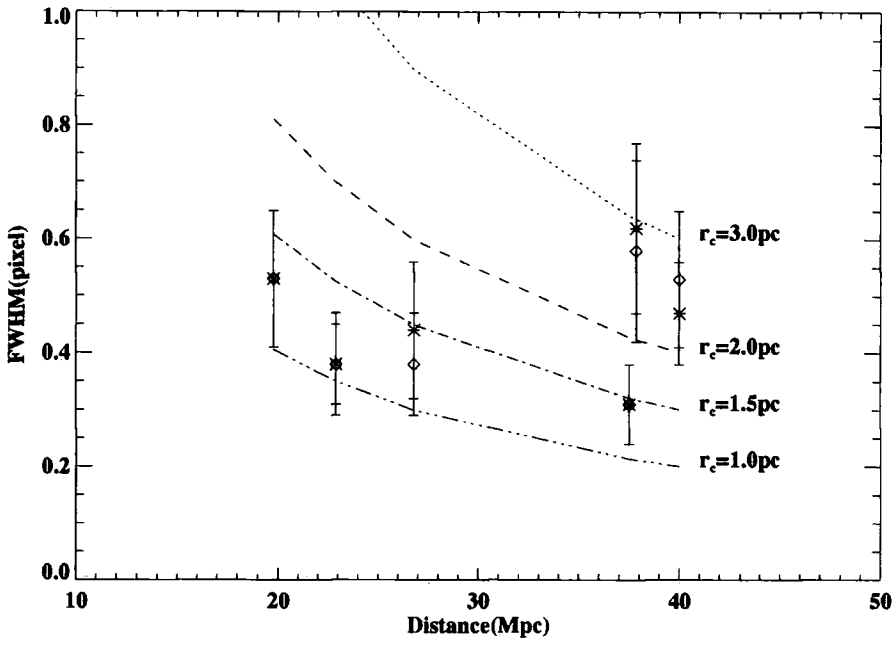

Figure 3.14: The size of GC, FWHM, returned by `ishape`. The asterisk is from F606W, the diamond from F814W. The four lines are the analytic King models with c=30 for the four different core radius.

indicator, a standard value should be defined first, for example from Galactic GCs. However, the size of Galactic GCs spans a wide range of $0.04pc \lesssim r_c \lesssim 30pc$ with an asymmetric distribution. The mean value varies significantly with how this is sampled. Therefore, the median size of GCs is not as a good distance indicator as other methods such as SBF (Tonry et al., 1997) , or the turnover magnitude of the GCLF (Richtler, 2003).

3.4 Discussion

3.4.1 Comparison with Sikkema et al. (2006)

Sikkema et al. (2006; hereafter SIK06) have also investigated the properties of the GCs in the same sample of shell ellipticals using the same HST/ACS data set. However, SIK06

used different reduction methods which have produced somewhat different results from ours. The initial reduction procedures were almost identical and used a default set of parameters for the ACS calibration pipeline. SIK06 removed comic rays by running the LA_COSMIC software (van Dokkum, 2001), which is a robust cosmic ray rejection algorithm based on Laplacian edge detection, on the final images. The biggest difference in the procedure for detecting GCs is how to treat the host galaxy background light explicitly. In this work, we did not subtract the galaxy light explicitly, letting SExtractor remove the galaxy light using a filtering scheme before GC detection. SIK06 used the ellipse fitting task GALPHOT to fit the underlying spheroid. There are minor differences in the SExtractor parameters used for detecting and selecting GCs (e.g. BACK_FILTERSIZE, BACK_SIZE, ELONGATION). Our colour selection range ($0.5 < V - I < 1.5$) is also slightly narrower than SIK06's ($0.55 < V - I < 1.45$). While we applied a magnitude cut at the bright end, SIK06 did not.

There are several differences in the photometric procedures adopted. Even though both analyses used aperture photometry, we used an initial aperture diameter of 6 pixels, but SIK06 adopt 8 pixels. Aperture corrections were also calculated differently. SIK06 added artificial objects with a typical *stellar* point spread function to a residual image and calculated the offset between input and output magnitudes. This aperture correction, 0.26mag, was then applied to all of the twelve images. The reason this procedure was adopted is that SIK06 conclude that GCs in their sample galaxies are well represented by point sources. However, as described in §3.2.3, our analysis is based on actual measured light profiles of the globular clusters. Therefore our aperture corrections vary depending on galaxy distance and filter. We believe our treatment of the aperture corrections is more accurate and realistic. For example, even though the aperture correction of 0.26mag SIK06 estimated is almost identical to that from our calculation of the PSF, the aperture corrections used for the GCs are greater than that of the PSF in all cases (see Table 3.2).

Regarding the total number of GCs, both studies selected a similar number of GC can-

didates for further analyses. For instance, SIK06 detected 660 and 1051 GCs for NGC3923 and NGC7626 respectively, whereas we find 662 and 1110 GCs. The difference in numbers of GCs is less than 50 objects for all the other galaxies in the sample. Moreover, the foreground/background contamination estimated shows a good agreement of around 15 objects for each galaxy. The overall shapes of the colour distributions are similar, however the peak positions of the blue and red sub-populations in SIK06 tend to be bluer than our estimation by a few hundredth of a magnitude (see Table 3.5). The reason for this, we believe, is the different aperture corrections as described above. The difference of aperture correction between the two filters is $\langle \Delta F606W - \Delta F814W \rangle = 0.07$mag on average, which is big enough to explain the blue shift of their colour distributions compared to our results. SIK06 also applied the same value of aperture correction to both filters, while our aperture correction of F814W is greater than that of F606W. Thus SIK06 slightly underestimate the amount of light in F814W so that their colour is slightly bluer than ours. Because SIK06 did not published an average of colour for their GCSs, we are not able to compare it directly. In terms of bimodality of the colour distributions, both works have a similar result. However, the SIK06 colour distributions for NGC7626 and NGC2865 show a rather complex shape, fitting neither a single nor double Gaussians.

Based on these colour distributions, SIK06 discuss the possible evidence for recent star formation in their sample galaxies. For NGC7626, the brightest GCs are provided as evidence of young GCs (2-5Gyr old) because they are $\sim$1mag more luminous than the bright GCs in other galaxies. Our results show little evidence for this conclusion. The distance modulus they infer from Roberts et al. (1991) determined from the HI systematic velocity is 33.41, which is 0.4mag greater than our adopted distance modulus, 33.01, from Prugniel & Simien (1996) using the recessional velocity and assuming $H_0 = 75 km/s/Mpc$. If a distance modulus of NGC7626 is derived from the GCLF in §3.3.2, assuming an absolute turn-over magnitude of $M_{V,TO} = -7.4 \pm 0.2$, the derived distance modulus would be 33.0. This value is also

Table 3.5: Comparison with Sikkema et al. (2006)

Host Galaxy	Sikkema et al. (2006)				This work			
	Blue Peak	Red Peak	p-value	Bimodality	Blue Peak	Red Peak	p-value	Bimodality
NGC3923	0.94	1.16	0.036	YES	0.97	1.20	0.000	YES
NGC7626	0.92	1.13	0.039	Not sure	0.99	1.21	0.000	YES
NGC5892	0.96	1.24	0.000	YES	0.98	1.23	0.000	YES
NGC2865	0.85	1.12	0.039	Not sure	0.99		0.554	NO
NGC1344	0.92	1.21	0.004	NO	0.99		0.606	NO
NGC474	0.90	1.22	0.035	NO	0.94		0.998	NO

more comparable to our adopted distance modulus than that used by SIK06. If we use our adopted distance modulus, the evidence for young GCs becomes not very strong. For NGC2865, SIK06 regarded the excess of blue GCs as evidence for very young GCs (0.5-1Gyr old). This is also not found in our results. Figure 3.10 and Table 3.5 show that the position of the blue peak in this galaxy is almost consistent with other galaxies in the sample, while the blue peak estimated by SIK06 is significantly bluer than those of other galaxies. These colour differences are possibly because of the different aperture corrections adopted as described in the previous paragraph. These two arguments in SIK06 also seem to be somewhat self-contradictory; if the bright GCs in NGC7626 are young, then the even younger GCs in NGC2865 would be expected to be even more luminous but they are not found to be so.

3.4.2 Application of Yoon et al. (2006)'s model

Yoon et al. (2006; hereafter YOO06) explained the bimodality of the GC colour distributions in elliptical galaxies differently from previous works. YOO06 argue that the bimodality in colour does not necessarily require a bimodality in metallicity if there is a non-linear relation

between colour and metallicity caused by horizontal branch stars. In this case YOO06 demonstrate that even a single broad Gaussian metallicity distribution can produce double peaks in the colour distribution. We therefore tested this hypothesis on our own results of the GCS in each galaxy independently. We take the average colours from our sample (Table 3.3), and convert to metallicity based on the colour-metallicity relation from YOO06. After simulating one million GCs having a Gaussian distribution with the mean metallicity obtained above and $\sigma([Fe/H]) = 0.5$, the metallicities of the individual GCs are converted to colour using YOO06's model. In addition, the simulated GCs are distributed in brightness using the luminosity functions from our actual data (Table 3.4). Photometric errors from our analysis are then added.

Figure 3.15 shows the comparison of the actual colour histograms with those from the simulated GC data. Even though there are some deviations, which can be reduced by adjusting the scatter of the metallicity distribution, our test suggests that even single peak distributions in metallicity can reproduce double peaks in the colour distribution. However, this still does not rule out the possibility that some mixture of two components in metallicity also results in the bimodallity in colour when using the non-linear relation. Inferring an original metallicity distribution from an observational colour distribution still has many uncertainties arising from colour-metallicity relations (either empirical or from simple stellar population models) and whether there are assumed to be one or two populations.

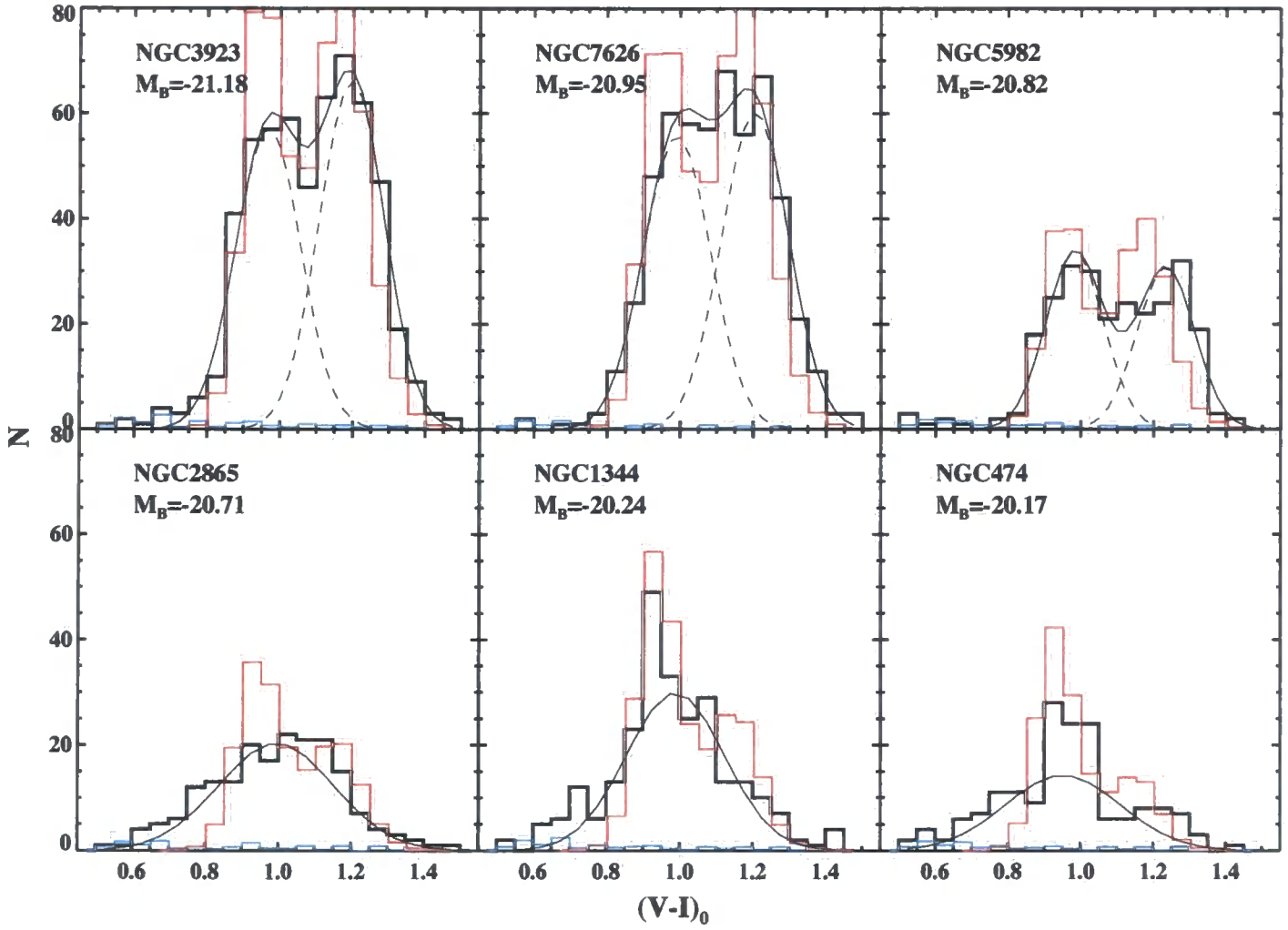

Figure 3.15: Comparison between the observational colour histogram and the simulated histogram based on Yoon et al. (2006)'s model. The black histograms are our observational colour distributions, and the blue histograms represent the contamination level. The red histograms are produced from the simulated GCs (see text for details).

Some critics have argued that horizontal branch stars cannot have that much effect on the integrated light of GCs, and that the linear and non-linear relations are not distinguishable with current observational data (e.g. Spitler et al. 2008). There is also direct evidence that in some galaxies the metallicity distribution is not unimodal. For example the GCSs in the Milky Way and M31 show a clear bimodality in metallicity (see Figure 1.4). Strader et al. (2007) shows two distinct GC subpopulations from spectroscopically derived metallicities for 47 GCs in NGC4472 (M49), the most luminous galaxy in the Virgo cluster. Beasley et al. (2008) found a strong evidence that the spectroscopic metallicity distribution for 207 GCs in NGC5128 is multimodal. Using an optical/mid IR colour (R-[3.6]), which is insensitive to horizontal branch stars, Spitler et al. (2008) also detected a strong bimodality in the colour distribution of GCS in NGC5128. This implies that the metallicity distribution is indeed bimodal as the metallicity-colour transform is more likely linear in optical/mid IR colours (see Figure 7 in Spitler et al. (2008)). Kundu & Zepf (2007) also detect a bimodality in the I-H colour distribution in GCS of M87 and demonstrate that the properties of the blue and red peaks of the M87 GCS do not change with distance from the center of M87, in conflict with YOO06's prediction that the blue and red peaks should get bluer with radial distance as average metallicity decreases.

3.5 Conclusions

- Three of the six shell ellipticals had already been observed with the HST/WFPC2. By comparison with these previous observations, we confirmed that the ACS does a much better job than WFPC2 with the benefits of its higher spatial resolution, larger field of view, and higher quantum efficiency, detecting almost four times more GCs and finding bimodality of some colour distributions that were previously thought to be unimodal.

- With the high resolution of the ACS, GCs far up to $D \sim 40$ Mpc are marginally

resolved. Photometry of such GCs needs great care. Assuming GCs are point sources can result in misleading outcomes.

- Overall the trends of GCS colour distributions in our shell elliptical sample follow those in normal galaxies. Bimodal colour distributions are more common in more luminous galaxies and the colour peaks of the blue and red subpopulations agree well with those in normal early-type galaxies. Shell galaxies appear like normal galaxies in their GCS properties.

- We found no evidence for young GC subpopulations associated with the shell formation epoch, although Sikkema et al. (2006) found some very blue GCs (possibly young GCs) in some shell galaxies. We suspect that this different result is due to the different way of treating aperture corrections.

- We have tested the hypothesis suggested by Yoon et al. (2006) that a non-linear colour-metallicity relation can produce a bimodal colour distribution even when the underlying metallicity distribution is unimodal. The application of this model to our colour distributions shows that this hypothesis is plausible. However, direct evidence of metallicity bimodality in some galaxies including the Milky Way and some giant elliptical galaxies appears to be against this hypothesis.

Chapter 4

Globular Cluster Systems of Early-type Galaxies in Low-density Environments

As mentioned in Chapter 1, globular cluster systems (GCSs) are powerful tools to explore their host galaxy formation history. Large surveys have revealed that the properties of galaxies in cluster environments differ from those in the field (e.g. Lewis et al. 2002), and semi-analytic models (e.g. Baugh et al. 1996) predict that low luminosity field galaxies should be younger and more metal poor than cluster galaxies. However, most studies of extragalactic globular cluster systems in early-type galaxies have focused on galaxies in rich cluster environments. We have therefore observed 10 low luminosity early-type galaxies in low density environments with HST/ACS in two colours, F475W (~Sloan g) and F850LP (~Sloan z), to investigate the properties of GCSs in these galaxies. We select globular cluster candidates using morphological and photometric properties to produce samples with very low contaminations and good completeness. Galaxies from the ACS Virgo Cluster Survey (Côté et al. 2004; ACSVCS) were chosen as a counterpart in high-density environments

and comparison with them reveals that there are some common as well as some different characteristics in the properties of GCSs between field and cluster environments.

4.1 Sample Selection and Observation

In order to obtain a well-defined sample of early-type galaxies with low luminosity and in low-density environments, we first compiled a complete sample of galaxies with $-5 \leq H_{code} \leq -2$[1], $-18.0 < M_B < -19.5$[2], distance $D \lesssim 30Mpc$, Galactic latitude $|b| \gtrsim 45\,\mathrm{deg}$, and local density $\rho_0 < 1.0Mpc^{-3}$ from the Nearby Galaxy Catalogue(NBG) (Tully, 1988). After visual inspection of the Digitized Sky Survey images, 10 of the brightest targets in apparent magnitude without nearby bright stars within the ACS field of view were selected. The properties of our final sample of early-type galaxies in low-density environments are listed in Table 4.1 in descending order of absolute luminosity. The local densities for 47 galaxies from the ACSVCS sample are also available in the NBG, including all ACSVCS galaxies within the luminosity range of our sample. The left panel of Figure 4.1 demonstrates not only the clear separation in local density between our field galaxy sample and the ACSVCS sample, but also that the sample in low-density environments is more representative of early-type galaxies in general. The right panel shows the distribution in absolute magnitude of our sample and the ACSVCS.

The observations (Program ID: 10554) were carried out with the ACS Wide Field Camera (WFC) on the Hubble Space Telescope during Cycle 14 (Oct 05 - Sep 06). The WFC is composed of two 4K×2K chips with a pixel scale of $0.05''/pix$, covering a field of view of $202''\times202''$. Each galaxy used 2 orbits to obtain images in the two bands, F475W and F850LP, which correspond to Sloan g and z respectively. These two filters were also used

[1]This is a morphological type code. Elliptical and lenticular galaxies are included in this range.

[2]The absolute magnitudes of galaxies listed in the NBG scatter by ~ 0.5mag compared to the values from the NASA Extragalactic Database (NED). We adopt the values from the NED for the presents analysis.

Table 4.1: Galaxy Properties

Name	M_B	RA(J2000) (h:m:s)	DEC(J2000) (°:′:″)	Type	m-M	B_T	E(B-V)	Density ($/Mpc^3$)
NGC3818	-20.33	11:41:57.36	-06:09:20.4	E5	32.80	12.47	0.036	0.20
NGC7173	-19.96	22:02:03.19	-31:58:25.3	E+ p	32.48	12.52	0.026	0.35
NGC1439	-19.95	03:44:49.95	-21:55:14.0	E1	32.13	12.18	0.030	0.45
NGC1426	-19.65	03:42:49.11	-22:06:30.1	E4	31.91	12.26	0.017	0.66
NGC3377	-19.18	10:47:42.40	+13:59:08.3	E5	30.25	11.07	0.034	0.49
NGC4033	-19.11	12:00:34.74	-17:50:33.4	E6	31.64	12.53	0.047	0.38
NGC1172	-19.10	03:01:36.05	-14:50:11.7	E+	31.66	12.56	0.064	0.28
NGC3156	-18.84	10:12:41.25	+03:07:45.7	S0	31.75	12.91	0.034	0.20
NGC3073	-18.78	10:00:52.08	+55:37:07.8	SAB0	32.64	13.86	0.010	0.28
IC2035	-18.57	04:09:01.87	-45:31:03.1	S0	31.18	12.61	0.013	0.16

Col. 1: Galaxy name; Col. 2: Absolute B magnitude; Col. 3: RA, Dec; Col. 4: Morphological type; Col. 5: Distance modulus; Col. 6: Total apparent B magnitude; Col. 7: Galactic reddening; Col. 8: Local density. The morphological type and apparent B magnitude are taken from NED. The distance moduli are SBF values from Tonry et al. (2001) except for IC2035 where the distance modulus was estimated using the redshift from NED. The Galactic extinction is taken from Schlegel, Finkbeiner, & Davis (1998) and the local density from Tully (1988).

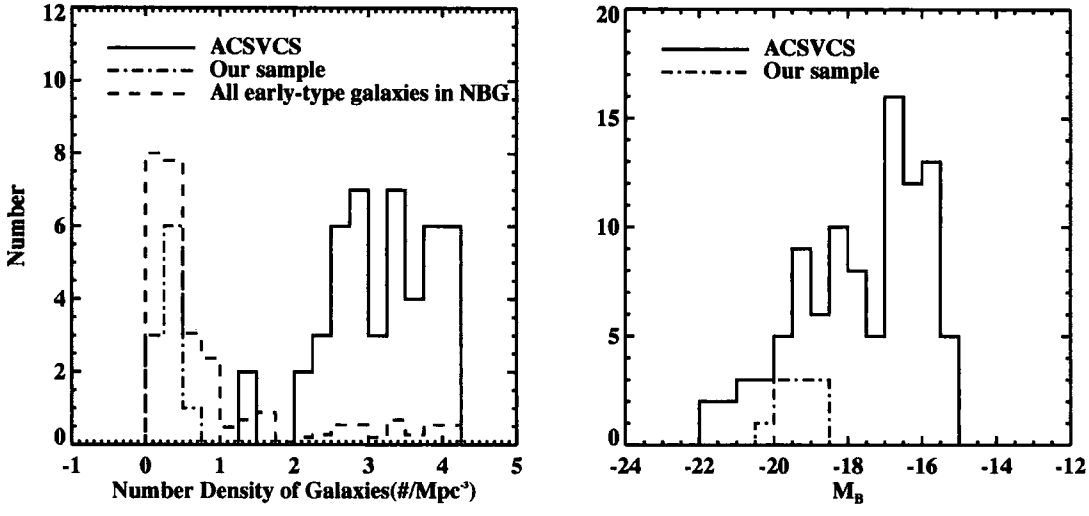

Figure 4.1: Distribution of local density and luminosity for our sample and the ACSVCS showing the clear separation in environment between the two samples. The distribution of all early-type galaxies in the NBG is plotted with a dashed line on an arbitrary scale.

by the ACSVCS, which has the advantage of being able to compare results directly without any photometric transformations. We used a four-point line dithering pattern, in which the telescope pointing shifts 5×60 pixels between subexposures. This allows us to fill the gap between the two chips and to eliminate hot pixels during data processing. Because dithering also removes cosmic rays effectively, `CR-SPLIT` was set to NO. We maximize total exposure times by arranging 8 sub-exposures in the following way. At the first orbit, four sub-exposures of F475W and one sub-exposure of F850LP were allocated. At the second orbit, three sub-exposures of F850LP were obtained. Actual total exposure times depend one target visibility; typical exposure times were 1300s and 3000s for F475W and F850LP respectively. The observation logs are listed in Table 4.2; for NGC3156, the pointing and orientation were adjusted slightly to avoid adjacent bright stars. Figure 4.2 shows the ACS images in the F475W band of a $1' \times 1'$ central region for the sample galaxies.

Table 4.2: Observation Log

Target	Date	Filter	Exp. Time (sec)	Dataset
NGC3818	2006-01-01	F475W	1380	J9CZ04010
		F850LP	2987	J9CZ04020
NGC7173	2006-05-16	F475W	1375	J9CZ10010
		F850LP	3075	J9CZ10020
NGC1439	2006-08-21	F475W	1375	J9CZ06010
		F850LP	3023	J9CZ06020
NGC1426	2006-08-21	F475W	1375	J9CZ09010
		F850LP	3023	J9CZ09020
NGC3377	2006-01-13	F475W	1380	J9CZ08010
		F850LP	3005	J9CZ08020
NGC4033	2006-01-04	F475W	1380	J9CZ07010
		F850LP	3017	J9CZ07020
NGC1172	2006-08-17	F475W	1380	J9CZ03010
		F850LP	3005	J9CZ03020
NGC3156	2005-10-30	F475W	1380	J9CZ02010
		F850LP	2972	J9CZ02020
NGC3073	2006-05-14	F475W	1428	J9CZ05010
		F850LP	3490	J9CZ05020
IC2035	2006-04-28	F475W	1380	J9CZ01010
		F850LP	3299	J9CZ01020

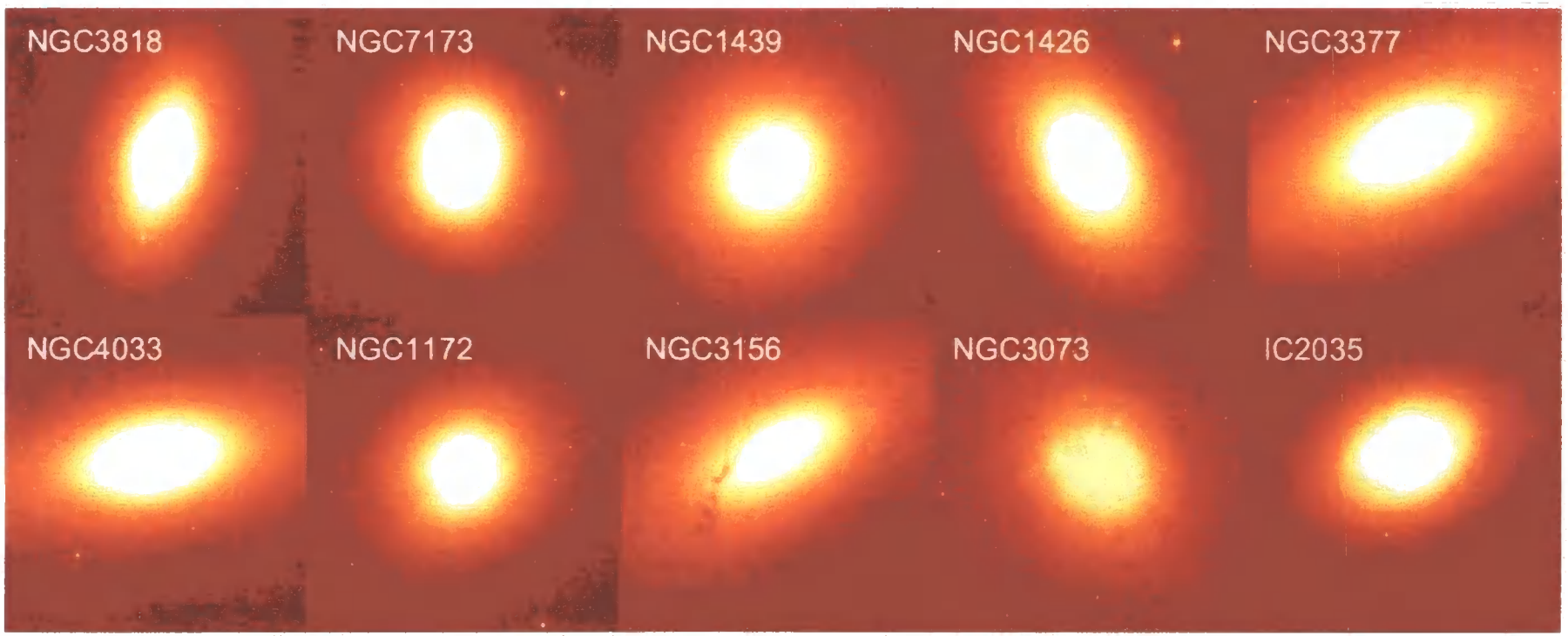

Figure 4.2: F475W band images of the $1' \times 1'$ central region of the sample galaxies. The high resolution ACS/WFC images are very effective at revealing central dust lanes and other morphological features invisible on deep ground-based images (e.g. DSS).

4.2 Data Reduction

4.2.1 Basic image reduction

Each target has four sub-exposure images with different dithering positions in each filter. These raw images were reduced using the default ACS pipeline, *CALACS*, to produce bias subtracted and flat-field corrected images. We found that because of the large contribution of galaxy light in these images, the default processing overestimates the sky background slightly, resulting in negative background levels on the outskirts of a galaxy in the final drizzled images. We determined an improved sky background by adopting the minimum level from the median values of four 200pix $\times$ 200pix corners of each subexposure. The four subexposure images were combined and geometric-corrected using the *MultiDrizzle* package. The final drizzled image consists of a 4096$\times$4096 pixel science image in the unit of electrons/sec and an error map in the second extension containing all the error sources such as readout noise, dark current and photon background noise.

4.2.2 Galaxy light subtraction

The smooth galaxy light of each target was fitted with elliptical isophotes using the *IRAF/ELLIPSE* routine. Fitted ellipse parameter tables were then used to build a galaxy model image using the *IRAF/BMODEL* task. Another use of these tables is to derive a surface brightness profile and structure parameters such as position angle, effective radius and an ellipticity profile. The model galaxy was then subtracted from the original image. It was found that subtracting the galaxy continuum light improves the efficiency of detecting GCs in the central regions of a galaxy.

4.2.3 GC detection and selection

On the galaxy-light subtracted images we ran *SExtractor* (Bertin & Arnouts, 1996) to detect GC candidates with a 3σ detection limit above the background. In order to properly account for noise due to the diffuse galaxy light, the error map from the drizzled images was used to create a weight image in *SExtractor*. From the detected objects we rejected objects with `ELONGATION` > 2 in either the F475W or F850LP band, and any very diffuse ones with `CLASS_STAR` < 0.9 in the F475W band. Objects were matched within 2 pixels radius across the two bands. At the edge of the images we found some spurious detections, which were manually removed.

4.2.4 GC Photometry

Once the list of GC candidates had been generated, we performed aperture photometry using 1 to 10 pixel radius apertures in one pixel steps using the *IRAF/PHOT* package on the galaxy-subtracted images. The background was estimated locally from a 10 to 20 pixel radius annulus. This locally estimated background has an advantage that the photometry of GCs is barely affected by the global sky background estimation and modeling of the underlying galaxy light. Because GCs are marginally resolved by ACS/WFC at the distance of our sample galaxies, the aperture correction from stellar PSFs would not be applicable to our GCs. Instead we constructed a representative GC model profile from several moderately bright GCs for each galaxy using the *IRAF/PSF task*, from which growth curves were extracted. Figure 4.3 clearly shows that the GCs are not point sources, and verifies that the light profiles of the GCs in the closest galaxy, NGC 3377, are the most extended.

An aperture correction for GCs in each galaxy was determined from the magnitude difference between the 3 pixel and 10 pixel radius apertures on the growth curve (Table 4.3). This aperture correction was then applied to the 3 pixel radius aperture photometry for all of the GC candidates. This can be justified by the fact that the sizes of GCs are

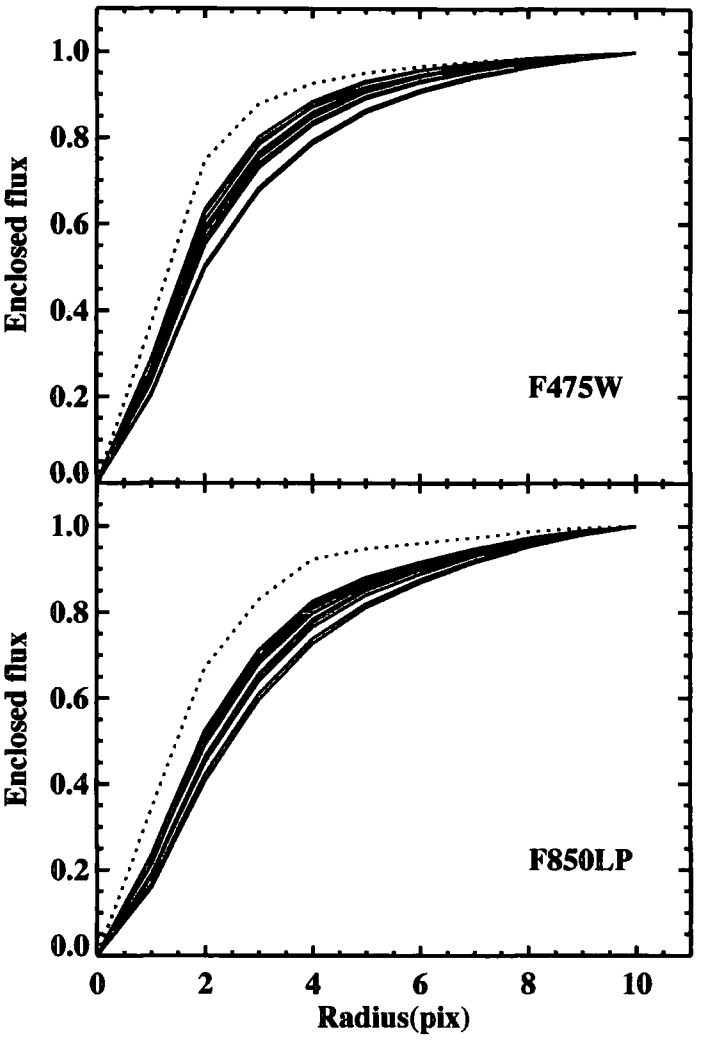

Figure 4.3: Growth curves of bright GCs in the different sample galaxies. The dotted lines are growth curves for the ACS PSF. The GCs are clearly more extended than a point source. The most extended profile is in fact the one from the closest galaxy (NGC 3377).

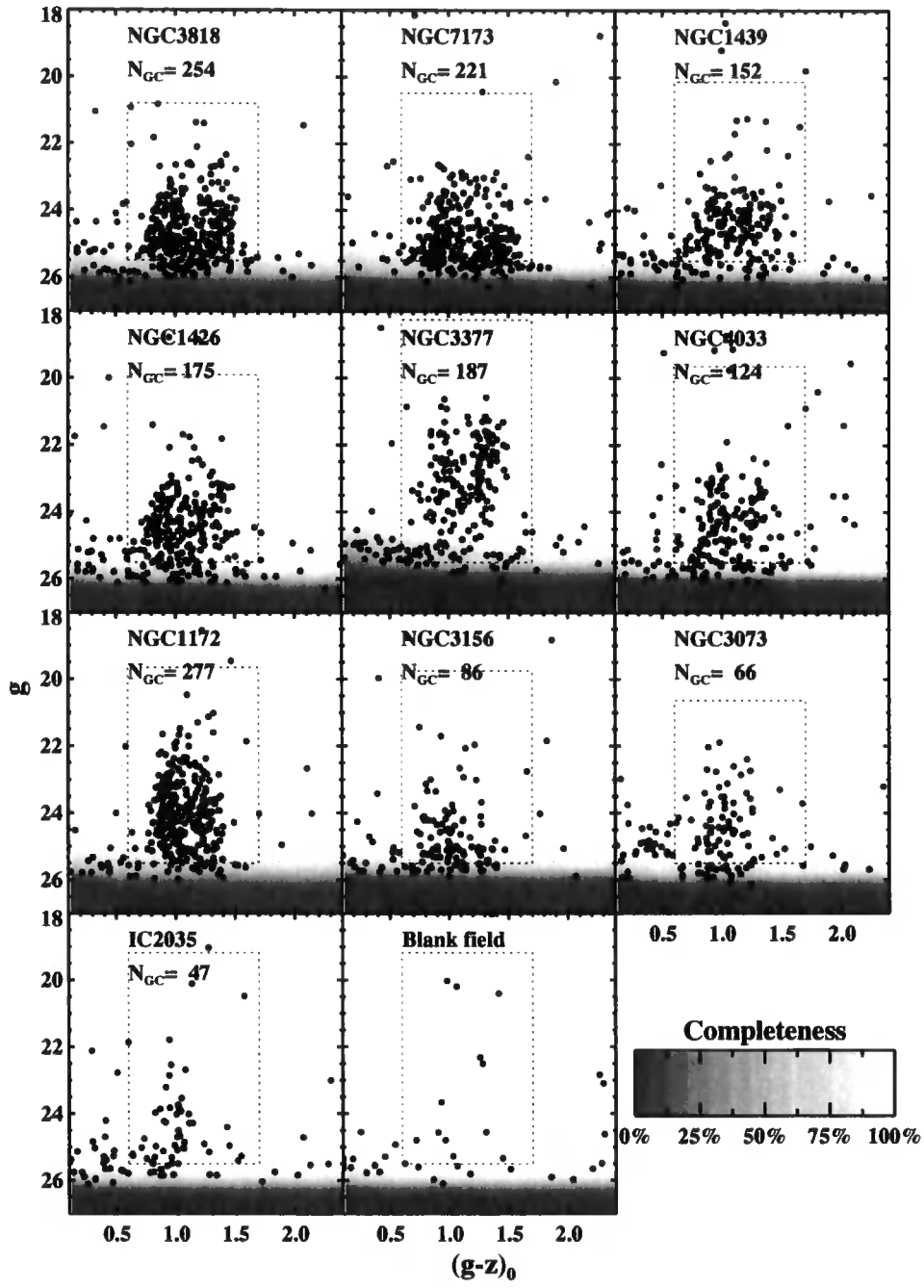

Figure 4.4: The colour-magnitude diagram of GC candidates; the parent galaxies are ordered from most luminous to least luminous. The dotted box indicates the colour cut and the magnitude cut applied. The number of GCs in this box is denoted along with the galaxy name. The background grey scale visualizes the completeness at a given magnitude and colour. The bottom-center panel shows an example of contamination per field, after one out of six objects are randomly selected from 6 compiled blank fields.

Table 4.3: Aperture correction magnitudes from 3 pixel to 10 pixel radius aperture

	ΔF475	ΔF850LP
NGC3818 GCs	0.254	0.399
NGC7173 GCs	0.241	0.372
NGC1439 GCs	0.292	0.416
NGC1426 GCs	0.299	0.444
NGC3377 GCs	0.414	0.543
NGC4033 GCs	0.327	0.466
NGC1172 GCs	0.341	0.479
NGC3156 GCs	0.309	0.414
NGC3073 GCs	0.424	0.531
IC2035 GCs	0.263	0.420

independent of their luminosity (Jordán et al., 2005). The final corrections from 10 pixel radius to total magnitudes are primarily a function of the ACS/WFC PSF and are 0.095 for F475W and 0.117 for F850LP; the zero-points of the ABmag scale are 26.068 and 24.862 for F475W and F850LP respectively (Sirianni et al., 2005). Finally Galactic extinction was corrected for based on the Schlegel, Finkbeiner, & Davis (1998) extinction map values(listed in Table 4.1) and the extinction ratios, $A_{F475W} = 3.634E(B-V)$ and $A_{F850LP} = 1.485E(B-V)$ from Sirianni et al. (2005). Hereafter g and z magnitudes refer to the F475W and F850LP extinction-corrected total ABmag. The colour-magnitude diagrams for the GC candidates are shown in Figure 4.4 ordered by luminosity, with the most luminous galaxy in the top-left panel.

4.2.5 GC Completeness tests

To test the effectiveness of our GC detection and selection method, we generated a list of 1000 artificial GCs with a uniform luminosity function and spatial distribution in both filters independently, and then added them on a galaxy subtracted image, which contains all the noise sources such as readout noise and poisson errors from sky and galaxy light. The artificial GCs were simulated using *IRAF/MKOBJECTS* with the representative GC light profile previously constructed in §4.2.4. Then as described in § 4.2.3, we repeated the GC detection and selection procedures and match the initial input coordinates of artificial GCs with the recovered ones. For a given magnitude bin, the number fractions of recovered GCs are calculated.

A completeness curve can often be expressed by the analytic function,

$$f = \frac{1}{2}\Big(1 - \frac{a(m - m_0)}{\sqrt{1 + a^2(m - m_0)^2}}\Big) \tag{4.1}$$

where m_0 is a magnitude where f is 0.5, and a controls how quickly f declines (the larger a, the steeper is the transformation from 1 to 0) (Harris 2001). Figure 4.5 shows an example of completeness in one of the galaxies. The fitted parameters of Equation 4.1 are listed in Table 4.4. The completeness in each galaxy a given magnitude and colour is displayed as a grey scale in Figure 4.4. It is calculated by multiplying the completeness in g and z at over a grid of small boxes on the colour-magnitude plane. The completeness levels in g decline more steeply than in z as seen in Figure 4.5 and Table 4.4, because the additional selection criterion in g, $CLASS\_STAR > 0.9$, rejects faint GCs more quickly due to the increasing uncertainty of `CLASS_STAR` with fainter GCs.

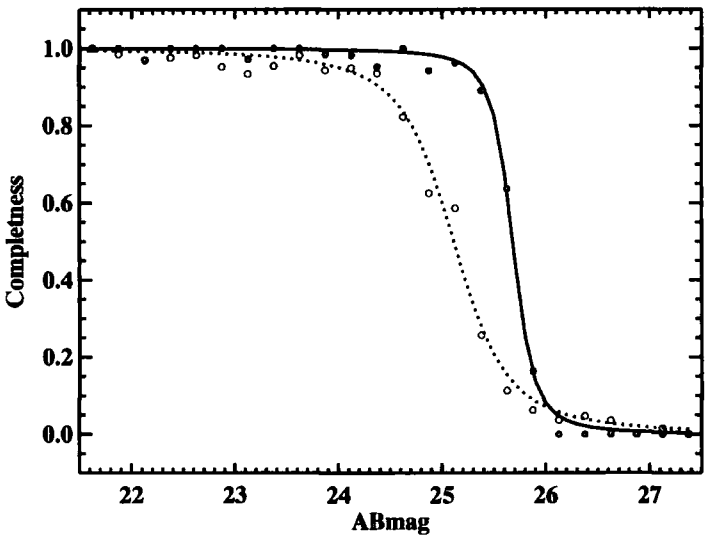

Figure 4.5: The completeness of GC detections in NGC3377. The filled and open circles are the completeness of the g and z bands respectively. The solid and dotted lines are the fitted curves from Equation 4.1.

Table 4.4: Parameters of completeness functions

	F475W		F850LP	
	m_0	a	m_0	a
NGC3818	25.94	4.29	25.79	3.06
NGC7173	25.93	5.24	25.74	2.73
NGC1439	26.01	6.17	25.84	3.12
NGC1426	26.05	5.55	25.85	3.44
NGC3377	25.68	4.81	25.11	1.88
NGC4033	25.90	7.06	25.81	3.81
NGC1172	25.86	3.85	25.65	4.03
NGC3156	25.77	4.88	25.65	5.10
NGC3073	25.92	5.48	25.79	3.88
IC2035	26.10	6.77	26.02	4.85

4.2.6 Contamination of background galaxies

Although our selection criteria are quite tight, inevitably some amount of contamination by background galaxies is expected (contamination by foreground stars is small at these magnitudes with our selection criteria.). To estimate this contamination statistically, we searched the ACS archive for high Galactic latitude blank-fields observed with the same filters and at least as deep as our observations. In total six blank fields were retrieved. One field usually consists of 4-6 subexposures, which were combined into one image by taking median values using *IRAF/IMCOMBINE*. We apply the same GC detection and selection techniques to these images. Since the observation conditions of the blank fields are not exactly the same as ours (e.g. exposure time and dithering), we have to take this difference into account. We found that some hot pixels were misclassified as GCs in the blank fields, which were removed by applying an additional classification, `FWHM_IMAGE` < 1.5. In the bottom-center panel in Figure 4.4, one out of every six objects in the 6 blank fields that passed the selection criteria are randomly chosen and plotted. Then, because the blank fields are deeper than ours, the completeness of each galaxy was applied to obtain the colour distribution and luminosity function of the contamination for each galaxy. These contamination profiles were used in the subsequent analysis. The typical contamination per field is $\sim$14 objects.

4.3 Results

4.3.1 Colour Distributions

To construct the GC colour distributions, we refined the sample of GC candidates by applying the colour cut, $0.6 < (g-z)_0 < 1.7$, and the magnitude cut, $M_g > -12.0$,and $g < 25.5$, where the completeness is $\approx 80\%$. These colour and magnitude selections are indicated by the dotted box in Figure 4.4. In Figure 4.6, the raw distribution is drawn with a black

histogram. The red histogram represents the expected contamination level mentioned in the above section. For each colour bin, the number of contaminating objects was removed from the raw distribution, with the green histogram displaying the contamination-corrected colour distribution. The panels in Figure 4.6 are placed in the same order as in Figure 4.4.

In order to test the significance of any colour bimodality statistically, we employed the KMM test (Ashman, Bird, & Zepf, 1994), which estimates the probability (P-value) that two distinct Gaussians with the same dispersion are a better-fit to the observational data than a single Gaussian using likelihood ratio test statistics. After running the KMM test for 100 bootstrap resamples of the contamination corrected colours, we estimate the peaks of the colour histograms, sigma of subpopulations, fraction of red population, P-value and fraction of P-values that are less than 0.05 (Table 4.5(a)), in which the representative values are median values of 100 KMM outputs, and uncertainties are half a width within which 68% of the data are contained relative to the median. Since the KMM outputs have a somewhat skewed distribution (especially the P-values are highly skewed), a median is a more robust estimation than a mean value. The statistical interpretation of the P-value is that a distribution with a P-value of 0.05 favours bimodality rather than unimodality with a 95% confidence. In Figure 4.6, the results of KMM tests for each sub group are plotted with dashed lines, and the sum of the two groups with solid lines. We decide the significance of colour bimodality on the basis of $\langle P \rangle$, and the fraction of $P < 0.05$. For $\langle P \rangle < 0.05$ and $f_{(P<0.05)} > 0.90$, a distribution is interpreted as a strong bimodal distribution, for either $0.05 < \langle P \rangle < 0.10$ or $0.50 < f_{(P<0.05)} < 0.90$ one to be likely bimodal, and otherwise unimodal. For IC2035, despite its small P-value, we regard this galaxy as unimodal because of the insignificant number of red clusters. The significance of bimodality is listed as S(trong), L(ikely), or U(nimodal) in Table 4.5.

The ability of the KMM test to detect bimodality depends on the sample number and the normalized separation between the two peaks (see Ashman, Bird, & Zepf 1994). For example,

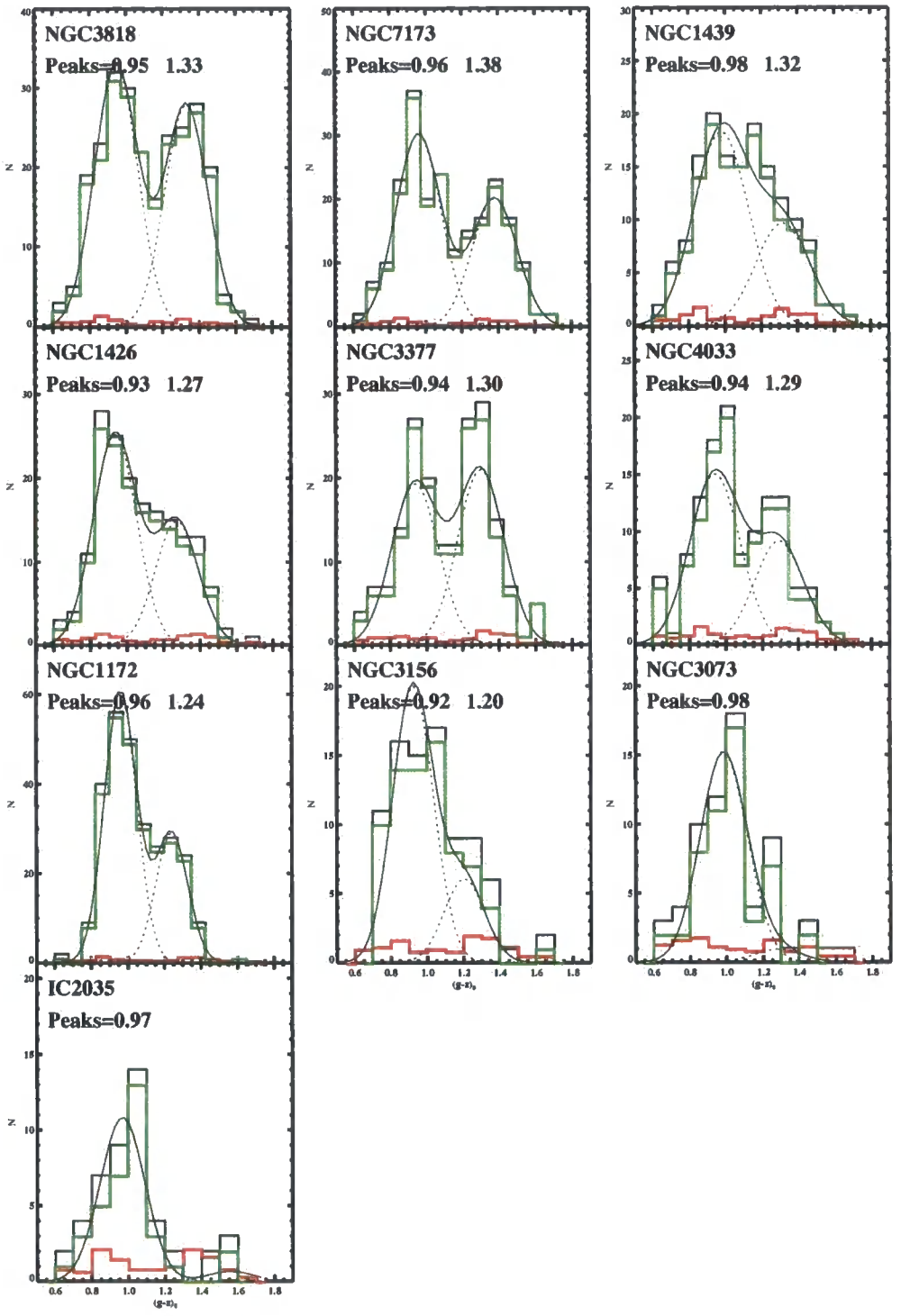

Figure 4.6: Colour distributions of GC candidates. The black histograms are colour distributions of raw data. The red histograms are contamination. The green histograms are after correcting contamination. The KMM results for subpopulations are drawn with dashed lines, and the solid lines are the sum of the two subpopulation.

Table 4.5: Properties of GCs: Colour Distribution

Host galaxy	N_{GC}	Blue Peak	Red Peak	σ_{sub}	f_{red}	$\langle P \rangle$	$f(P < 0.05)$	Bimod.	$\langle (g-z)_0 \rangle$
(a)					$0.6 < (g-z)_0 < 1.7$				
NGC3818	240	0.95 ± 0.01	1.33 ± 0.02	0.12	0.46	<0.01	1.00	S	1.12 ± 0.01
NGC7173	208	0.96 ± 0.01	1.38 ± 0.02	0.12	0.40	<0.01	1.00	S	1.13 ± 0.02
NGC1439	139	0.98 ± 0.03	1.32 ± 0.04	0.15	0.35	0.02 ± 0.09	0.63	L	1.10 ± 0.02
NGC1426	159	0.93 ± 0.02	1.27 ± 0.02	0.12	0.37	<0.01	0.99	S	1.06 ± 0.02
NGC3377	173	0.94 ± 0.02	1.30 ± 0.02	0.13	0.52	<0.01	0.96	S	1.13 ± 0.02
NGC4033	111	0.94 ± 0.03	1.29 ± 0.03	0.14	0.38	0.03 ± 0.16	0.56	L	1.07 ± 0.02
NGC1172	265	0.96 ± 0.01	1.24 ± 0.02	0.09	0.32	<0.01	1.00	S	1.05 ± 0.01
NGC3156	74	0.95 ± 0.05	1.29 ± 0.20	0.13	0.16	0.03 ± 0.09	0.57	L	1.01 ± 0.02
NGC3073	52	0.98 ± 0.03	...	0.13	0.06	0.28 ± 0.42	0.16	U	1.02 ± 0.02
IC2035	35	0.97 ± 0.03	...	0.12	0.06	<0.01	0.83	U	1.00 ± 0.03
(b)					$0.7 < (g-z)_0 < 1.6$				
NGC3818	236	0.95 ± 0.01	1.33 ± 0.01	0.11	0.46	<0.01	1.00	S	1.12 ± 0.01
NGC7173	201	0.97 ± 0.01	1.37 ± 0.02	0.11	0.40	<0.01	1.00	S	1.14 ± 0.02
NGC1439	134	0.98 ± 0.02	1.30 ± 0.04	0.13	0.39	0.01 ± 0.02	0.84	L	1.10 ± 0.02
NGC1426	157	0.94 ± 0.02	1.28 ± 0.02	0.11	0.38	<0.01	1.00	S	1.07 ± 0.02
NGC3377	165	0.95 ± 0.01	1.30 ± 0.01	0.11	0.53	<0.01	1.00	S	1.13 ± 0.02
NGC4033	105	0.95 ± 0.01	1.30 ± 0.02	0.11	0.40	<0.01	0.98	L	1.09 ± 0.02
NGC1172	264	0.96 ± 0.01	1.24 ± 0.01	0.09	0.33	<0.01	1.00	S	1.05 ± 0.01
NGC3156	73	0.92 ± 0.03	1.20 ± 0.05	0.11	0.23	0.09 ± 0.15	0.40	L	1.00 ± 0.02
NGC3073	50	0.99 ± 0.03	...	0.11	0.16	0.08 ± 0.27	0.42	U	1.03 ± 0.02
IC2035	34	0.98 ± 0.02	...	0.11	0.06	<0.01	0.88	U	1.01 ± 0.03

the larger the sample size and the larger the separation of the two subcomponents, the higher the chance to detect bimodality. Moreover, the extended tails of the distribution can also affect the results. We have therefore tested an alternative GC sample with a narrower colour range $0.7 < (g-z)_0 < 1.6$. These results are listed in Table 4.5(b). It is found that clipping the tails decreases the P-value, in other words, without the extended tails the KMM test is more likely to detect bimodality. This is not surprising because fitting extended tails results in a larger sigma for each subgroup, thus making it harder to separate two subgroups. In this experiment, however, the values of the fitted parameters do not vary significantly, remaining within the uncertainty estimated initially. There is one case where a fitted parameter, the red peak colour, has been changed significantly after clipping the tails: in NGC3156, there is one isolated very red GC (see middle-bottom panel in Figure 4.6), which makes the red peak significantly redder than when it is removed. It is potentially a background galaxy contaminant because it lies at a large projected distance from the galaxy center unlike other red GCs. For further analysis, the values from Table 4.5(a) are adopted, except in the case of NGC3156, for which we take the value from Table 4.5(b). Finally the results are overplotted in Figure 4.6.

It is noticeable that the colour bimodality of GCs is more common in the luminous galaxies. The red population gets weaker and moves to redder colour with decreasing galaxy luminosity, and eventually only a blue peak appears in the faint galaxies. The richness of the GCS also decreases with the host galaxy luminosity. None of our GC colour distributions have a single broad peak placed between the normal blue and red peaks, as has been found in some early-type galaxies in other environments (e.g. Larsen et al. 2001; Kundu & Whitmore 2001a; Peng et al. 2006a). We will discuss the behavior of the GC colour with host galaxy luminosity in more detail later.

4.3.2 Luminosity functions

Luminosity functions in the g and z bands were constructed using globular clusters within the colour range of $0.6 < (g-z)_0 < 1.7$ (black histograms in Figure 4.7 and Figure 4.8). The contamination (red histograms) estimated previously was subtracted from the raw distribution and incompleteness corrections applied. The corrected luminosity functions (green histograms) were fitted with a Gaussian function up to the 50% completeness limit. The fitted parameters (peak magnitude and standard deviation) and their uncertainties are listed in Table 4.6, where the missing data are those parameters having a large uncertainty caused by the small number of GC samples and some excess of faint GCs. For the luminous galaxies, Gaussian functions well represent the luminosity functions of GCSs. The arrows in Figure 4.7 and 4.8 indicate the expected turn-over magnitudes based on peak absolute magnitudes of the GC luminosity function (GCLF) of $\mu_g = -7.2$ and $\mu_z = -8.4$ as given by Jordán et al. (2007b).

4.3.3 Host galaxy properties vs. colours of GCs

It is well established that there is a strong correlation between mean colours/red peaks and host galaxy luminosities (e.g. Larsen et al. 2001; Kundu & Whitmore 2001a). However, there have been few measurements that support a correlation between the blue peak and host galaxy luminosity until the recent ACSVCS data found this relation with their large dynamic range of galaxy luminosity (Peng et al., 2006a).

In Figure 4.9, the peak colours of the sub-populations and mean GC colours are plotted against the host galaxy luminosity. Each relation is fitted to a straight line using weighted chi-squre minimization. It is clear that a strong dependency of the red peak and mean colour on host galaxy luminosity does exist in our field galaxies with almost identical slope. On the other hand, the blue peak is almost independent of galaxy luminosity. In fact, the fitted slope shows a weak anti-correlation, the statistical significance of which, however, is within

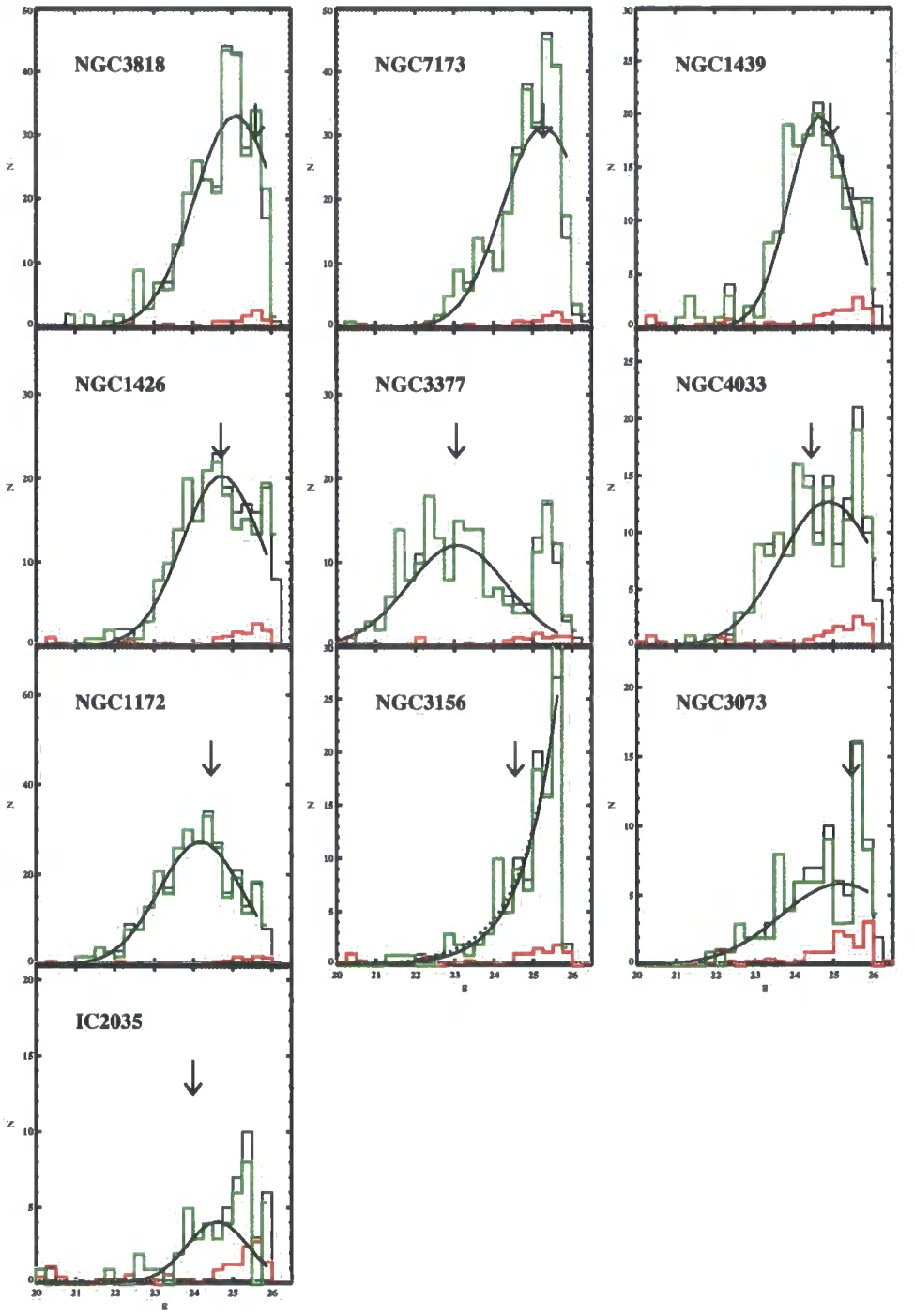

Figure 4.7: Luminosity functions of globular clusters in the g band. The black histograms are luminosity functions before correction. The red histograms are contamination estimates, and the green ones are luminosity functions corrected for background contamination and completeness. The solid curves are the best fit Gaussian curves, and the arrow indicates the expected turn-over position for each galaxy based on the GCLF parameters from (Jordán et al., 2007b).

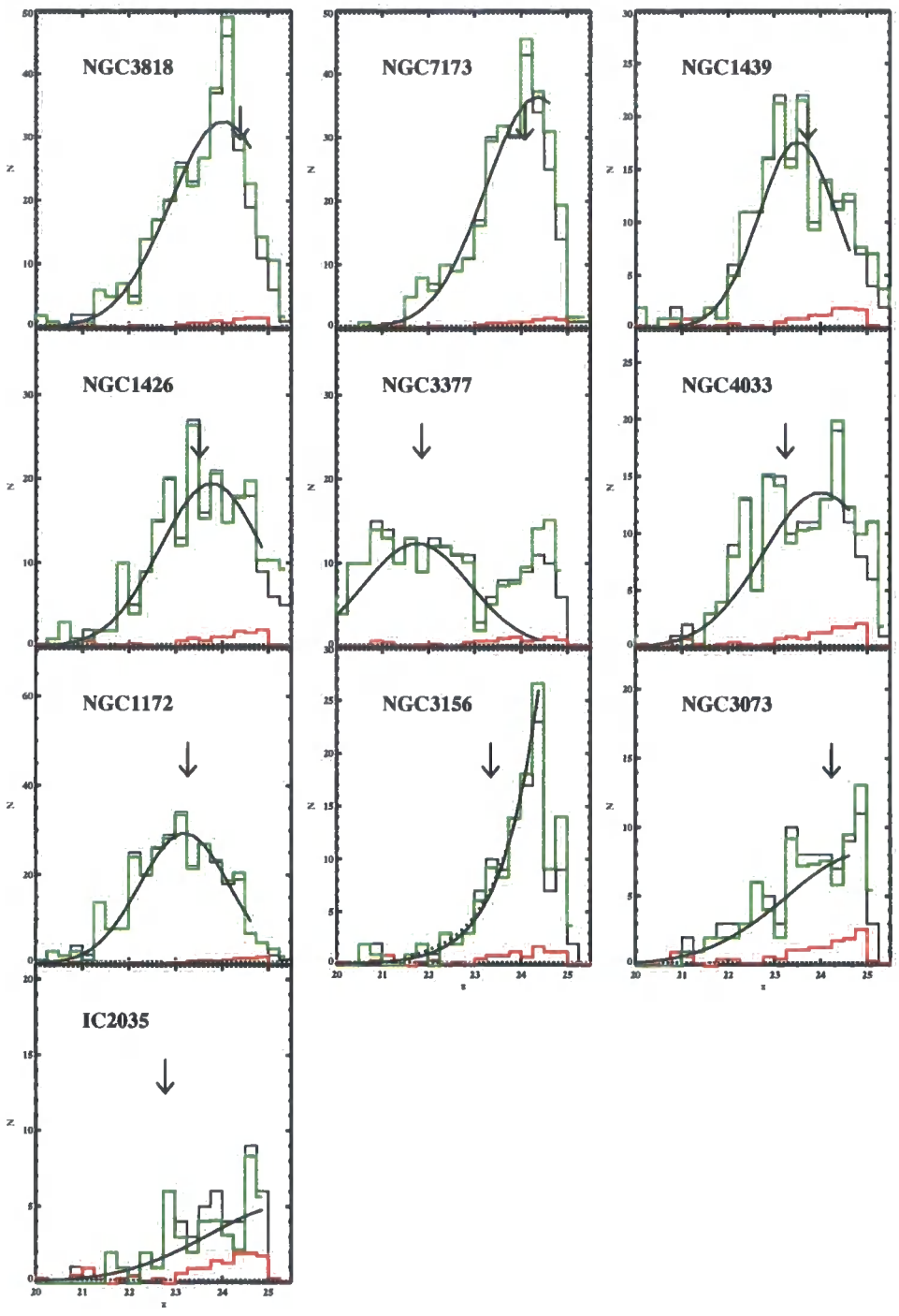

Figure 4.8: Luminosity functions of globular clusters in the z band. All the histograms and curves have the same meaning as in the g band luminosity functions in Figure 4.7.

Table 4.6: Gaussian fitted parameters of luminosity functions

Host galaxy	$m_{to,g}$	σ_g	$m_{to,z}$	σ_z
NGC3818	25.09 ± 0.13	1.05 ± 0.09	24.02 ± 0.17	1.14 ± 0.11
NGC7173	25.28 ± 0.15	1.04 ± 0.11	24.36 ± 0.24	1.12 ± 0.14
NGC1439	24.66 ± 0.08	0.77 ± 0.07	23.51 ± 0.10	0.84 ± 0.08
NGC1426	24.73 ± 0.12	1.02 ± 0.09	23.77 ± 0.14	1.11 ± 0.11
NGC3377	23.08 ± 0.12	1.25 ± 0.11	21.75 ± 0.11	1.14 ± 0.09
NGC4033	24.88 ± 0.24	1.22 ± 0.17	24.01 ± 0.33	1.26 ± 0.20
NGC1172	24.18 ± 0.09	1.06 ± 0.07	23.19 ± 0.07	0.96 ± 0.06
NGC3156	...	...	...	...
NGC3073	25.17 ± 0.67	1.53 ± 0.44	...	...
IC2035	24.60 ± 0.19	0.79 ± 0.17	...	...

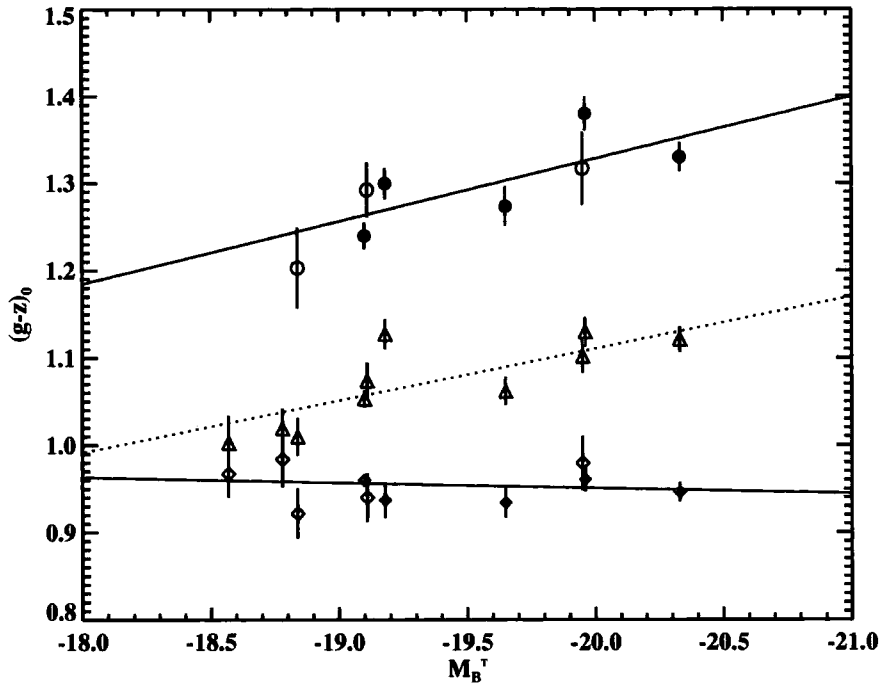

Figure 4.9: A plot of GC colours against host galaxy luminosity. The diamond and circle symbols represent the blue and red peaks respectively. Strong bimodality is indicated by a filled symbol,and marginal or zero bimodality by an open symbol. The mean colours of all GCs within a galaxy are plotted with an open triangle. The two solid lines are the least squares best fits to the blue and red peaks. The dotted line is fitted to the mean colour.

1σ of a zero slope. From our results alone, it is uncertain whether the absence of a blue peak gradient is due to the narrow dynamic range of luminosity in our field galaxy sample or an intrinsic effect across a wide range of luminosity. Our results clearly show that the observed trends in GC colours with host galaxy luminosity are the consequence of the gradual change in the fraction and colour of the red GCs, and not a systematic change of the colours of all GCs within a galaxy.

4.3.4 Comparison with the ACS Virgo Cluster Survey

The ACS Virgo Cluster Survey (ACSVCS) was a large programme to image 100 early-type galaxies in the Virgo cluster with the ACS in two filters (g and z bands) (Côté et al., 2004). The main scientific aims were to study the properties of globular cluster systems in these galaxies (e.g. Peng et al. 2006a; hereafter PJC06, Jordán et al. 2006), their central structures (Ferrarese et al., 2006), and to obtain accurate surface brightness fluctuation distances (Mei et al., 2007).

The observation conditions and data reduction procedures of the ACSVCS are somewhat different from those adopted here. The ACSVCS used 100 orbits of the HST, allocating only one orbit for each galaxy. Each galaxy of the ACSVCS has an exposure time of 750 sec in F475W and 1210 sec in the F850LP filter, while our exposure times are almost twice as long (typically 1300 sec in F457W and 3000 sec in F850LP). The data reduction procedures of the ACSVCS are described in detail by Jordán et al. (2004). In brief, the exposures were split into two or three sub-exposures, without repositioning, to remove cosmic rays; these sub-exposures were then reduced and combined using the standard ACS pipeline. Model galaxies were created using the *ELLIPROF* programme (Tonry et al., 1997) and subtracted from the original images. The *KINGPHOT* programme developed by Jordán et al. (2005) was used for photometry of the GCs and to measure their sizes. *KINGPHOT* fits King models convolved with a given point spread function in each filter to individual GC candidates and finds the best fit parameters of the King model. Total magnitudes for the GCs were calculated by integrating these best-fit convolved King models. All GCs are were selected based on magnitude ($g \geq 19.1$ or $z \geq 18.0$) and a mean elongation in the two filters $\langle e \rangle \leq 2$, where $\langle e \rangle \equiv a/b$. The main results on the colour distributions of the ACSVCS GCSs were published by PJC06, and are compared with our results below.

In Figure 4.10, our mean colours for the 10 GCSs in our sample are compared with the results from PJC06. Our mean colours generally appear to be located at the bluer end of

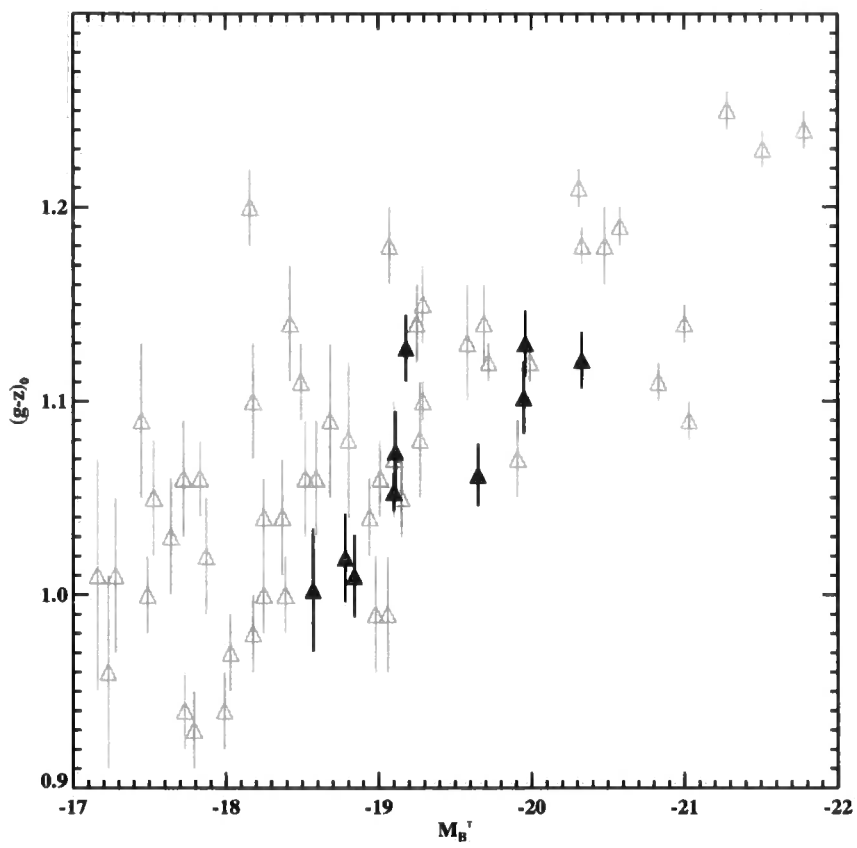

Figure 4.10: Comparison of mean colours for GCs in our galaxy sample with those from the ACS Virgo Cluster Survey (ACSVCS). Our results are plotted with a filled triangle, while ACSVCS results from PJC06 are plotted with an open triangle. The mean colours of our field galaxy sample appear to be situated at the bluer end of the colour range for a given galaxy luminosity.

the distribution of mean colours of the ACSVCS galaxies at a given host galaxy luminosity. In order to estimate the mean colour difference quantitatively, the mean GC colours of the ACSVCS in the range of the absolute magnitude of our sample ($-18.4 \geq M_B^T \geq -20.4$) were fitted by a straight line. The deviations from the fitted line for the ACSVCS and our sample were then calculated. The offset of the mean of these two deviations is $\sim$0.04 mag, and the K-S test reveals that the probability of the two samples originating from the same distribution is less than 3%.

For NGC3377 the mean colour of its GCS is in the middle of the range of mean colours of the ACSVCS, unlike other GCSs in our sample. Because the distribution of red GCs is more centrally concentrated, and NGC3377 is the nearest galaxy in our sample, it is possible that the GCs detected within our ACS field are biased to red GCs. To test whether this selection bias is big enough to shift the mean colour, we have resampled the GCs in other galaxies with a smaller field of view and recalculated their mean colours. NGC4033 and NGC1172 which have a similar absolute magnitude, but are as twice as distant as NGC3377, were chosen. The mean colour of the GCs in these two galaxies within 50″ radius from their galaxy centers is $\sim$0.03mag redder than our original estimations for the full spatial coverage. Noting that the full field of view of the ACS is 202″ $\times$ 202″ so that a circle with 50″ radius covers almost half of the original aperture, the intrinsic mean colour of GCs in NGC3377 could be about $\sim$0.03mag bluer than our original estimation. However, this is a relatively small correction compared to the wide range of mean colours seen in the ACSVCS. Note that the error bar of NGC3377 plotted in Figure 4.10 is also $\pm$0.02mag.

PJC06 have analyzed their colour distributions with two different methods. One method separates the two sub-populations in each host galaxy and tests for bimodality using the KMM routine. The other coadds the colour distributions of GCs in bins of host galaxy luminosity and separate the two sub-populations by nonparametric decomposition. We compared the former results of PJC06 with ours, because our colour distributions were also analyzed

with the KMM method and because the number of our sample galaxies is not large enough or wide enough to bin by galaxy luminosity. Figure 4.11 shows a comparison of the colour peaks of the two sub-populations between our results and PJC06. Comparison of the fractions of red populations, and total number of GCs detected, are also plotted in Figure 4.12. In Figure 4.12, only data with a bimodal colour distribution are plotted.

Overall trends for the colour distributions appear to behave similarly with host galaxy luminosity in both samples. As can be seen in Figures 4.11 and 4.12, the probability of bimodality is getting lower with decreasing host galaxy luminosity, as the red population are getting weaker. There is a strong correlation between the peak of the red sub-population and host galaxy luminosity. Furthermore, the more luminous galaxies also host more GCs.

On the other hand, some differences do also exist between these two samples. In Figure 4.11, our slope of red peak against galaxy absolute magnitude appears to be steeper than the ACSVCS by a factor of $\sim$2. In other words, the bimodal colour distributions in our sample disappear more quickly as galaxies get fainter. Moreover, we have found no correlation between the blue peaks and galaxy absolute magnitude, while PJC06 have found a weak correlation, although not as steep as for the red peaks. The red peaks of our sample appear to be slightly bluer than those of the ACSVCS by $\sim$0.04 mag although at the bright end of our sample ($M_B^T \approx -20$) there is no difference. Unlike the red peaks, the blue peak positions are almost identical with the ACSVCS, as can be seen in the left panel of Figure 4.12, It is also found that our fraction of red GCs is $\sim$10% lower than seen in the ACSVCS at given galaxy luminosity. Given that the mean colours of the GCs in our sample are slightly bluer than those of the ACSVCS, and the blue peak positions are almost identical with ACSVCS, this suggests that the difference of the mean colours is due to differences in the relative fraction of the red population as well as the red peak position. In terms of richness of the GCSs, it is tricky to compare these two different results directly because the GC selection criteria are rather different and the observation setups are not identical, even though the

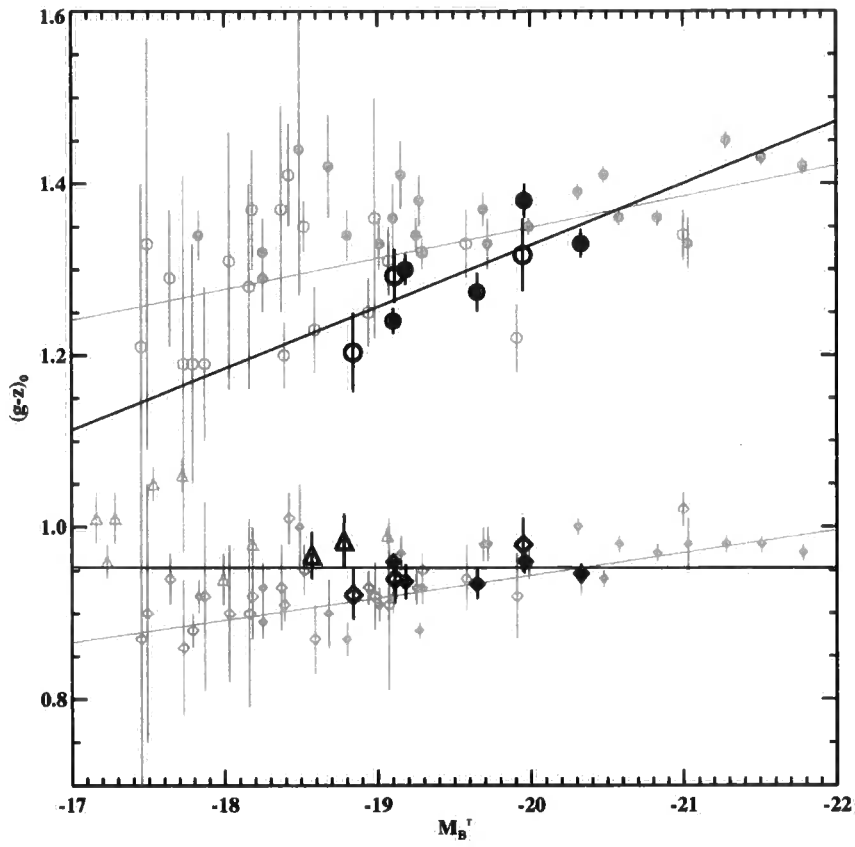

Figure 4.11: Comparison of colour peaks with the ACSVCS. Symbols are identical with Figure 4.9. Black symbols are from our results, while grey ones are from the ACSVCS. The dark sold lines are a linear fit to each subpopulation from our results, whereas the grey solid lines are linear fits by PJC06 to the ACSVCS.

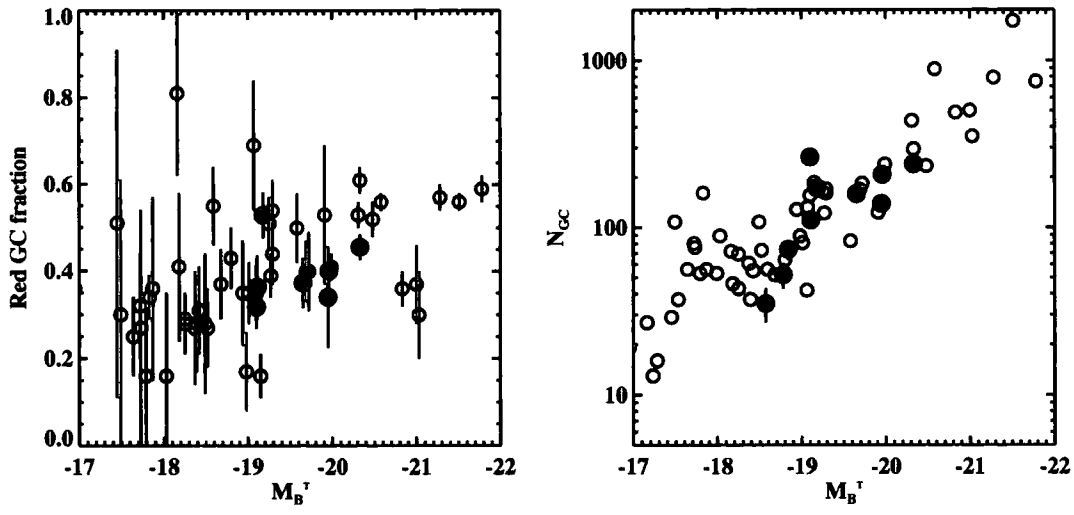

Figure 4.12: Comparison of the fraction of red GCs and total number of GCs with the ACSVCS. Filled circles are from this work, while open circles are from the ACSVCS.

right panel of Figure 4.12 shows a good agreement in the total detected number of GCs.

In terms of shapes of colour distributions, those in the ACSVCS are more varied than those in our sample. For instance, PJC06 found one single broad peak for the colour distribution in VCC1664 and VCC1619, and also found examples in which the red population dominates completely with red GC fractions of 0.84 in VCC1146 and NGC4458. These kinds of "abnormal" colour distributions are not found in our smaller field sample.

To sum up the comparison of the properties of GCSs in our sample with those of the ACSVCS, the first column of Figure 4.13 shows the GC properties against host galaxy absolute magnitude (identical with Figures 4.10, 4.11, and 4.12). The second and third columns present comparisons of GC properties against local galaxy number density (environment) and Hubble type respectively. In these two columns, only results from the ACSVCS within the range of galaxy luminosity of our sample ($-18.4 \geq M_B^T \geq -20.4$) are plotted to minimize any dependance on galaxy luminosity. In the third column, the GCSs with the same

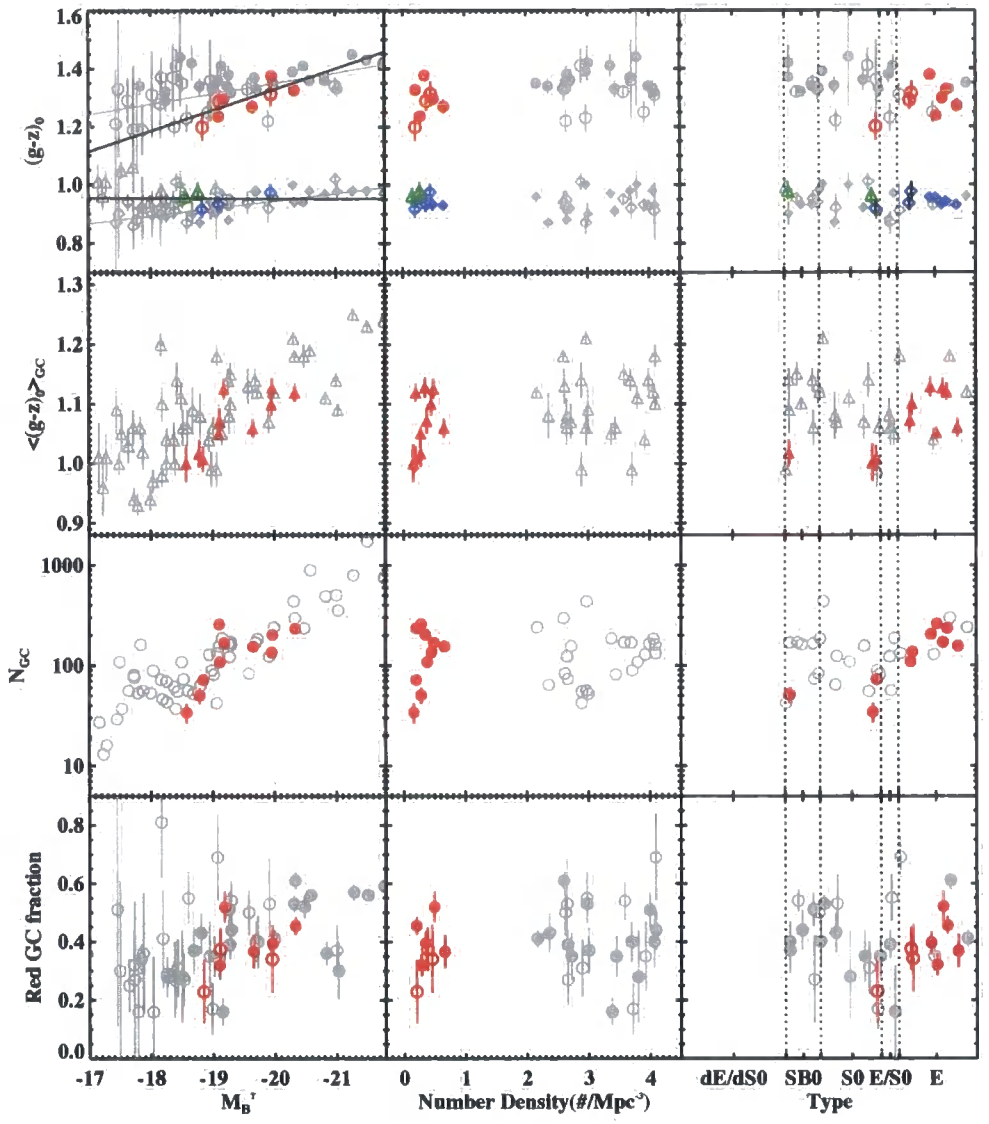

Figure 4.13: Comparison of the global properties of GCSs in our sample of low-luminosity field E/S0s with those of the ACSVCS. The columns show plots versus absolute magnitude, local number density of galaxies from Tully(1988), and morphological type of the host galaxy respectively. The rows show the colour of the blue and red peaks, mean colour, total number of detected GCs, and the fraction of red GCs. The coloured symbols represent our data, while the grey symbols are from the ACSVCS. For the second and third columns, only galaxies from the ACSVCS within the luminosity range of our sample are plotted. For the first and fourth rows, closed circles show the GCs in which colour bimodality is strongly detected using the KMM test, and open symbols show those with weak colour bimodality. In the top-left panel, black lines are the best linear fit to our data, and the grey lines to the ACSVCS data.

morphological type are randomly positioned within the morphological type bins. As can be seen in the second column, our sample is clearly discriminated from the ACSVCS in terms of galaxy environment. Because the GCS properties of both the ACSVCS and our sample are widely spread, distinct differences with galaxy number density are not obvious in these plots. In the plots of GC properties against morphological type (third column of Figure 4.13) there are some interesting findings. For the VCSACS there are no obvious trends against morphological type, but for our sample the GCSs in SB0/S0 type galaxies have little/no bimodal colour distributions. In other words, the SB0/S0 galaxies have smaller red subpopulations and fewer total numbers of GCs compared to those in E-type galaxies. The implications of our findings in this section for the role of environment in early-type galaxy formation will be discussed further in Chapter 5.

Our globular cluster luminosity functions (GCLFs) have also been compared with the results of the ACSVCS in Figure 4.14. Jordán et al. (2007b) fit the GCLF of 89 galaxies with a Gaussian function as well as a Schechter function and found that the GCLF dispersions are correlated with galaxy luminosity, whereas the GCLF turn-over magnitudes are rather constant (in both bands). We compare our results from §4.3.2 directly with the Gaussian fitting parameters of the galaxy-binned GCLFs by Jordán et al. (2007b), using distance moduli from Table 4.1 and apparent turn-over magnitudes from Table 4.6. In Figure 4.14, our results are overplotted on the fitting parameters from Jordán et al. (2007b). Our results appear to be more widely spread than the ACSVCS, however, one must keep in mind that the ACSVCS results come from galaxy-binned GCLFs, which are less noisy than individual GCLF fitting parameters. Using only our GCLF dispersions, it is hard to say whether or not there is a trend with galaxy luminosity because of the narrower range of galaxy luminosity in our sample. Our GCLF dispersions agree well with the ACSVCS, at least within the range of our galaxy luminosities.

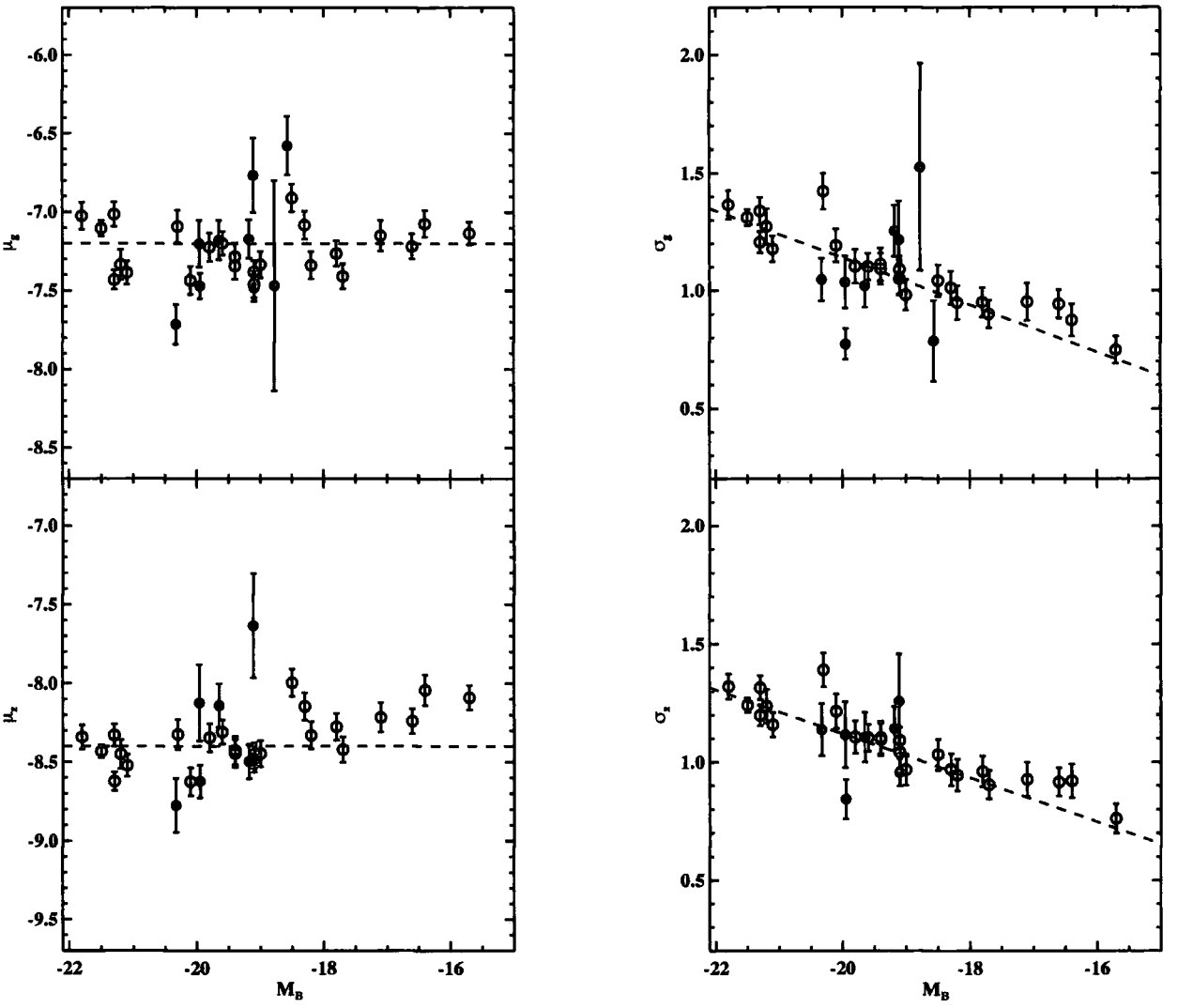

(a) (b)

Figure 4.14: Gaussian fit parameters of luminosity functions against host galaxy luminosity. Graph (a) plots turn-over magnitudes in g and z bands against galaxy luminosity, and (b) plots dispersions of luminosity functions against galaxy luminosity. The open circles represent the Gaussian fits to galaxy-binned GCLFs from the ACSVCS by Jordán et al. (2007b), whereas the results from this work are plotted with filled circles.

4.4 Conclusions

- High spatial resolution images of ten low-luminosity early-type galaxies in low density (field) environments have been obtained using the HST/ACS in the F457W and F850LP bands. We have investigated the properties of the globular cluster systems (GCSs) associated with these galaxies and also the connection with the host galaxy properties. We have then compared our results with those of the ACS Virgo Cluster Survey (ACSVCS) to study the role of environment in galaxy formation.

- The GCS properties of our low-density sample show similar trends against host galaxy luminosity to those in clustered environments. There are more GCs in total and more red GCs in luminous galaxies, whilst the mean colour and the colour of the red peak GCs are strongly correlated with host galaxy luminosity. Colour bimodality becomes less clear with deceasing galaxy luminosity.

- The mean colours and colours of the red peaks in low-density (field) regions appear to be $\sim$0.04 mag bluer than those around galaxies of equivalent luminosities in high-density regions, while the colour of the blue peaks remains constant. The fraction of red GCs in field galaxies is found to be $\sim$10% lower than that in clustered galaxies of similar luminosities. Colour bimodality disappears more quickly as galaxies get fainter, compared to the trend observed in the ACSVCS.

- Luminosity functions of GCs in most of our sample galaxies are well fit by a Gaussian function whose fitting parameters (turn-over magnitude and dispersion) agree well with those of the ACSVCS, even though we found no independent evidence for a trend of dispersion of the fitted Gaussian luminosity functions against galaxy luminosity.

Chapter 5

Discussion and Conclusions

5.1 Effect of horizontal branch stars on integrated spectra of stellar systems

Whether or not horizontal branch (HB) stars have a significant effect on the integrated light of GCs is an important, but not well understood, issue in stellar population synthesis models (e.g. Maraston & Thomas 2000; Lee et al. 2000; Lee et al. 2002). From our database of line indices we have investigated whether there is any systematic dependance of Balmer line strength on HB morphology. In Figure 5.1 three Balmer line indices are plotted against metallicity with 10 and 12 Gyr simple stellar population models from Lee & Worthey (2005) superimposed. The reason the two models cross each other is the effect of blue HB stars on the integrated spectra (see more detail in Lee et al. (2000)). Without HB stars the line strength of the 12 Gyr model would be weaker than the 10 Gyr model at all metallicities. Our data for the Balmer lines appears to lie comfortably between the 10 and 12 Gyr models.

We have selected GCs with the same metallicity but different HB morphology (minimum

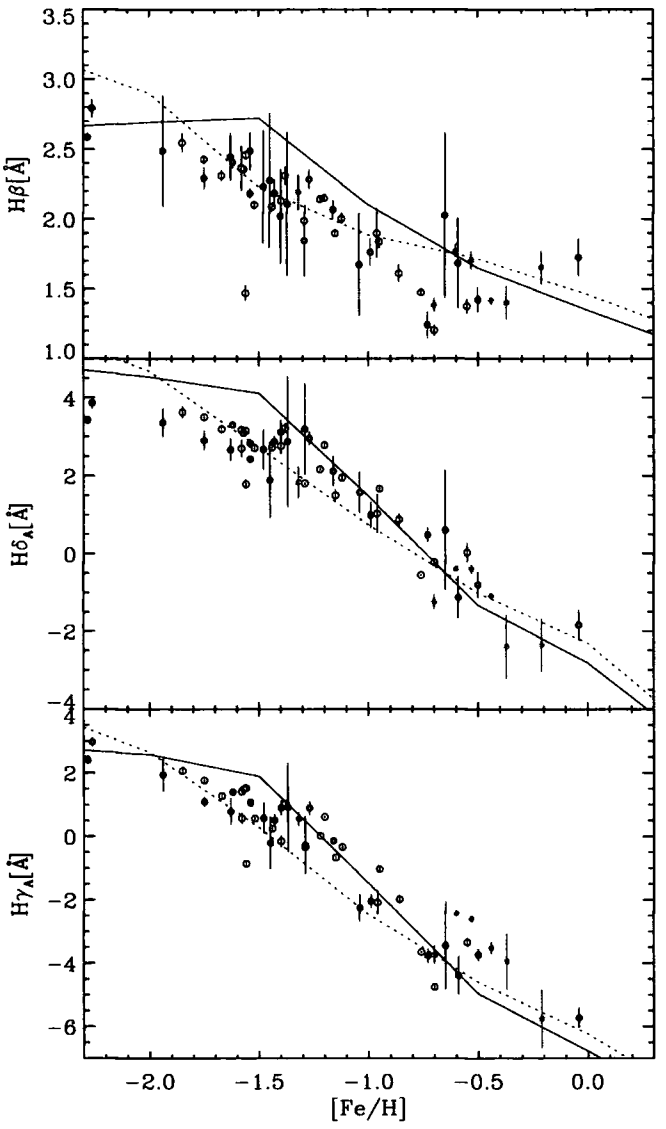

Figure 5.1: Strength of Balmer lines against metallicity of the Galactic GCs. Metallicities [Fe/H] are taken from Harris (1996). Symbols are identical with Figure 2.2. The overplotted lines are simple stellar population models from Lee & Worthey (2005) with ages of 10 Gyr (dotted line) and 12 Gyr (solid line) and an alpha element abundance of $[\alpha/\mathrm{Fe}]=+0.3$.

Table 5.1: Galactic globular clusters pairs with the same metallicity but a different HB morphology. [Fe/H] and HBR values are taken from Harris (1996). Their three Balmer line indices and references are listed.

Globular cluster	[Fe/H]	HBR	Data ref.	Hβ[Å]	Hδ_A[Å]	Hγ_A[Å]
NGC7006	-1.63	-0.28	This work	2.45±0.17	2.67±0.29	0.78±0.41
NGC7089 (M2)	-1.62	0.96	This work	2.41±0.04	3.31±0.05	1.40±0.11
NGC3201	-1.58	0.08	SRC05	2.36±0.16	2.70±0.22	0.57±0.17
NGC5986	-1.58	0.97	SRC05	2.37±0.03	3.18±0.04	1.41±0.04
NGC6934	-1.54	0.25	This work	2.49±0.13	2.83±0.11	1.06±0.11
NGC6205 (M13)	-1.54	0.97	This work	2.18±0.03	2.43±0.07	1.08±0.05
NGC6981 (M72)	-1.40	0.14	This work	2.02±0.34	3.12±0.30	0.90±0.23
NGC6229	-1.43	0.24	This work	2.18±0.10	2.87±0.14	0.50±0.19
NGC6235	-1.40	0.89	SRC05	2.13±0.10	2.76±0.20	-0.16±0.18
NGC6266 (M62)	-1.29	0.32	SRC05	1.99±0.02	1.81±0.03	-0.34±0.03
NGC6717	-1.29	0.98	This work	1.85±0.26	3.20±1.16	-0.28±0.92
NGC2808	-1.15	-0.49	SRC05	1.90±0.02	1.50±0.15	-0.67±0.03
NGC6723	-1.12	-0.08	SRC05	2.01± 0.04	1.95±0.07	-0.34±0.06
NGC6652	-0.96	-1.00	SRC05	1.90±0.17	1.03±0.50	-2.08±0.37
NGC6638	-0.99	-0.30	This work	1.76±0.97	1.00±0.34	-2.04±0.23

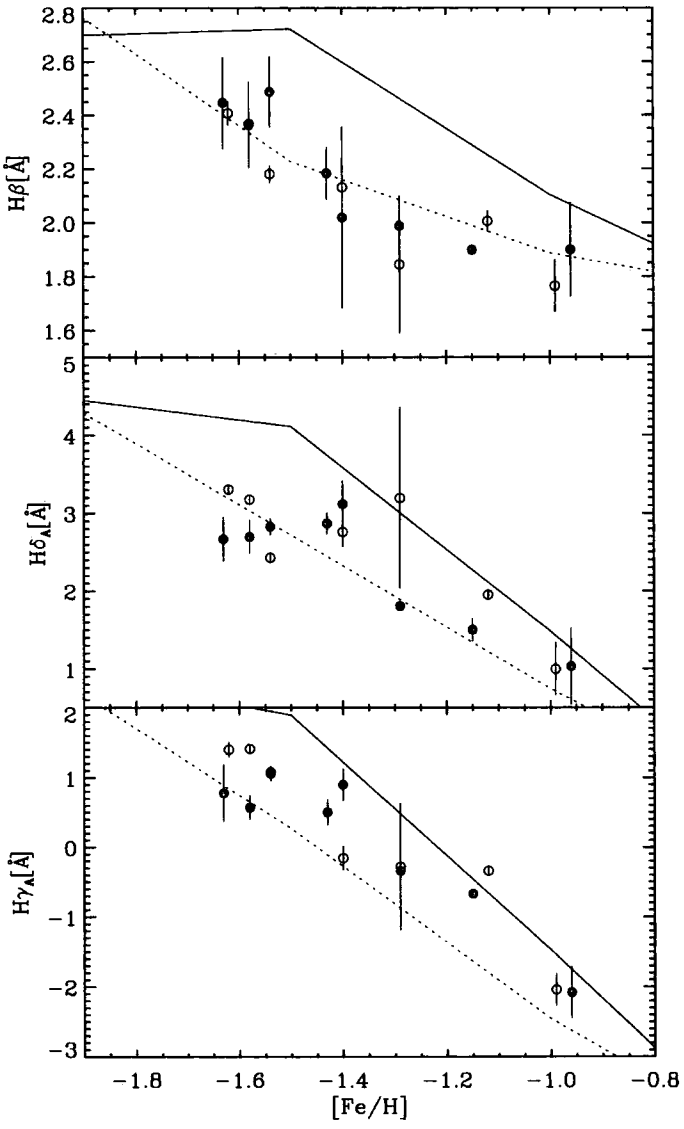

Figure 5.2: Balmer line strengths of the sample from Table 5.1. The filled circles represent GCs dominated by relatively red HB stars, while the open circles are GCs dominated by relatively blue HB stars. The model lines are the same as in Figure 5.1.

difference of 0.7 in HBR [1]) to see the explicit effect of HB stars on integrated spectra. Seven pairs or triplets of GCs have been selected with various metallicities but where the metallicities are nearly identical within a given set (Table 5.1). These sets are plotted in Figure 5.2. One might expect that GCs with more blue HB stars (*open circles* in Figure 5.2) have stronger Balmer lines than those with fewer blue HB stars (*closed circles*). However, some sets of indices with a large uncertainty do not follow this expectation. Sets of GCs, in which relatively blue HB dominant GCs have stronger Balmer lines with a high S/N, are those with the two lowest (NGC7006 and NGC7089; NGC3201 and NGC5986) and the second highest metallicity (NGC6723 and NGC2808).

From our spectroscopic data alone, it is hard to determine whether the stronger Balmer lines are due to blue HB stars or because simply they are younger (with minimal effects due to HB stars). To distinguish these two possibilities, independent estimation of the age of these GCs are required. We adopt relative ages measured by De Angeli et al. (2005) who used a method based on the magnitude difference between the HB and the main sequence turnoff point. This difference is then compared with theoretical isochrones of Cassisi et al. (2004) to determine relative ages of Galactic GCs. There are two sets of GCs that have both age measurements available: 0.77±0.04[2] and 0.91±0.05 for NGC3201 and NGC5986; 0.77±0.08 and 0.96±0.11 for NGC2808 and NGC6723 respectively. De Angeli et al. (2005) estimated differences of the normalized age depending on models to be at the level of ~5%-8%. In both cases, the GCs with stronger Balmer lines are older than those with weaker lines. This is in contradiction to the fact that stars near the main-sequence turnoff are a major source of Balmer lines so that the Balmer line strength should decrease with increasing age of GCs.

[1]The HBR index is defined as $HBR \equiv (B-R)/(B+V+R)$ by Lee et al. (1994), where B and R are the number of stars bluer and redder than the instability strip respectively, and V is the number of RR Lyrae stars

[2]This is a normalized age, defined as the ratio between the GC age and the mean age of the group of metal-poor clusters i.e. a normalized age of 1.0 corresponds to 11.2 Gyr.

Therefore, an additional source of hot stars that boost the Balmer lines is required. Our results suggest that GCs with bluer HB type have stronger Balmer lines in spite of older ages, which implies that hot HB stars are a substantial contribution to the Balmer liine strength and can make a GC look younger in ages derived from integrated light.

5.2 Globular Cluster Luminosity Functions (GCLFs) of NGC474 and NGC3377

As can be seen in Figure 3.13 and Figure 4.7, there is an excess of faint GCs around $V \sim 25.5mag$ in the GCLF of NGC474 and $g \sim 25.5mag$ in NGC3377, deviating significantly from the fitted Gaussian function. We investigate in more detail below the properties of these objects.

In Figure 5.3, the spatial distribution, size and colour of NGC3377 GCs fainter than $g = 25mag$ are plotted along with those brighter than $g = 25mag$. In the top-left panel, the faint GCs (large closed circles) appear to be distributed uniformly, unlike bright GCs (small open circles) which are concentrated to the galaxy center. The top-right panel shows histograms of FWHM returned by *Sextractor* for the faint and bright GCs. The distribution of sizes of the faint GCs is also quite different from those of the bright GCs, in the sense that they are either smaller or larger than the medium size for all clusters. The colour distribution of the faint GCs appears to be rather flat as shown in the bottom-left panel. We have looked for any colour dependence of the size of the faint GCs by separating the GCs at $FWHM = 2.8$ pixels. In the bottom-right panel, the thin histogram is the colour distribution of faint GCs with $FWHM > 2.8$, while the thick histogram is for GCs with $FWHM < 2.8$. There is no obvious correlation between the sizes and colours found in this plot.

We can speculate on the possibilities of the origin of these faint objects that deviate

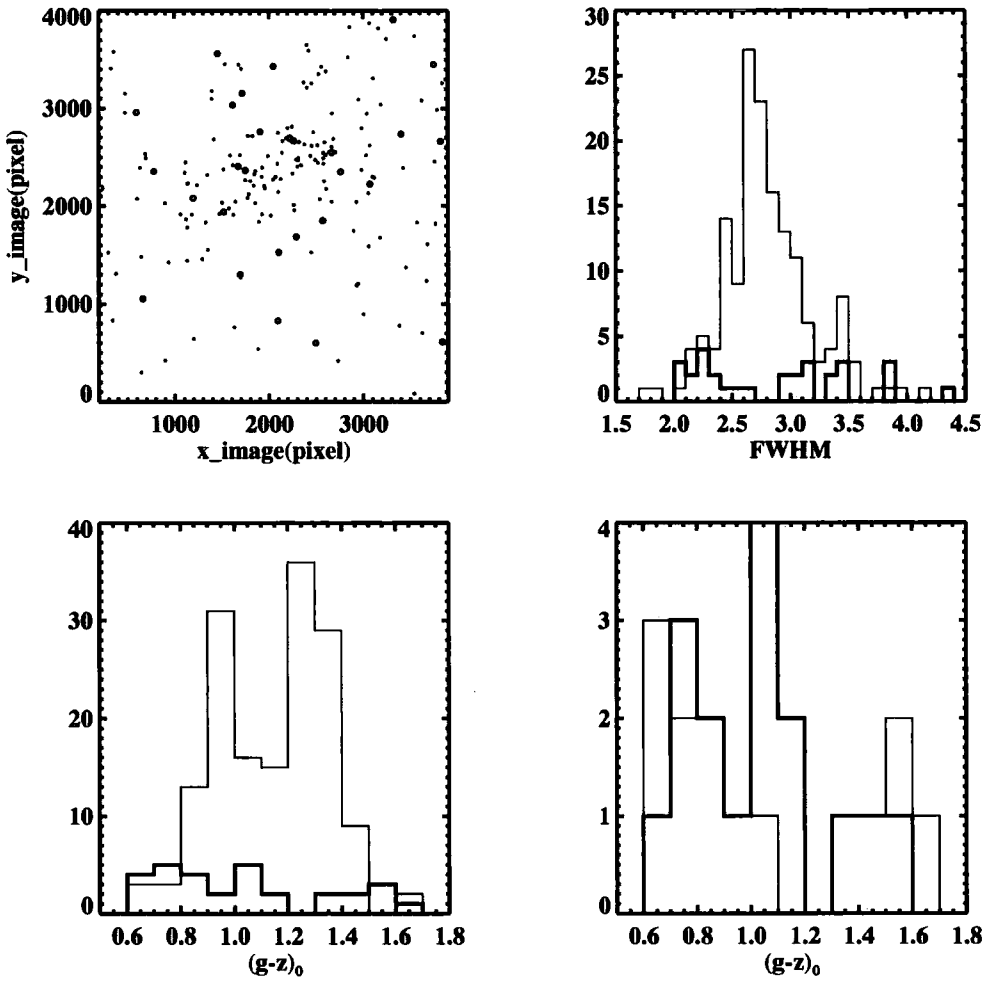

Figure 5.3: Properties of faint GCs near g$\sim$25.5 mag in NGC3377. The top-left panel shows the spatial distribution of bright GCs (g<25 mag, small open circles) and faint GCs (g>25 mag, large closed circles). The top-right panel shows the histograms of FWHM of the bright (thin histogram) and faint (thick histogram) GCs. The bottom-left panel shows colour distributions of the bright (thin histogram) and faint (thick histogram) GCs. The bottom-right panel shows colour distributions of the faint GCs with larger FWHM>2.8 (thin histogram) and smaller FWHM<2.8 (thick histogram).

from the normal Gaussian GCLF. Peng et al. (2006b) found a class of 'diffuse' star clusters (DSCs) in the ACSVCS and investigated the nature of these objects, which are characterized by low luminosity, a broad distribution of sizes, low surface brightness, and redder colour than normal metal-rich GCs. Their spatial distribution was also closely associated with the host galaxy light. Not all of these characteristics are found in our faint objects, however, which have a wide distribution of sizes but with significant number of blue GCs and a random spatial distribution.

Another possibility is that they may be field stars (bright giant) that belong to the parent galaxy. By comparing with isochrones having various ages and metallicities (Girardi 2006), the locus of giant stars ($M_v < -5$) with very young age ($\sim$10 Myr) overlaps that of the faint objects on the colour-magnitude diagram (Figure 4.4). It is however very unlikely that such young stars exist in large elliptical galaxies like NGC3377 in significant numbers, and horizontal branch stars are not luminous enough to account for these objects. Furthermore, Harris et al. (2007) found no evidence of young stellar populations (<3 Gyr) in the halo star C-M diagram of NGC3377 from deep HST/ACS photometry, although their field of view barely overlaps ours. The number density of foreground Milky Way stars in the direction to NGC3377 is also very low ($N_{star} < 10$) within the ACS field (Robin et al. 2003) and even lower in the magnitude range of the faint GCs. Visual inspection of these faint objects reveals that some are more likely to be misclassified background galaxies.

In Figure 5.4, the spatial distribution, size and colour of NGC474 GCs fainter than $V = 25$ mag are plotted along with those brighter than $V = 25$ mag. In the top-left panel, the faint GCs (large closed circles) appear to be concentrated to the galaxy center around (x,y)=(2000pixel, 2500pixel) like the bright GCs (small open circles). The top-right panel shows histograms of FWHM returned by *Sextractor* for the faint and bright GCs. The sizes of the faint GCs seem to be systematically larger than those of the bright GCs. The colour distributions of the two GCs samples also appear to be similar as shown in the bottom-left

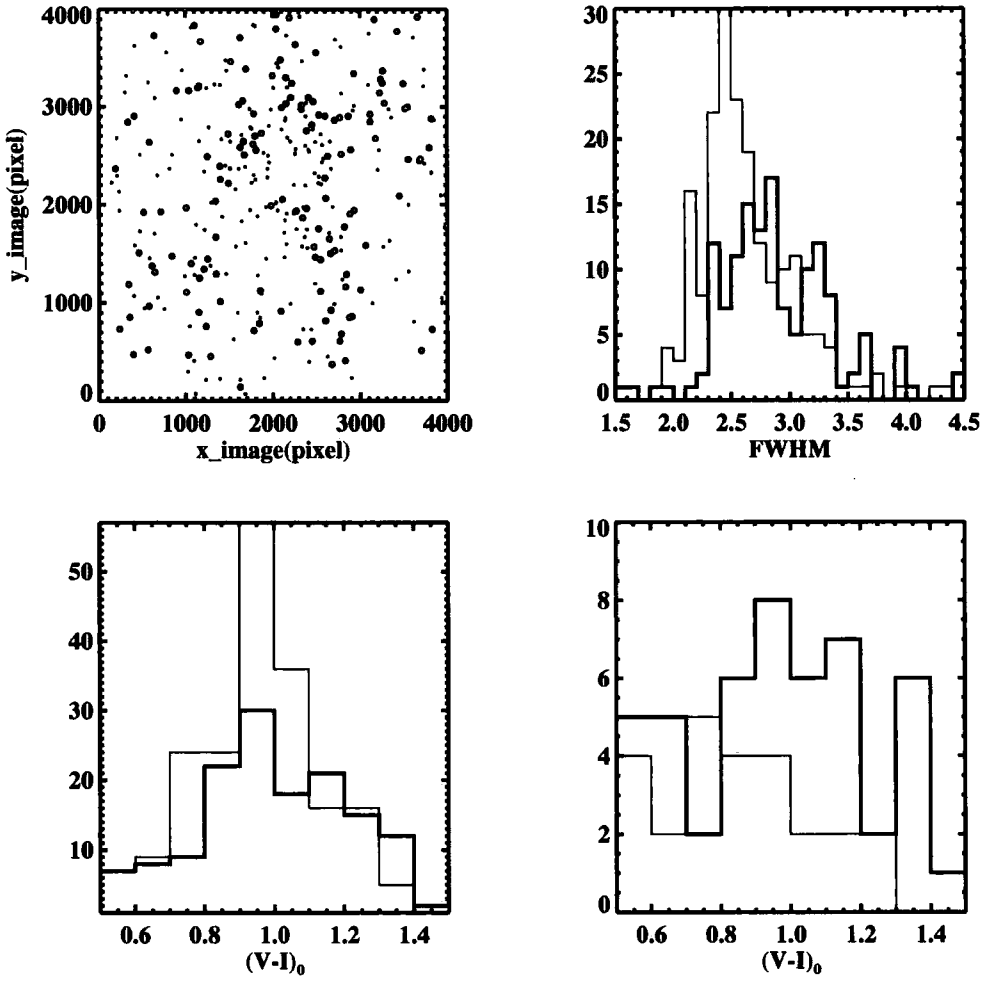

Figure 5.4: Properties of faint GCs near V$\sim$25.5 mag in NGC474. The top-left panel shows the spatial distribution of bright GCs (V<25.25 mag, small open circles) and faint GCs (V>25.25 mag, large closed circles). The top-right panel shows the histograms of FWHM of the bright (thin histogram) and faint (thick histogram) GCs. The bottom-left panel shows colour distributions of the bright (thin histogram) and faint (thick histogram) GCs. The bottom-right panel shows colour distributions of bright (thin histogram) and faint (thick histogram) GCs with FWHM$\geq$3.1.

panel. In the bottom-right panel, the faint GCs with FWHM≥3.1 appear to be slightly redder than the bright GCs with FWHM≥3.1. Unlike the faint GCs in NGC3377, which are 2.5 mag fainter than its turn-over magnitude, those in NGC474 are only 0.8 mag fainter than its turn-over magnitude. This makes any features of 'abnormal' faint GCs, if there are any, less distinguishable from other GCs. Most of these faint GCs are thought to be genuine GCs. However, some faint GCs could presumably be background galaxy contaminations as they are slightly more extended and redder than normal bright GCs.

5.3 Effect of environment on galaxy formation

Our results have shown that the mean colours of GCSs in field environments are slightly bluer than those in cluster environments at a given host galaxy luminosity. The simplest interpretation would be that they are either less metal-rich or younger than their counterparts in rich clusters (or both metal-poor and young). We have adopted simple stellar population models from Girardi (2006) to estimate the magnitude of these effects and compare them with our mean colours. The models contain a metallicity range of $0.0001 \leq Z \leq 0.030$ and an age range of $6.30 \leq log(t/yr) \leq 10.25$ with a Kroupa (2001) initial mass function (IMF). Figure 5.5 shows the prediction of $(g-z)_0$ colour in various age and metallicity ranges based on the Girardi (2006) models. We first assume that the blue and red subpopulations are coeval so that the colours purely depend on metallicity. The metallicity range of each subpopulation is shown with a shaded area in Figure 5.5. Assuming an age of 11.2 Gyr, which is typical of the age of metal-poor Galactic globular clusters (e.g. Salaris & Weiss 2002; De Angeli et al. 2005), we estimate a metallicity range of $-1.89 \leq [Fe/H] \leq -1.59$ for the blue subpopulations and $-0.86 \leq [Fe/H] \leq -0.42$ for the red subpopulations. These ranges of the two metallicity peaks agree well with previous studies (Figure 5.9).

With only one colour $(g-z)$ it is almost impossible to break the well known age-metallicity

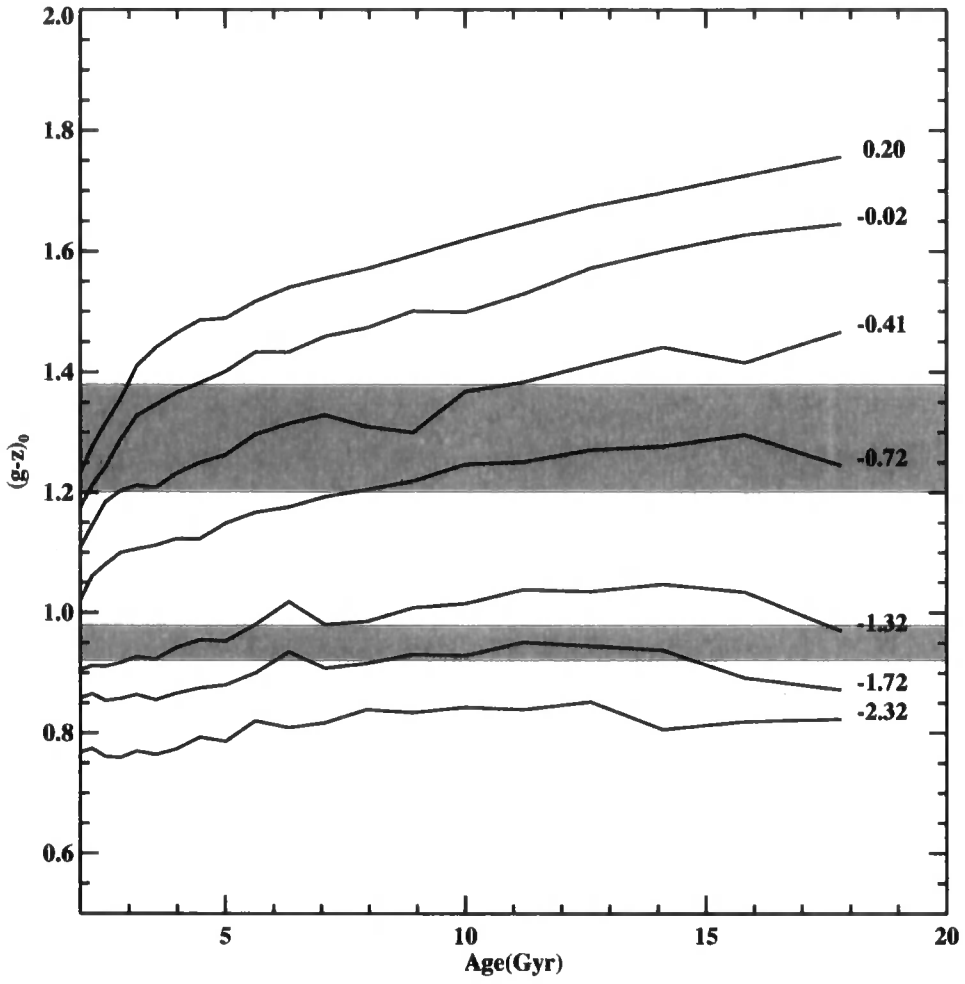

Figure 5.5: Evolution of g-z colour for various metallicities and ages. The tracks are taken from simple stellar population models by Girardi (2006). The metallicity noted at the end of each track is in units of [Fe/H]. The two stripes represent the colour ranges of red and blue peaks of GCSs in our sample galaxies. This graph shows that for old stellar populations >8 Gyr, $(g-z)_0$ colour is mainly governed by metallicity rather than age, except for the most metal-rich subpopulations.

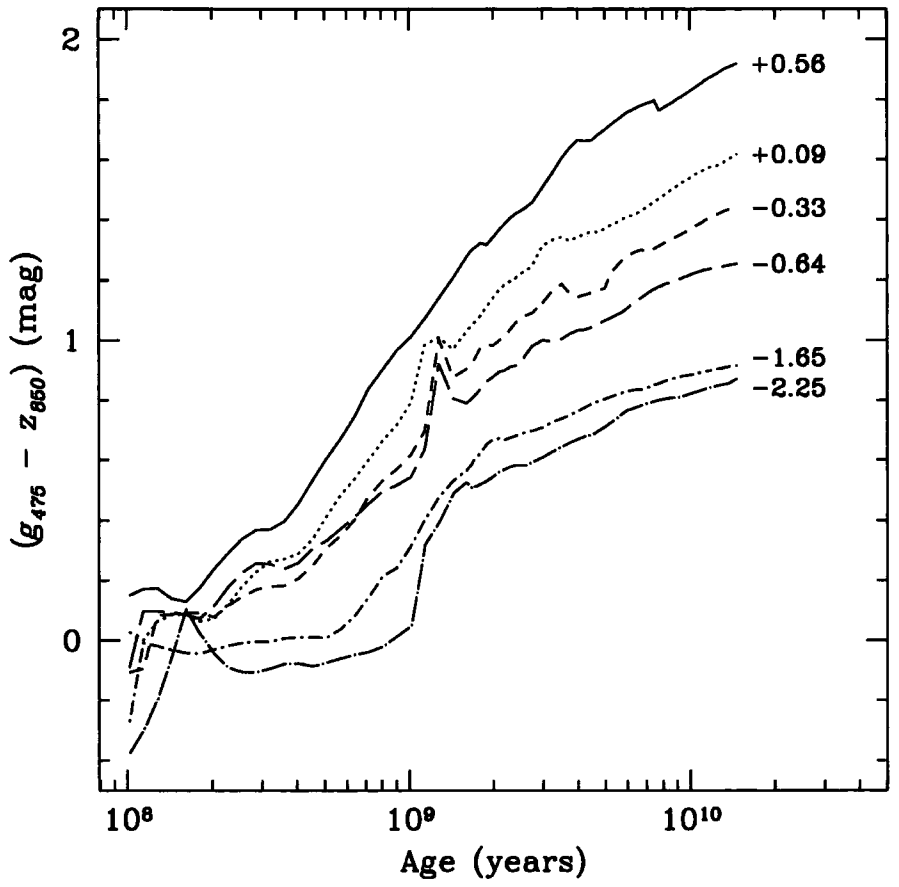

Figure 5.6: Evolution of g-z colour with age from Côté et al. (2004). The tracks are based on simple stellar population models from Bruzual & Charlot (2003). The numbers next to each track indicate metallicity in [Fe/H]. Note that there are systematic differences in the predicted colours compared with tracks from Girardi (2006) shown in Figure 5.5, especially at low metallicities.

degeneracy. Thus, we make an assumption that in these cases, the mean ages of GCSs in low and high density regions are nearly coeval and have <2 Gyr age difference (Thomas et al. 2005). Metallicity offsets were then calculated from the colour offset of $\sim$ 0.05 in the mean colour between the low and high density regions using the SSP model from Girardi (2006) for the range of mean colours from our sample. Figure 5.7 shows the metallicity differences ($\Delta[Fe/H] = [Fe/H]_{cluster} - [Fe/H]_{field}$) against the mean colour of GCSs in the field galaxies for various age combinations (coeval, 11 and 9 Gyr, and 10 and 8 Gyr for cluster and field galaxies respectively). The metallicity of GCSs in low-density environments appears lower by $\sim$0.2-0.15 dex than that in high-density regions assuming they are coeval. This metallicity offset is reduced to $\sim$0.05 dex if GCSs in field galaxies are $\sim$2 Gyr younger than those in clusters. However, this small metallicity offset ($\sim$0.05) could easily disappear entirely if we take into account photometric uncertainties, systematic differences between SSP models (Figure 5.6), and slightly different age offsets. We tentatively conclude that GCSs in low-density environments are either less metal-rich with the same age or slightly less metal-rich (probably same metallicity) with younger ages than those in high-density regions.

There have been a few previous attempts to detect differences in GC properties depending on the environments to which their host galaxies belong. Gebhardt & Kissler-Patig (1999) used 50 mostly early-type galaxies from the HST/WFPC2 archive and found no correlation between the colour peaks and host galaxy properties in 15 field sample galaxies, whereas they found a strong correlation of GCS peak colours versus galaxy velocity dispersion and Mg_2 index in their cluster galaxy sample. Our field galaxy results certainly show a strong relation between the mean colour versus galaxy luminosity (see Figure 4.9). One reason that Gebhardt & Kissler-Patig (1999) could not find any such relation in their field galaxy sample could be that their galaxies are too luminous ($M_V \lesssim -20$), because only small differences are expected for luminous ($M_B \lesssim -21$) early-type galaxies (see Figure 5.8). Alternatively

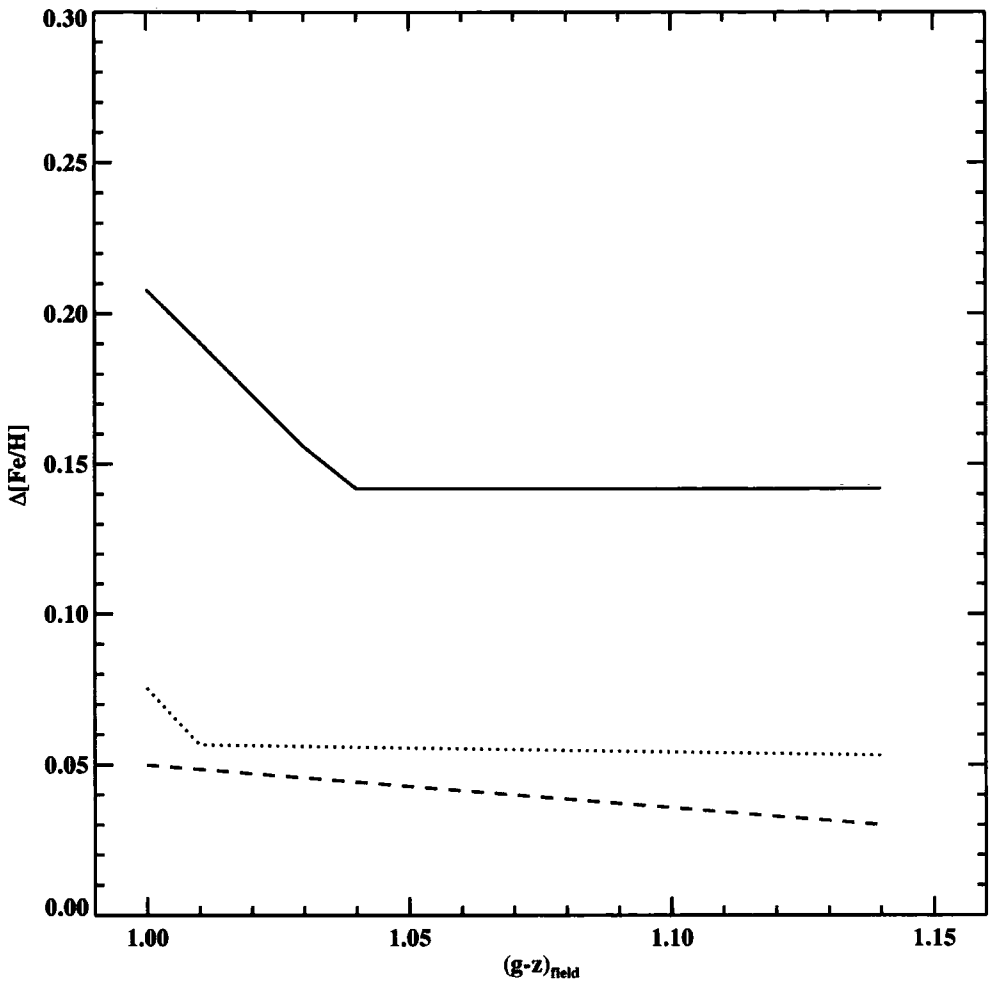

Figure 5.7: Metallcity differences of GCs between in dense and loose environments. The x-axis indicates the mean colour of GCs in the field galaxies. These metallcity offsets were derived from the SSP model by Girardi (2006) assuming that the mean colours of GCs in cluster galaxies are 0.05 mag redder than those in field and the ages of GCs in cluster and field galaxies are same(11 Gyr, solid line), 11 and 9 Gyr (dotted line), and 10 and 8 Gyr (dashed line) respectively.

it could be that the photometric accuracy of the HST/WFPC2 data was not good enough to detect this correlation (see the comparison of performance between ACS and WFPC2 in §3.2.6). In fact there are two common field galaxies between this work and Gebhardt & Kissler-Patig (1999) (NGC1426 and NGC3377). We detect twice as many GCs in these two galaxies compared to Gebhardt & Kissler-Patig (1999). Larsen et al. (2001) also briefly investigated the dependancy of colour bimodality on environment in an independent sample of 17 early-type galaxies obtained from HST/WFPC2, but did not find any correlation. As can be seen from our results, the colour bimodality of GCSs mainly depends on galaxy luminosity (mass), although this trend disappears at a slightly higher galaxy luminosity in low density regions.

Peng et al. (2008) found a large spread in the specific frequencies (S_N) of dwarf galaxies from the ACSVCS. Almost all dwarfs with a high S_N are located within a projected radius of 1 Mpc from M87 (Figure 4 in Peng et al. (2008)), whereas no difference of S_N between the central region and the outskirts of the Virgo cluster was found for intermediate luminosity galaxies (similar to those in our low density sample). Even though Peng et al. (2008) found a dependency of S_N for the dwarfs with environment, the cumulative GC colour distributions of these two groups show no obvious difference. It is possible that the environmental effect on the color distribution is so subtle that it could not be detected within a cluster environment like Virgo.

Regarding the environmental dependance of galaxy formation generally, many studies have been conducted both observationally and theoretically without including constraints from GCS data. It is now well established that late-type galaxies are biased to low-density environments and giant elliptical galaxies are preferentially located in galaxy clusters (Dressler 1980). Cluster galaxies also had lower star formation rates than field galaxies at a given redshift, luminosity, and bulge-to-disk ratio (Balogh et al. 1998; Lewis et al. 2002; Gómez et al. 2003). Early-type galaxies in low density environments also appear to be younger

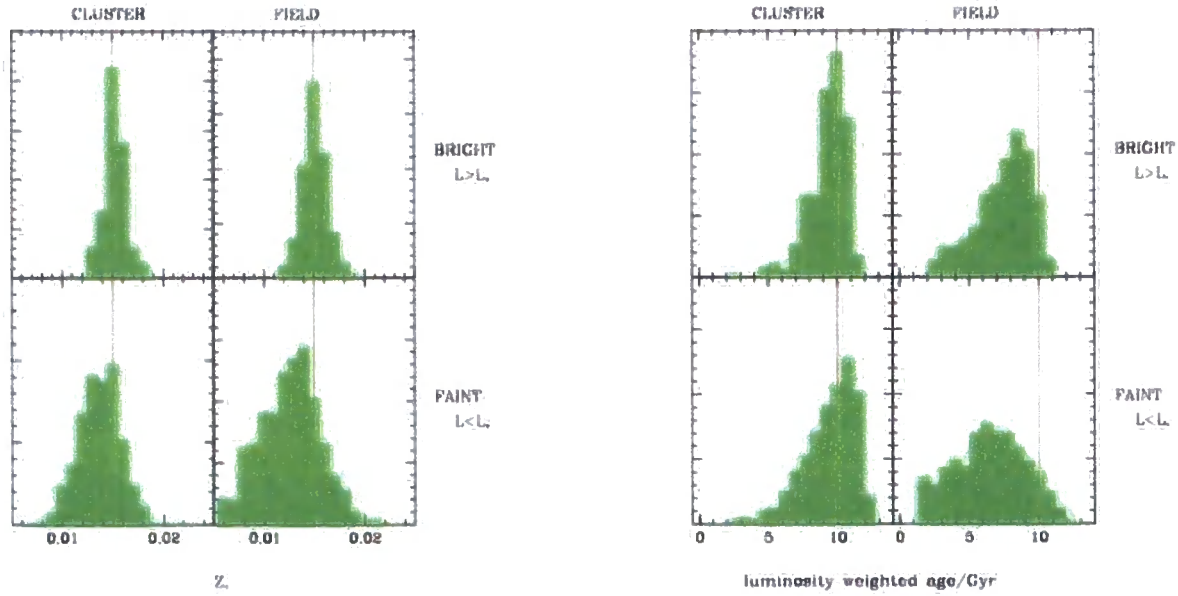

Figure 5.8: Metallicity and mean age distributions of galaxies from a semianalytic model (Baugh et al. 1996 and Cole et al. (2000)) of galaxy formation in a hierarchical CDM universe. Whilst bright galaxies in both clusters and the field show remarkably uniform properties, low luminosity galaxies ($L < L_*$, where L_* is the characteristic luminosity of a Schechter luminosity function corresponding to $M_B \approx -21$) show a large spread in both metallicities and ages. Field galaxies also have lower metallcity and younger age on average than cluster galaxies.

($\Delta t \sim 2$ Gyr) and more metal-rich ($\Delta[Fe/H] \sim 0.1$ dex) compared with their counterparts in dense environments (Kuntschner et al. 2002; Thomas et al. 2005), although Clemens et al. (2006) found no environmental influence on metallicity (but still found younger ages for field galaxies). These observational findings are contradictory to the semi-analytic model of hierarchical galaxy formation (e.g. Baugh et al. 1996; Cole et al. 2000) which predict a larger spread of age and metallicity, and younger ages and lower metallicities on average, in low-density environments, especially in low-luminosity early-type galaxies (see Figure 5.8).

Our results for the GCSs are somewhat inconsistent with those of Kuntschner et al. (2002) and Thomas et al. (2005) who find higher metallicities for galaxies in field environments (consistent with the semi-analytic model (Figure 5.8)). Is globular cluster formation history then different from field star formation history or does environment have different effects on globular cluster and field star formation? Harris & Harris (2002) have suggested that globular clusters formed somewhat earlier than most field stars based on their finding of higher S_N at low metallicity in NGC5128. This argument is also supported by Peng et al. (2008), who estimated globular cluster formation rates from the Millennium Simulation (Springel et al. 2005) and showed that cluster formation peaks earlier than field star formation, thus explaining why GCs are more metal-poor than field stars in early-type dwarf galaxies. Also the higher S_N of dwarf ellipticals in the Virgo cluster center was successfully explained by the higher peak star formation rate (SFR) and star formation surface density (Σ_{SFR}) in the cluster central region compared to the outskirts and a model where GC formation rate $CFR \propto SFR(\Sigma_{SFR})^{0.8}$.

As we described in §4.3.4, the colour of GCSs is mainly determined by the mass of the host galaxy in both cluster and field environments, and there are subtle environmental differences in that the mean metallicity of GCSs in field galaxies are slightly lower than those in cluster galaxies at a given host galaxy luminosity (mass), while the fraction of red clusters is higher in dense environments. From our findings, we suggest that GCS in field

galaxies form later than those in cluster galaxies and/or have a lower metallicity, and possibly form with lower cluster formation efficiency. Moreover, we expect in dense environments that cluster formation history is complicated by disturbing or interacting neighbour galaxies which is reflected in the more varied shapes of colour distributions that are found in dense environments. Even though Peng et al. (2008) found no difference of S_N in the low-luminosity ellipticals (intermediate luminosity in their term) of their Virgo cluster sample, it would be worth comparing S_N for our sample with the ACSVCS in the future.

5.4 Metal-poor GCs - galaxy luminosity relation

Whether a correlation between the peak of the blue GC colours and host galaxy luminosity exists or not can have implications for different galaxy formation scenarios. Major merger (Ashman & Zepf, 1992) and accretion models (Côté et al., 1998) would have difficulty explaining this correlation because, in the merger model, metal-poor GCs in two lower equal mass spiral galaxies are still a primary resource of metal-poor GCs in the final ellipticals. In the accretion model metal-poor GCs come from dwarf galaxies, so that the mean metallicities of GCs in dwarf galaxies and metal-poor GCs in ellipticals are more or less the same. Many early studies found a strong correlation between the colours of metal-rich GCs and host galaxy luminosity, but failed to detect any evidence of a similar correlation in the mean colours of the metal-poor GCs (e.g. Forbes et al. 1997; Kundu & Whitmore 2001a; Forbes & Forte 2001). However, Larsen et al. (2001) found a weak correlation between the mean colours of metal-poor GCs and galaxy absolute magnitude in their HST/WFPC2 sample. Burgarella et al. (2001) also suggest that such relation might exist, and Lotz et al. (2004) found that the slope of the GC peak of their dwarf ellipticals sample ($M_B \geq -18$) against galaxy luminosity is consistent with that of the GC blue peak in early-type galaxies found by Larsen et al. (2001).

Recent studies on the correlation between the metal-poor GCs and host galaxy luminosity have been carried out by Strader et al. (2006) and Peng et al. (2006a). The former compiled blue GC peak data in early-type galaxies, as well as local spirals, from various sources (Larsen et al. 2001; Kundu & Whitmore 2001a,2001b; Harris 1996; Barmby et al. 2000; Olsen et al. 2004) and found a significant ($> 5\sigma$) correlation of blue colour peak against galaxy luminosity. Peng et al. (2006a) also detect this blue peak trend in the homogenous ACSVCS data, but not as strong as that for the red peak. Using their own relation between $g - z$ colour and [Fe/H], the slope of the blue peak metallicity - galaxy luminosity relation is even steeper than that in the colour-galaxy luminosity plane due to the steeper colour-metallicity relation in the metal poor region (see Figure 12 in Peng et al. (2006a)). However, Peng et al. (2006a) note that this blue slope varies depending on the adopted colour-metallicity relation (simple stellar population model or empirical transformation) by a factor of $\sim$3.

Figure 5.9 from Brodie & Strader (2006) shows the peak metallicities of GC subpopulations against galaxy luminosity, in which the peak positions are taken from Strader et al. (2004) and Strader et al. (2006). In this plot the peak metallicity of both metal-poor and metal-rich GCs appears to be correlated with host galaxy luminosity with even a similar slope. This metal-poor GC trend can be accounted for with the *in-situ* scenario (Forbes et al., 1997), in which metal-poor GCs formed in the Universe first and after sudden truncation (possibly by reionization) the metal-rich GCs formed along with the bulk of the field stars in galaxies. Strader et al. (2005) also proposed a new GC formation scenario that combines *in-situ* and accretion models with hierarchical merging.

From our results on the blue peak colours alone, it is not clear whether or not the blue peak colours are correlated with the host galaxy luminosity because of the narrow galaxy luminosity range in our sample (only $\sim$2 mag range in M_B compared to the range of $\sim$6 mag in the ACSVCS). In order to see any trend of blue peak colour with galaxy luminosity we would need to study GCSs in fainter galaxies ($M_B \geq -18$ i.e. dwarf ellipticals) in

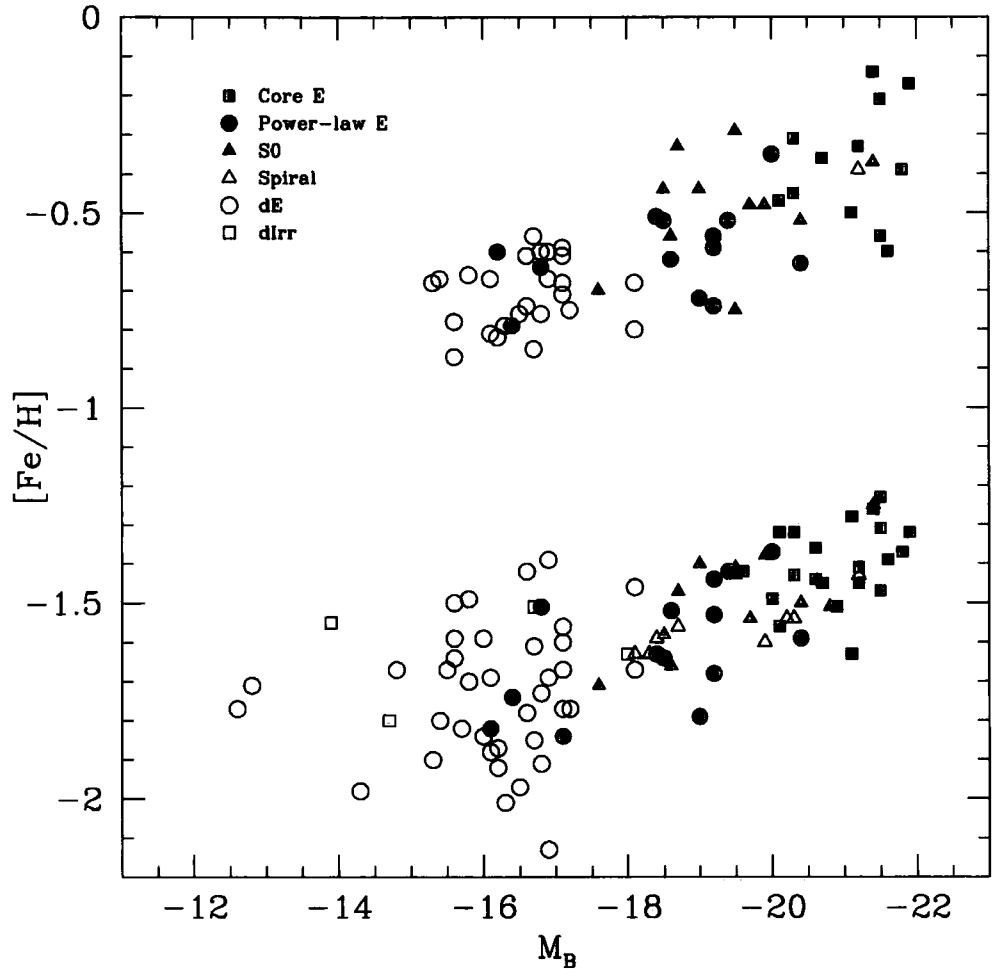

Figure 5.9: GC metallicity peak vs. galaxy luminosity for metal-poor and metal-rich GC subpopulations (Brodie & Strader 2006). The data come from Strader et al. (2004) and Strader et al. (2006). This compiled data show a correlation between metallcity peaks and host galaxy luminosity in both metal-poor and metal-rich GCs.

low density environments, similar to those used by Lotz et al. (2004) to strengthen the correlation between GC blue peak and galaxy luminosity in the higher density Virgo and Fornax clusters. It is therefore still not clear whether the slope of the blue(metal-poor) GC peak in field environments is different from that in clusters. In fact, Strader et al. (2004) predict that the slope of the metal-poor GC metallicity against galaxy luminosity in dense environment should be steeper than that in low density environments if cosmic reionization caused the quenching of the blue GC formation.

5.5 Conclusions

- From the pairs and triplets of our Galactic globular cluster sample that have an identical metallicity, but a different horizontal branch morphology, we have confirmed that the horizontal branch morphology can have a significant effect on the Balmer absorption lines in the integrated light of a globular cluster. In particular, an excess of blue horizontal branch stars makes a globular cluster look younger by boosting the Balmer absorption lines, even when independent age estimates indicate an older age.

- We have investigated possible origins of the unexpected excess of globular clusters in NGC3377 near g ~25.5 and in NGC474 near V~25.5, which deviate from a normal Gaussian luminosity function. The origin of the entire population in NGC3377 is still not understood, but some of them are confirmed to be background galaxies by visual inspection and some are possibly diffuse star clusters. For NGC474 most of them are genuine GCs, but some possible background galaxies are expected.

- The mean colours of our GCSs in low density environments are slightly bluer ($\Delta(g - z)_0 \sim 0.05$) than their counterparts in high density environment at a given luminosity. By assuming a few combinations of ages and employing a simple stellar population

model, this colour offset corresponds to a metallicity difference of $\Delta[Fe/H] \sim 0.15 - 0.20$ or an age difference of $\Delta age \sim 2Gyr$ on average. Therefore, GCs in field galaxies appear to be either less metal-rich or younger than those in cluster galaxies.

- A correlation between blue peak colour of GCs and host galaxy luminosity was not detected in our low-density galaxy sample, whereas this correlation has been found in the Virgo cluster (ACSVCS). It is not clear whether the absence of such a trend is because simply our galaxy luminosity range is too narrow or because intrinsically the slope of the relation depends on environment. To distinguish these two, observation of GCs in dwarf ellipticals in low density environments is needed.

- The more varied shapes of the colour distributions for GCSs in the Virgo cluster sample could imply that more complex galaxy formation processes are taking place in galaxy clusters, for example by interactions/harassment with adjacent galaxies. The higher fraction of red GCs in cluster galaxies also supports this possibility.

- Although we have found that galaxy environment has a subtle effect on the formation and metal enrichment of GC systems, host galaxy mass is the primary factor that determines the stellar populations of GCs and the galaxy itself.

5.6 Future perspectives

Large surveys of Galactic globular clusters and extragalactic globular cluster systems continue to be undertaken with both ground and space-based instruments. Following the ACS Virgo Cluster Survey, the ACS Fornax Cluster Survey (Jordán et al. 2007b) has observed 43 early-type galaxies in the Fornax cluster and is investigating properties of globular cluster systems in that environment which is somewhat looser and less dense than Virgo. More recently, the HST/ACS Coma Cluster Survey (Carter et al. 2008) planned to cover an area

of 740 arcmin^2 including GCs around the brightest cluster galaxies as well as searching for intergalactic GCs. Unfortunately the failure of the ACS in January, 2007 resulted in only 28% of the survey being completed, but the data will be still invaluable for studying globular cluster systems in an extremely rich cluster environment.

In the near future, the new instrument for HST succeeding ACS, WFC3, has been built and is scheduled to be installed during the Servicing Mission 4 in 2009. WFC3/UVIS has increased sensitivity at extended UV wavelengths compared to ACS/WFC and WFC3/IR will have improved in sensitivity by a factor of 2 compared to NICMOS. All these instruments show much better performance in terms of read-out noise and dark current than ACS. These high performances will allow us to break the metallicity-age degeneracy using two colours of globular clusters more effectively. Finally, the James Webb Space Telescope (JWST) in the future is expected to make huge leap in studying extragalactic globular clusters by allowing us to see the faint end of globular cluster luminosity functions, globular cluster systems in more distant galaxies, and more globular clusters in dwarf galaxies.

Bibliography

Ajhar, E. A., Blakeslee, J. P., & Tonry, J. L. 1994, AJ, 108, 2087

Ashman, K. M., & Zepf, S. E. 1992, ApJ, 384, 50

Ashman, K. M., Bird, C. M., & Zepf, S. E. 1994, AJ, 108, 2348

Balogh, M. L., Schade, D., Morris, S. L., Yee, H. K. C., Carlberg, R. G., & Ellingson, E. 1998, ApJ Lett., 504, L75

Balcells, M., & Carter, D. 1993, AAP, 279, 376

Barmby, P., Huchra, J. P., Brodie, J. P., Forbes, D. A., Schroder, L. L., & Grillmair, C. J. 2000, AJ, 119, 727

Baugh, C. M., Cole, S., & Frenk, C. S. 1996, MNRAS, 283, 1361

Baugh, C. M., Cole, S., Frenk, C. S., & Lacey, C. G. 1998, ApJ, 498, 504

Baumgardt, H., & Makino, J. 2003, MNRAS, 340, 227

Beasley, M. A., Brodie, J. P., Strader, J., Forbes, D. A., Proctor, R. N., Barmby, P., & Huchra, J. P. 2004, AJ, 128, 1623

Beasley, M. A., Brodie, J. P., Strader, J., Forbes, D. A., Proctor, R. N., Barmby, P., & Huchra, J. P. 2005, AJ, 129, 1412

Beasley, M. A., Bridges, T., Peng, E., Harris, W. E., Harris, G. L. H., Forbes, D. A., & Mackie, G. 2008, MNRAS, 386, 1443

Beers, T. C., Flynn, K., & Gebhardt, K. 1990, AJ, 100, 32

Bellazzini, M., Ferraro, F. R., & Ibata, R. 2003, AJ, 125, 188

Benjamin, R. A., et al. 2003, P.A.S.P., 115, 953

Bertin,E., & Arnouts,S., 1996, A&AS, 117, 393

Bica, E., Dutra, C. M., Soares, J., & Barbuy, B. 2003, AAP, 404, 223

Bird, C. M., & Beers, T. C. 1993, AJ, 105, 1596

Borissova, J., Pessev, P., Ivanov, V. D., Saviane, I., Kurtev, R., & Ivanov, G. R. 2003, AAP, 411, 83

Brodie, J. P., & Huchra, J. P. 1991, ApJ, 379, 157

Brodie, J. P., Strader, J., Denicoló, G., Beasley, M. A., Cenarro, A. J., Larsen, S. S., Kuntschner, H., & Forbes, D. A. 2005, AJ, 129, 2643

Brodie, J. P., & Strader, J. 2006, ARA&A, 44, 193

Bruzual, G., & Charlot, S. 2003, MNRAS, 344, 1000

Burgarella, D., Kissler-Patig, M., & Buat, V. 2001, AJ, 121, 2647

Burstein, D., Faber, S. M., Gaskell, C. M., & Krumm, N. 1984, ApJ, 287, 586

Burstein, D., et al. 2004, ApJ, 614, 158

Cantiello, M., & Blakeslee, J. P. 2007, ApJ, 669, 982

Carney, B. W. 2001, in Star Clusters, Saas-Fee Advanced Course 28, ed. L. Labbardt, & B. Binggeli (Berlin: Springer), 1

Carter, D., et al. 2008, ApJS, 176, 424

Cassisi, S., Salaris, M., Castelli, F., & Pietrinferni, A. 2004, ApJ, 616, 498

Cederbloom, S. E., Moss, M. J., Cohn, H. N., Lugger, P. M., Bailyn, C. D., Grindlay, J. E., & McClure, R. D. 1992, AJ, 103, 480

Chaboyer, B. 1995, ApJ Lett., 444, L9

Clemens, M. S., Bressan, A., Nikolic, B., Alexander, P., Annibali, F., & Rampazzo, R. 2006, MNRAS, 370, 702

Cohen, J. G., Matthews, K., & Cameron, P. B. 2005, ApJ Lett., 634, L45

Cole, S., Lacey, C. G., Baugh, C. M., & Frenk, C. S. 2000, MNRAS, 319, 168

Côté, P., Marzke, R. O., & West, M. J. 1998, ApJ, 501, 554

Côté, P., McLaughlin, D. E., Cohen, J. G., & Blakeslee, J. P. 2003, ApJ, 591, 850

Côté, P., et al. 2004, ApJS, 153, 223

Covino, S., Galletti, S., & Pasinetti, L. E. 1995, AAP, 303, 79

Da Costa, G. S., & Armandroff, T. E. 1995, AJ, 109, 2533

De Angeli, F., Piotto, G., Cassisi, S., Busso, G., Recio-Blanco, A., Salaris, M., Aparicio, A., & Rosenberg, A. 2005, AJ, 130, 116

Djorgovski, S., Piotto, G., & Mallen-Ornelas, G. 1991, The Formation and Evolution of Star Clusters, 13, 262

Djorgovski, S., Piotto, G., Phinney, E. S., & Chernoff, D. F. 1991, ApJ Lett., 372, L41

Djorgovski, S., & Piotto, G. 1992, AJ, 104, 2112

Dotter, A., Chaboyer, B., Jevremović, D., Baron, E., Ferguson, J. W., Sarajedini, A., & Anderson, J. 2007, AJ, 134, 376

Dressler, A. 1980, ApJ, 236, 351

Dubath, P., Meylan, G., & Mayor, M. 1997, AAP, 324, 505

Dupraz, C., & Combes, F. 1986, AAP, 166, 53

Durrell, P. R., & Harris, W. E. 1993, AJ, 105, 1420

Dutra, C. M., Bica, E., Soares, J., & Barbuy, B. 2003, AAP, 400, 533

Eggen, O. J., Lynden-Bell, D., & Sandage, A. R. 1962, ApJ, 136, 748

Fall, S. M., & Zhang, Q. 2001, ApJ, 561, 751

Peebles, P. J. E. 1984, ApJ, 277, 470

Ferguson, A. M. N., Irwin, M. J., Ibata, R. A., Lewis, G. F., & Tanvir, N. R. 2002, AJ, 124, 1452

Ferrarese, L., et al. 2006, ApJS, 164, 334

Ferraro, F. R., Paltrinieri, B., Rood, R. T., & Dorman, B. 1999, ApJ, 522, 983

Forbes, D. A., & Thomson, R. C. 1992, MNRAS, 254, 723

Forbes, D. A., Franx, M., Illingworth, G. D., & Carollo, C. M. 1996, ApJ, 467, 126

Forbes, D. A., Brodie, J. P., & Grillmair, C. J. 1997, AJ, 113, 1652

Forbes, D. A., & Forte, J. C. 2001, MNRAS, 322, 257

Galleti, S., Federici, L., Bellazzini, M., Fusi Pecci, F., & Macrina, S. 2004, AAP, 416, 917

Gebhardt, K., & Kissler-Patig, M. 1999, AJ, 118, 1526

Geisler, D., Lee, M. G., & Kim, E. 1996, AJ, 111, 1529

Giavalisco, M., et al. 2004, ApJ Lett., 600, L93

Giraradi, L. 2006, http://pleiadi.pd.astro.it/isoc_photsys.02/isoc_acs_wfc/index.html

Gómez, P. L., et al. 2003, ApJ, 584, 210

Goudfrooij, P., Gilmore, D., Whitmore, B. C., & Schweizer, F. 2004, ApJ Lett., 613, L121

Guhathakurta, P., Webster, Z. T., Yanny, B., Schneider, D. P., & Bahcall, J. N. 1998, AJ, 116, 1757

Harris, W. E., & van den Bergh, S. 1981, AJ, 86, 1627

Harris, W. E. 1991, ARA&A, 29, 543

Harris, W.E. 1996, AJ, 112, 1487

Harris, W. E. 2001, in Star Clusters, Saas-Fee Advanced Course 28, ed. L. Labbardt, & B. Binggeli (Berlin: Springer), 223

Harris, W. E., & Harris, G. L. H. 2002, AJ, 123, 3108

Harris, W. E., Harris, G. L. H., Layden, A. C., & Stetson, P. B. 2007, AJ, 134, 43

Hernquist, L., & Quinn, P. J. 1988, ApJ, 331, 682

Hernquist, L., & Quinn, P. J. 1989, ApJ, 342, 1

Herschel, W. 1789, Philosophical Transactions Series I, 79, 212

Hesser, J. E., & Shawl, S. J. 1985, P.A.S.P., 97, 465

Howell, J. H., Guhathakurta, P., & Tan, A. 2000, AJ, 119, 1259

Hurt, R. L., Jarrett, T. H., Kirkpatrick, J. D., Cutri, R. M., Schneider, S. E., Skrutskie, M., & van Driel, W. 2000, AJ, 120, 1876

Ibata, R., Irwin, M., Lewis, G., Ferguson, A. M. N., & Tanvir, N. 2001, Nature, 412, 49

Iben, I. J., & Faulkner, J. 1968, ApJ, 153, 101

Jordán, A., West, M. J., Côté, P., & Marzke, R. O. 2003, AJ, 125, 1642

Jordán, A., et al. 2004, ApJS, 154, 509

Jordán, A., et al. 2005, ApJ, 634, 1002

Jordán, A., et al. 2006, ApJ Lett., 651, L25

Jordán, A., et al. 2007, ApJS, 169, 213

Jordán, A., et al. 2007, ApJS, 171, 101

Kim, Y.-C., Demarque, P., Yi, S. K., & Alexander, D. R. 2002, ApJS, 143, 499

King, I. 1962, AJ, 67, 471

Kobulnicky, H. A., et al. 2005, AJ, 129, 239

Krist, J., & Hook, R. 2004, http://www.stsci.edu/software/tinytim

Kroupa, P. 2001, MNRAS, 322, 231

Kundu, A., & Whitmore, B. C. 2001, AJ, 121, 2950

Kundu, A., & Whitmore, B. C. 2001, AJ, 122, 1251

Kundu, A., & Zepf, S. E. 2007, ApJ Lett., 660, L109

Kuntschner, H., Smith, R. J., Colless, M., Davies, R. L., Kaldare, R., & Vazdekis, A. 2002, MNRAS, 337, 172

Larsen, S. S. 1999, AAPS, 139, 393

Larsen, S. S., Brodie, J. P., Huchra, J. P., Forbes, D. A., & Grillmair, C. J. 2001, AJ, 121, 2974

Larsen, S. S., Brodie, J. P., Beasley, M. A., Forbes, D. A., Kissler-Patig, M., Kuntschner, H., & Puzia, T. H. 2003, ApJ, 585, 767

Layden, A. C., & Sarajedini, A. 2000, AJ, 119, 1760

Lee, Y.-W., Demarque, P., & Zinn, R. 1994, ApJ, 423, 248

Lee, Y.-W., Joo, J.-M., Sohn, Y.-J., Rey, S.-C., Lee, H.-C., & Walker, A. R. 1999, Nature, 402, 55

Lee, H.-c., Yoon, S.-J., & Lee, Y.-W. 2000, AJ, 120, 998

Lee, H.-c., Lee, Y.-W., & Gibson, B. K. 2002, AJ, 124, 2664

Lee, H.-c., & Worthey, G. 2005, ApJS, 160, 176

Lewis, I., et al. 2002, MNRAS, 334, 673

Li, Y., & Burstein, D. 2003, ApJ Lett., 598, L103

Lotz, J. M., Miller, B. W., & Ferguson, H. C. 2004, ApJ, 613, 262

Lutz, D. 1991, AAP, 245, 31

Mackey, A. D., & Gilmore, G. F. 2004, MNRAS, 355, 504

Malin, D. F., & Carter, D. 1980, Nature, 285, 643

Malin, D. F., & Carter, D. 1983, ApJ, 274, 534

Maraston, C. 1998, MNRAS, 300, 872

Maraston, C., & Thomas, D. 2000, ApJ, 541, 126

Maraston, C., Greggio, L., Renzini, A., Ortolani, S., Saglia, R. P., Puzia, T. H., & Kissler-Patig, M. 2003, AAP, 400, 823

Massey, P., Strobel, K., Barnes, J. V., & Anderson, E. 1988, ApJ, 328, 315

Massey, P., Valdes, F., & Barnes, J. 1977, A User's Guide to CCD Reductions with IRAF

Massey, P. 1977, A User's Guide to CCD Reductions with IRAF

Messier, C., 1781. Catalogue des Nébuleuses & des amas d'Étoiles. Connoissance des Temps for 1784 (published 1781), pp. 227-267

Michard, R., & Prugniel, P. 2004, AAP, 423, 833

Mei, S., et al. 2007, ApJ, 655, 144

Mendel, J. T., Proctor, R. N., & Forbes, D. A. 2007, MNRAS, 379, 1618

Oke, J. B. 1990, AJ, 99, 1621

Olsen, K. A. G., Miller, B. W., Suntzeff, N. B., Schommer, R. A., & Bright, J. 2004, AJ, 127, 2674

Ortolani, S., Barbuy, B., & Bica, E. 1990, AAP, 236, 362

Parmentier, G., Jehin, E., Magain, P., Neuforge, C., Noels, A., & Thoul, A. A. 1999, AAP, 352, 138

Pavlovsky, C., et al. 2006, "Advanced Camera for Surveys Instrument Handbook for Cycle 16", Version 7.1, (Baltimore: STScI)

Peng, E. W., et al. 2006, ApJ, 639, 95

Peng, E. W., et al. 2006, ApJ, 639, 838

Peng, E. W., et al. 2008, ApJ, 681, 197

Perrett, K. M., Bridges, T. J., Hanes, D. A., Irwin, M. J., Brodie, J. P., Carter, D., Huchra, J. P., & Watson, F. G. 2002, AJ, 123, 2490

Ponder, J. M., et al. 1998, AJ, 116, 2297

Prugniel, P., & Simien, F. 1996, AAP, 309, 749

Puzia, T. H., Zepf, S. E., Kissler-Patig, M., Hilker, M., Minniti, D., & Goudfrooij, P. 2002, AAP, 391, 453

Puzia, T. H., Saglia, R. P., Kissler-Patig, M., Maraston, C., Greggio, L., Renzini, A., & Ortolani, S. 2002, AAP, 395, 45

Puzia, T. H., Perrett, K. M., & Bridges, T. J. 2005, AAP, 434, 909

Quinn, P. J. 1984, ApJ, 279, 596

Rey, S.-C., Yoon, S.-J., Lee, Y.-W., Chaboyer, B., & Sarajedini, A. 2001, AJ, 122, 3219

Richtler, T. 2003, Stellar Candles for the Extragalactic Distance Scale, 635, 281

Riess, A., & Mack, J., 2004, ISR ACS 2004-006

Roberts, M. S., Hogg, D. E., Bregman, J. N., Forman, W. R., & Jones, C. 1991, ApJS, 75, 751

Robin, A. C., Reylé, C., Derrière, S., & Picaud, S. 2003, AAP, 409, 523

Rose, J. A., Stetson, P. B., & Tripicco, M. J. 1987, AJ, 94, 1202

Rosenberg, A., Saviane, I., Piotto, G., & Aparicio, A. 1999, AJ, 118, 2306

Salaris, M., & Weiss, A. 2002, AAP, 388, 492

Sandage, A. 1982, ApJ, 252, 553

Sarajedini, A., et al. 2007, AJ, 133, 1658

Saviane, I., Rosenberg, A., Piotto, G., & Aparicio, A. 2000, AAP, 355, 966

Schiavon, R. P., Rose, J. A., Courteau, S., & MacArthur, L. A. 2004, ApJ Lett., 608, L33

Schiavon, R. P., Rose, J. A., Courteau, S., & MacArthur, L. A. 2005, ApJS, 160, 163

Schiminovich, D., van Gorkom, J. H., van der Hulst, J. M., & Malin, D. F. 1995, ApJ Lett., 444, L77

Schlegel, D.J.,Finkbeiner, D.P., & Davis, M. 1998, ApJ, 500, 525

Schweizer, F., Seitzer, P., Faber, S. M., Burstein, D., Dalle Ore, C. M., & Gonzalez, J. J. 1990, ApJ Lett., 364, L33

Schweizer, F., & Seitzer, P. 1992, AJ, 104, 1039

Schweizer, F., Seitzer, P., & Brodie, J. P. 2004, AJ, 128, 202

Secker, J., Geisler, D., McLaughlin, D. E., & Harris, W. E. 1995, AJ, 109, 1019

Searle, L., & Zinn, R. 1978, ApJ, 225, 357

Seitzer, P. & Schweizer, F. 1990, Dynamics and Interactions of Galaxies, p. 270, ed. Wielen, R., Springer-Verlag, Heidelberg

Shapley, H. 1918, P.A.S.P., 30, 253

Shapley, H. 1918, ApJ, 48, 89

Shapley, H. 1918, ApJ, 48, 279

Shapley, H., & Shapley, M. B. 1919, ApJ, 50, 42

Sikkema, G., Peletier, R. F., Carter, D., Valentijn, E. A., & Balcells, M. 2006, AAP, 458, 53

Sikkema, G., Carter, D., Peletier, R. F., Balcells, M., Del Burgo, C., & Valentijn, E. A. 2007, AAP, 467, 1011

Sirianni, M., et al. 2005, P.A.S.P., 117, 1049

Skrutskie, M. F., et al. 1997, The Impact of Large Scale Near-IR Sky Surveys, 210, 25

Sohn, Y.-J., Byun, Y.-I., & Chun, M.-S. 1996, Ap&SS, 243, 379

Springel, V., et al. 2005, Nature, 435, 629

Spitler, L. R., Forbes, D. A., & Beasley, M. A. 2008, MNRAS, 389, 1150

Strader, J., Brodie, J. P., & Forbes, D. A. 2004, AJ, 127, 3431

Strader, J., Brodie, J. P., Cenarro, A. J., Beasley, M. A., & Forbes, D. A. 2005, AJ, 130, 1315

Strader, J., Brodie, J. P., Spitler, L., & Beasley, M. A. 2006, AJ, 132, 2333

Strader, J., Beasley, M. A., & Brodie, J. P. 2007, AJ, 133, 2015

Thomson, R. C., & Wright, A. E. 1990, MNRAS, 247, 122

Thomson, R. C. 1991, MNRAS, 253, 256

Thomas, D., Maraston, C., & Bender, R. 2003, MNRAS, 339, 897

Thomas, D., Maraston, C., & Korn, A. 2004, MNRAS, 351, L19

Thomas, D., Maraston, C., Bender, R., & Mendes de Oliveira, C. 2005, ApJ, 621, 673

Tonry, J. L., Blakeslee, J. P., Ajhar, E. A., & Dressler, A. 1997, ApJ, 475, 399

Tonry, J. L., Dressler, A., Blakeslee, J. P., Ajhar, E. A., Fletcher, A. B., Luppino, G. A., Metzger, M. R., & Moore, C. B. 2001, ApJ, 546, 681

Trager, S. C., Worthey, G., Faber, S. M., Burstein, D., & Gonzalez, J. J. 1998, ApJS, 116, 1

Tripicco, M. J. 1989, AJ, 97, 735

Tully, B. 1988, Nearby Galaxy Catalogue, Cambridge University Press

van Dokkum, P. G. 2001, P.A.S.P., 113, 1420

Vandenberg, D. A., Bolte, M., & Stetson, P. B. 1990, AJ, 100, 445

Villanova, S., et al. 2007, ApJ, 663, 296

Whitmore, B. C., Schweizer, F., Leitherer, C., Borne, K., & Robert, C. 1993, AJ, 106, 1354

Whitmore, B. C., & Schweizer, F. 1995, AJ, 109, 960

Woodley, K. A., Harris, W. E., & Harris, G. L. H. 2005, AJ, 129, 2654

Worthey, G., Faber, S. M., Gonzalez, J. J., & Burstein, D. 1994, ApJS, 94, 687

Worthey, G., & Ottaviani, D. L. 1997, ApJS, 111, 377

Yi, S., Demarque, P., & Kim, Y.-C. 1997, ApJ, 482, 677

Yoon, S.-J., Yi, S. K., & Lee, Y.-W. 2006, Science, 311, 1129

Zehavi, I., et al. 2005, ApJ, 630, 1

Zepf, S. E., & Ashman, K. M. 1993, MNRAS, 264, 611

Zepf, S. E., Ashman, K. M., & Geisler, D. 1995, ApJ, 443, 570

Zinn, R., & West, M. J. 1984, ApJS, 55, 45

Zinn, R. 1993, The Globular Cluster-Galaxy Connection, 48, 38